UNIVERSIDADE FEDERAL DO CEARÁ

Centro de Ciências

Departamento de Física

UNIVERSITEIT ANTWERPEN

Faculteit Wetenschappen

Departement Fysica

Silvia Helena Roberto de Sena

Propriedades eletrônicas de tricamada de grafeno e nanofitas de carbono tensionadas

---

Electronic properties of trilayer graphene and strained carbon nanoribbons

Fortaleza

2012

Silvia Helena Roberto de Sena

Propriedades eletrônicas de tricamada de grafeno e nanofitas de carbono tensionadas / Electronic properties of trilayer graphene and strained carbon nanoribbons

Tese apresentada ao Curso de Pós-Graduação em Física da Universidade Federal do Ceará como parte dos requisitos para a obtenção do título de Doutor em Física

Orientador:
Prof. Dr. João Milton Pereira Júnior

Co-orientador:
Prof. Dr. François M. Peeters

Doutorado em Física
Departamento de Física
Centro de Ciências
Universidade Federal do Ceará.

Fortaleza – CE

19 de dezembro de 2012

Dados Internacionais de Catalogação na Publicação
Universidade Federal do Ceará
Biblioteca Universitária
Gerada automaticamente pelo módulo Catalog, mediante os dados fornecidos pelo(a) autor(a)

S477p Sena, Silvia Helena Roberto de.
Propriedades eletrônicas de tricamada de grafeno e nanofitas de carbono tensionadas / Silvia Helena Roberto de Sena. – 2012.
112 f. : il. color.

Tese (doutorado) – Universidade Federal do Ceará, Centro de Ciências, Programa de Pós-Graduação em Física , Fortaleza, 2012.
Orientação: Prof. Dr. João Milton Pereira Júnior.

1. Grafeno. 2. Nanofitas de carbono. 3. Tricamadas de grafeno. I. Título.

CDD 530

Tese de doutorado sob o título *Propriedades eletrônicas de tricamada de grafeno e nanofitas de carbono tensionadas / Electronic properties of trilayer graphene and strained carbon nanoribbons*, defendida por *Silvia Helena Roberto de Sena* e aprovada em 19 de Dezembro de 2012, em Fortaleza, Ceará, pela banca examinadora constituda pelos doutores:

Prof. Dr. João Milton Pereira Júnior
Departamento de Física - UFC
Orientador

Prof. Dr. François Maria Leopold Peeters
Departamento de Física - UFC
Department of Physics - University of Antwerp, Belgium
Co-orientador

Prof. Dr. Gil de Aquino Farias
Departamento de Física - UFC

Prof^{a}. Dr^{a}. Ana Luiza Cardoso Pereira
Faculdade de Ciências Aplicadas - UNICAMP

Prof. Dr. Eduardo Costa Girão
Departamento de Física - Universidade Federal do Piauí

To my parents,
Ernandes e Fátima,
and to my sister
Ana Cristina.

Acknowledgements

I would like to express my gratitude to my parents, Ernandes e Fátima, for all the support, for teaching me, in their own way, the difference between right and wrong, and for all the moral values that I will carry throughout my life.

I thank my sister Ana Cristina (Bebê) for being such a motherly sister, for always want to take care of me, and specially for being the friend I know I can always count on.

I thank Professor João Milton Pereira Júnior for the support and for all things he has patiently taught me along the past five years as my advisor.

I thank to Professor François Peeters for his guidance during my staying in Antwerp, and for patiently correcting the papers.

I thank Professor Raimundo Nogueira da Costa Filho for kindly helping me every time I had trouble solving the problem he suggested, and for positively encouraging me to keep going.

I thank to Professor Gil de Aquino Farias for being always so nice and willing to help.

I thank the other members of the jury, Professors Ana Luiza Cardoso Pereira and Eduardo Costa Girão, for the time spent reading the thesis, for their corrections and suggestions that made this a better work.

I thank my friends Philipe, Ítalo e Igor for their company since we started the college, and for the good time we spent together.

My thanks to Edith, William, Ricardo, Massoud and Victor who helped me to adapt and made my staying in Antwerp a lot easier.

I thank all the Professors of the Department of Physics who contributed to my academic development.

Finally, I would like to thank CAPES for the financial support, which made the development of this work possible.

Resumo

Grafeno é um cristal bidimensional cujo espectro eletrônico a baixas energias ($E < 1$ eV) apresenta dispersão linear e ausência de gap que, juntamente com a natureza quiral dos portadores de carga, são responsáveis por uma variedade de propriedades incomuns. Como resultado da sua natureza singular, um grande esforço tem sido feito para entender todas as suas propriedades fundamentais e tentar gerar uma nova tecnologia baseada nesse material.

Nesta tese, nós realizamos um estudo teórico de dois tipos de sistemas: nanofitas de grafeno e tricamadas grafeno (TCG). No que diz respeito ao primeiro sistema, um modelo de ligação forte (tight-binding) é utilizado para estudar as bandas de energia de grafeno e fitas de grafeno sujeitas a uma tensão de cisalhamento. A fita é constituída por linhas de átomos de carbono cujas bordas estão orientadas nas direções conhecidas como "armchair" ou "zigzag". Uma tensão de cisalhamento simples é aplicada na direção x de forma que as distâncias interatômicas na direção y são mantidas inalteradas. Esta modificação na rede cristalina origina bandas de energia que diferem em vários aspectos do sistema original sem qualquer deformação. As mudanças no espectro dependem do deslocamento entre linhas adjacentes da fita, bem como do parâmetro de "hopping" modificado. Mostra-se também que este cisalhamento simples modifica as propriedades eletrônicas de ambos os sistemas, fitas de grafeno e grafeno, abrindo e fechando gaps de energia para diferentes deslocamentos do sistema. A densidade de estados modificada também é mostrada. Por fim, o modelo contínuo é utilizado a fim de investigar o espectro electrônico de três camadas de grafeno acopladas (tricamada de grafeno), na presença de um campo magnético externo. Nesse contexto, obtemos expressões analíticas para os níveis de Landau para ambos os tipos de empilhamento: Bernal (ABA) e romboédrico (ABC), verificando-se uma forte dependência dos níveis de energia com o tipo de empilhamento. Embora o espectro de Landau para tricamadas ABA seja uma sobreposição dos espectros de uma monocamada e de uma bicamada, tricamadas com empilhamento ABC apresentam uma dispersão do tipo $B^{3/2}$ com o campo magnético. Foi mostrado que uma assimetria entre as camadas, que pode ser introduzida por um potencial externo, pode influenciar fortemente as propriedades do sistema. Além disso, as energias de ressonância cíclotron, assim como forças de oscilador correspondentes, e o espectro de absorção para tricamadas de grafeno so calculadas para ambos os tipos de empilhamento. Verificou-se que um potencial de porta aplicado através das camadas leva a (1) uma redução das energias de transição, (2) um levantamento da degenerescência do nível de Landau $n = 0$, e (3) a quebra de simetria entre elétrons e buracos.

Abstract

Graphene is a truly two-dimensional crystal with a gapless linear electronic spectrum at low energies ($E < 1$ eV) which, along with the chiral nature of its charge carriers, is responsible for a variety of unusual properties. As a result of its uniqueness, a great effort has been made in order to understand all its fundamental properties and try to generate a new technology of them.

In this thesis we theoretically study two types of graphene-related systems: graphene nanoribbons and trilayer graphene (TLG). Concerning the former, a tight-binding model is used to study the energy band of graphene and graphene ribbon under simple shear strain. The ribbon consists of lines of carbon atoms in an armchair or zigzag orientation where a simple shear strain is applied in the x-direction keeping the atomic distances in the y-direction unchanged. Such modification in the lattice gives an energy band that differs in several aspects from the one without any shear and with pure shear. The changes in the spectrum depend on the line displacement of the ribbon, and also on the modified hopping parameter. It is also shown that this simple shear strain tunes the electronic properties of both graphene and graphene ribbon, opening and closing energy gaps for different displacements of the system. The modified density of states is also shown. On the latter subject, the continuum model is used in order to investigate the electronic spectrum of three coupled graphene layers (graphene trilayers) in the presence of an external magnetic field. We obtain analytical expressions for the Landau level (LL) spectrum for both the ABA and ABC types of stacking, which exhibit very different dependence on the magnetic field. While the LL spectrum of ABA TLG is found to be a superposition of a monolayer-like and bilayer-like spectra, the ABC TLG present a nearly $B^{3/2}$ field dependence. We show that layer asymmetry and an external gate voltage can strongly influence the properties of the system. In addition, the cyclotron resonance energies, the corresponding oscillator strengths, and the cyclotron absorption spectrum for trilayer graphene are calculated for both ABA and ABC stacking. A gate potential across the stacked layers leads to (1) a reduction of the transition energies, (2) a lifting of the degeneracy of the zero Landau level, and (3) the removal of the electron-hole symmetry.

Abstract

Grafeen is een twee dimensionaal kristal met een lineair spectrum zonder bandkloof. Dit spectrum zorgt samen met de chirale eigenschappen van de ladingsdragers voor zeer merkwaardige elektronische fenomenen. Hierdoor wordt dit unieke materiaal zeer intensief onderzocht om alle fundamentele eigenschappen ervan te doorgronden en om te proberen nieuwe technologien erop te baseren.

In deze thesis werd er theoretisch onderzoek gedaan naar twee type van grafeen gerelateerde systemen: grafeen nanoribbons en trilaag grafeen (TLG). Gebruikmakend van het "tight-binding" formalisme wordt de energie banden structuur onderzocht van grafeen en een grafeen nanoribbon onder uitrekking. ('shear strain'). De nanoribbon bestaat uit rijen van koolstofatomen met een "armchair" of "zigzag" orintatie die uitgerekt worden in de x-richting zodat in de y-richting de interatomaire afstand bewaard blijft. Zulke aanpassing zorgt voor een energie band die op vele vlakken verschillend is van deze zonder uitrekking of met isotrope uitrekking. De veranderingen in het spectrum hangen af van de verplaatsing van de rijen in de nanostrook, maar ook van de veranderende "hopping parameter". We tonen ook aan dat deze eenvoudige uitrekking de elektronische eigenschappen van zowel de nanostrook als het grafeen aanpast om een bandkloof te openen of te sluiten als gevolg van verschillende uitrekkingen in het systeem. Hiernaast wordt ook de toestandsdichtheid van deze systemen berekend. Bij trilaag grafeen wordt het continum model gebruikt om het elektronisch spectrum te onderzoeken van drie gekoppelde lagen grafeen in een magnetisch veld. We verkrijgen analytische uitdrukkingen voor het spectrum van de Landau niveaus (LL) voor zowel de ABA als ABC types van stapeling. Deze niveaus hangen op een zeer verschillende manier af van het magnetisch veld. Terwijl het LL spectrum van ABA TLG een superpositie blijkt te zijn van dat van een monolaagachtig en een bilaagachtig system, vertoont ABC TLG een bijna B3/2 afhankelijkheid. We tonen aan dat de asymmetrie in de lagen en een externe potentiaal de eigenschappen van deze systemen sterk benvloedt. Daarenboven worden ook de cyclotron resonantie energien de bijbehorende oscillator sterktes en het cyclotron absorptie spectrum voor beide stapelwijzen van trilaag grafeen berekend. Een potentiaal over de opeen gestapelde lagen zorgt voor: (1) een verlaging van de transitietemperatuur, (2) dat de ontaarding van het nulde Landau niveau wordt opgeheven en (3) dan de elektron-holte symmetrie wordt doorbroken.

Contents

List of Figures

List of Tables

1 Introduction

Whenever scientists come across a new material a whole range of possibilities opens up. First, they want to find out all its fundamental properties in order to, finally, answer the questions: what is this material good for? Is it capable of generating a new technology or improve a current one? In this context, carbon materials have been the big stars in the scientific scenario for the last few decades.

Carbon is a chemical element responsible for the existence of a great variety of materials. Among those we can mention all organic compounds, which form the basis of life, and also many crystalline solids. But how is carbon able to form such different materials, with so many structural forms and different properties? The usual answer is that carbon's orbitals allow for many types of hybridization or, more simply, the carbon atom is able to bond with other atoms in many different ways. Roughly speaking, hybridization is a superposition of atomic orbitals, or a linear combination of atomic wave functions having the same principal quantum number.

1.1 Hybridization of Carbon Atoms

In the carbon atom ($C : 1s^2 2s^2 2p^2$) [1] two out of its six electrons occupy the $1s$ orbital, forming the inner or core shell. These electrons are strongly bound to the atom and do not take part in the chemical bonds. The four remaining electrons, called valence electrons, are set in $2s$ and $2p$ states. Then in its ground state the carbon atom has only two half-filled orbitals, what make us think that it will be able to form at most two bonds. Recalling that energy is released when bonds are formed, it becomes energetically favorable to maximize the number of bonds carbon can form. Since $2p$ orbitals are just

[1] This way of representing the orbitals or atomic states is known as spectroscopic notation. The first number is the principal quantum number n, the letter that follows it indicates the azimuthal quantum number l, with s, p, d, f, g, h corresponding to $l = 0, 1, 2, 3, 4, 5$. This notation arose from observations of spectra of atoms prior to the advent of quantum mechanics; the letters s, p, d and f are the first letters of the adjectives *sharp*, *principal*, *diffuse*, and *fundamental*, respectively; letters corresponding to higher values of l follow in alphabetical order [1].

≈ 4.18 eV higher in energy and this amount of energy is small compared with the binding energy of the chemical bonds [2], it turns out that, in the presence of other atoms, is energetically favorable to form an excited state by promoting one of its $2s$ electron to the empty $2p$ state, resulting in four half-filled orbitals $2s$ $2p_x$ $2p_y$ $2p_z$ that can participate in covalent bonds.

In order to have some qualitative idea of how these states look like, let us recall that, within central potential approximation, the wave function of a many electrons atom can be still written as $\psi_{nlm}(\mathbf{r}) = R_{nl}(r)Y_l^m(\theta,\varphi)$, where $R_{nl}(r)$ is the radial part that depends on the exact form of the central potential $V_c(r)$, and $Y_l^m(\theta,\varphi)$ stands for the spherical harmonics. In carbon atoms we just have to deal with s and p orbitals, which correspond to $l = 0, 1$. When $l = 0$ the only possible value of the magnetic quantum number is $m = 0$, consequently, for a fixed r, we have a real and constant wave function that will be represented by $|ns\rangle = R_{n0}(r)Y_0^0 = \frac{1}{\sqrt{4\pi}}R_{n0}(r)$. The case with $l = 1$ allows $m = -1, 0, 1$, producing the following states [3]:

$$|np_z\rangle = R_{n0}(r)Y_1^0(\theta,\varphi) = \sqrt{\frac{3}{4\pi}}R_{n1}(r)\cos\theta, \tag{1.1}$$

$$|np_{\pm1}\rangle = R_{n1}(r)Y_1^{\pm1}(\theta,\varphi) = \mp\sqrt{\frac{3}{8\pi}}R_{n1}(r)\sin\theta e^{\pm i\varphi}. \tag{1.2}$$

In order to have the real $p_{x(y)}$ orbitals we make a linear combinations of the states with $m = \pm1$ such as

$$|np_x\rangle = \frac{-1}{\sqrt{2}}\left(|np_1\rangle - |np_{-1}\rangle\right) = \sqrt{\frac{3}{4\pi}}R_{n1}(r)\sin\theta\cos\varphi, \tag{1.3}$$

$$|np_y\rangle = \frac{i}{\sqrt{2}}\left(|np_1\rangle + |np_{-1}\rangle\right) = \sqrt{\frac{3}{4\pi}}R_{n1}(r)\sin\theta\sin\varphi. \tag{1.4}$$

The angular dependence of the s, p_x orbitals are displayed in Fig. 1, where, for a fixed r, we plotted the absolute value of the wave functions along each direction of θ and φ. The blue spheres on the left correspond to the s orbital, while p_x consists of two spheres tangential at the origin to yz plane. The colors represent the sign of the wave function, blue (red) stands for positive (negative) values. The p_y and p_z orbitals have the same shape as p_x, but are rotated in such way to be along the y and z directions, respectively.

Besides the promotion of one $2s$ electron into the $2p_z$ state, when surrounded by other atoms, the $2s$ and $2p$ states mix in order to increase the overlap with the surrounding atoms orbitals, making the bonds stronger. This mixing is called hybridization, and the mix of the $2s$ state with $n = 1, 2, 3$ $2p$ states is called sp^n hybridization[1, 4, 5]. We are

now going to discuss briefly about the three types of hybridization of the carbon atom: sp, sp^2, sp^3. [2]

1.1.1 *sp* Hybridization

In sp hybridization, one of the three $|2p_j\rangle$ orbitals and the $|2s\rangle$ orbital are combined to form two hybrids $|sp_r\rangle$ and $|sp_l\rangle$ states, such as

$$|sp_r\rangle = c_1|2s\rangle + c_2|2p_x\rangle, \tag{1.5}$$

$$|sp_l\rangle = c_3|2s\rangle + c_4|2p_x\rangle. \tag{1.6}$$

The orthonormality condition states that $\langle sp_r|sp_l\rangle = 0$ and $\langle sp_r|sp_r\rangle = \langle sp_l|sp_l\rangle = 1$. In addition, it is required the two hybrid orbitals to have the same geometric form, meaning that apart from their spacial orientation, they should be the same. Since the form depends only on the relative amount of $|2s\rangle$ and $|2p_x\rangle$ orbitals in the linear superposition, and s states are spherical symmetric, it is necessary that $c_1 = c_3$. These conditions lead to the following pair of hybrid states:

$$|sp_r\rangle = \frac{1}{\sqrt{2}}\left(|2s\rangle + |2p_x\rangle\right), \tag{1.7}$$

$$|sp_l\rangle = \frac{1}{\sqrt{2}}\left(|2s\rangle - |2p_x\rangle\right). \tag{1.8}$$

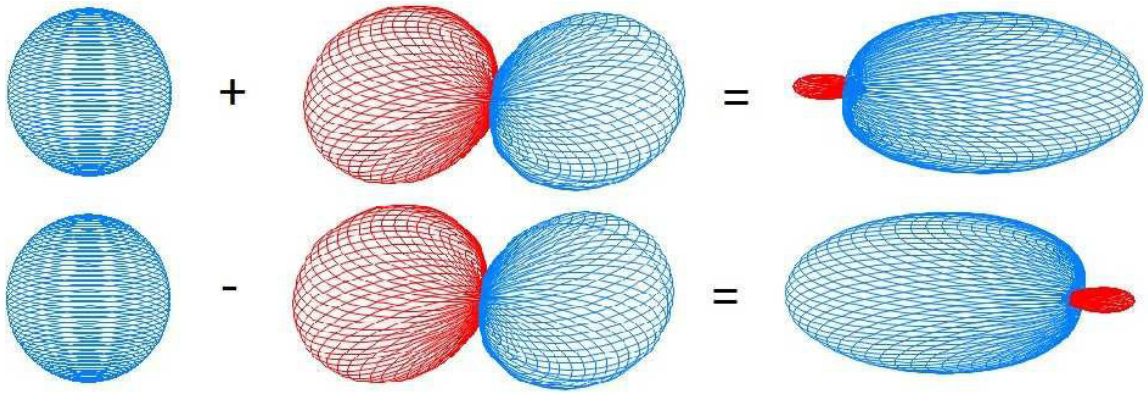

Figure 1: Schematic view of how the orbital s and p_x combine in order to form the hybrid states sp_r and sp_l.

A schematic view of these orbitals are shown in Fig. 1. The $|sp_r\rangle$ is extended in the positive x-direction, while $|sp_l\rangle$ is elongated in the negative direction. Thus, when the

[2] In materials such as bulckyballs and carbon nanotubes, carbon atoms assume a sp^δ hybridization, with $2 < \delta < 3$. This happens due the curved geometry of these materials' surface. A detailed discussion of this type of hybridization can be found in [6].

neighbor atoms are along the x-direction their wave function have a larger overlap with the hybrid orbitals than it would have with the pure $|2p_x\rangle$ orbital.

An example of material where the carbon atom has sp hybridization is the acetylene molecule C_2H_2. In this molecule all atoms are aligned, the hybrid orbitals of each carbon participate of σ bonds with one hydrogen and the other carbon atom. The pure orbitals p_y and p_z form the called π bonds that are weak compared to σ bonds.

1.1.2 sp^2 Hybridization

In sp^2 hybridization, two $2p$ orbitals and the $2s$ orbital are superposed to originate three sp^2 hybrid states.

$$|sp_a^2\rangle = c_1|2s\rangle + c_2|2p_x\rangle + c_3|2p_y\rangle, \tag{1.9}$$

$$|sp_b^2\rangle = c_4|2s\rangle + c_5|2p_x\rangle + c_6|2p_y\rangle, \tag{1.10}$$

$$|sp_c^2\rangle = c_7|2s\rangle + c_8|2p_x\rangle + c_9|2p_x\rangle. \tag{1.11}$$

Again we require the wave functions to be equivalent, what means that they can transform into each other under rotations about the z axis. Then, we have $c_1 = c_4 = c_7$. Besides, we can choose the axes in order to $|sp_a^2\rangle$ be symmetric about the xz plane. Consequently, we choose $c_3 = 0$. Finally, we impose the orthonormality condition that, together with the previous requirements, leads to the following hybrid orbitals:

$$|sp_a^2\rangle = \frac{1}{\sqrt{3}}|2s\rangle + \sqrt{\frac{2}{3}}|2p_x\rangle, \tag{1.12}$$

$$|sp_b^2\rangle = \frac{1}{\sqrt{3}}|2s\rangle - \frac{1}{\sqrt{6}}|2p_x\rangle + \frac{1}{\sqrt{2}}|2p_y\rangle, \tag{1.13}$$

$$|sp_c^2\rangle = \frac{1}{\sqrt{3}}|2s\rangle - \frac{1}{\sqrt{6}}|2p_x\rangle - \frac{1}{\sqrt{2}}|2p_y\rangle. \tag{1.14}$$

In order to check an important property of these orbitals let us recall that the operator $\mathbf{R_z}(\alpha) = e^{-i\alpha\mathbf{L_z}/\hbar 3}$ performs a rotation through an angle α about the z-axis, and that $\mathbf{L_z} = \frac{\hbar}{i}\frac{\partial}{\partial\varphi}$. Then, it can be easily shown that:

$$e^{-i\alpha\mathbf{L_z}/\hbar}|2s\rangle = |2s\rangle, \tag{1.15}$$

$$e^{-i\alpha\mathbf{L_z}/\hbar}|2p_x\rangle = \cos\alpha|2p_x\rangle + \sin\alpha|2p_y\rangle, \tag{1.16}$$

$$e^{-i\alpha\mathbf{L_z}/\hbar}|2p_y\rangle = -\sin\alpha|2p_x\rangle + \cos\alpha|2p_y\rangle. \tag{1.17}$$

[3]The function $\mathbf{R_z}(\alpha)$ is defined by $e^{-i\alpha\mathbf{L_z}/\hbar} = \sum_n \frac{1}{n!}(-i\alpha\mathbf{L_z}/\hbar)^n$ [3].

The expressions for the hybrid orbitals together with the rotation operator effect on the pure s and p states lead to:

$$e^{-i(2\pi/3)\mathbf{L_z}/\hbar}|sp_a^2\rangle = |sp_b^2\rangle, \tag{1.18}$$

$$e^{-i(2\pi/3)\mathbf{L_z}/\hbar}|sp_b^2\rangle = |sp_c^2\rangle. \tag{1.19}$$

The above expressions reveal a well-known property of the sp^2 hybridization: the hybrid orbitals are rotated by 120° in relation to each other which makes the chemical bonds formed by them to acquire a trigonal symmetry in the xy-plane (See Fig. 2). As examples of materials where the carbon atom has this kind of hybridization we can mention the ethylene molecule C_2H_4 and graphite.

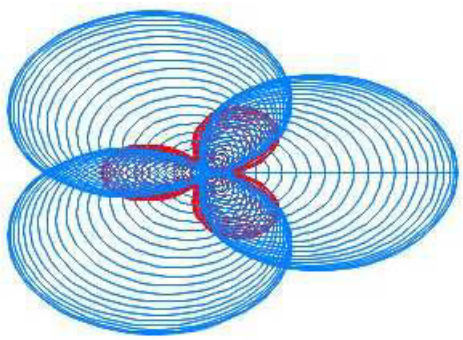

Figure 2: A top view of the hybrid sp^2 orbitals in $xy-$plane. The lines along which the orbitals are pointing make angles of 120° with each other.

1.1.3 sp^3 Hybridization

The sp^3 happens when all three $2p$ and the s orbitals are superposed to form four hybrid orbitals:

$$|sp_a^3\rangle = c_1|2s\rangle + c_2|2p_x\rangle + c_3|2p_y\rangle + c_4|2p_z\rangle, \tag{1.20}$$

$$|sp_b^3\rangle = c_5|2s\rangle + c_6|2p_x\rangle + c_7|2p_y\rangle + c_8|2p_z\rangle, \tag{1.21}$$

$$|sp_c^3\rangle = c_9|2s\rangle + c_{10}|2p_x\rangle + c_{11}|2p_x\rangle + c_{12}|2p_z\rangle, \tag{1.22}$$

$$|sp_d^3\rangle = c_{13}|2s\rangle + c_{14}|2p_x\rangle + c_{15}|2p_x\rangle + c_{16}|2p_z\rangle. \tag{1.23}$$

One more time we require the orbitals to have the same form, so $c_1 = c_5 = c_9 = c_{13}$. We can also choose the direction of the first orbital to be, for instance, $(1, 1, 1)$, which can be achieved by setting $c_1 = c_2 = c_3 = c_4 = 1/2$. The other constants are found by applying

the orthonormality condition. After some algebra we obtain

$$|sp_a^3\rangle = \frac{1}{2}|2s\rangle + \frac{1}{2}|2p_x\rangle + \frac{1}{2}|2p_y\rangle + \frac{1}{2}|2p_z\rangle, \tag{1.24}$$

$$|sp_b^3\rangle = \frac{1}{2}|2s\rangle - \frac{1}{2}|2p_x\rangle - \frac{1}{2}|2p_y\rangle + \frac{1}{2}|2p_z\rangle, \tag{1.25}$$

$$|sp_c^3\rangle = \frac{1}{2}|2s\rangle - \frac{1}{2}|2p_x\rangle + \frac{1}{2}|2p_x\rangle - \frac{1}{2}|2p_z\rangle, \tag{1.26}$$

$$|sp_d^3\rangle = \frac{1}{2}|2s\rangle + \frac{1}{2}|2p_x\rangle - \frac{1}{2}|2p_x\rangle - \frac{1}{2}|2p_z\rangle. \tag{1.27}$$

The orbitals sp_b^3, sp_c^3 and sp_d^3 point along the directions $(-1,-1,1)$, $(-1,1,-1)$ and $(1,-1,-1)$, respectively, which means that the axes of the four sp^3 orbitals are arranged like lines joining the center of a regular tetrahedron to its four corners. The angle between any two orbitals is $109°28'$.

This type of hybridization is responsible for the structural form of the diamond, and is also found in the methane molecule CH_4.

1.2 Carbon Materials

Among all the carbon materials found in nature, diamond and graphite are certainly the most popular ones, both of them with well-known and established properties [7]. The first one, object of desire of many ladies, is hard and transparent to the visible spectrum, besides being a good insulator. The latter, on the contrary, is soft, opaque and conductor.

Over the past three decades a great interest in carbon materials has resurfaced with the discover of new materials. In 1985 H. *W. Kroto et al.*, while peforming mass-spectroscopy analysis of carbon vapor, observed a series of even-numbered clusters with 38-120 atoms, being the C_{60} the most stable molecule [8].This new class of carbon allotropes were called fullerenes. Unlike diamond and graphite, the fullerenes are not a single material, but a family of molecular structures in form of spheroids. In order to close into a spheroid the carbon atoms are arranged in groups of twelve pentagons and a variable number of hexagons. In the case of the C_{60} twenty hexagons in addition to the necessary twelve pentagons give it the form of a soccer ball. In 1996 Robert F. Curl Jr., Sir Harold W. Kroto and Richard E. Smalley shared the Nobel prize of chemistry *for their discovery of fullerenes* [9].

In 1991, shortly after the discovery of fullerenes, the first report on *multi-wall carbon nanotubes* (MWCNTs), a new type of carbon structure consisting of needle-like tubes, came out [10]. Following the trend, in 1993, the first observation of single-wall carbon

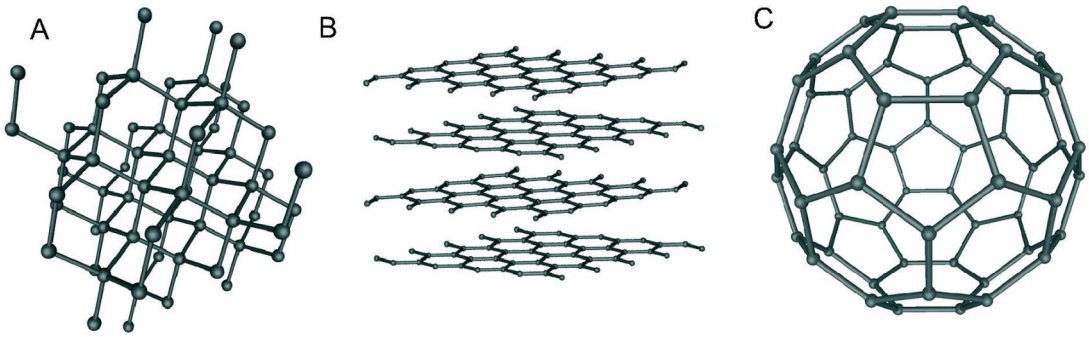

Figure 3: The structural form of three allotropes of carbon:(A) diamond, (B) graphite, (C) fullerene C_{60}.

nanotubes (SWCNTs) were reported [11, 12]. The structure of these nanotubes can be pictured as one or few layers of graphite, depending on whether we deal with SWCNTs or MWCNTs, rolled up into a cylinder whose diameters range from $0,7$ nm to $1,6$ nm (4 nm to 30 nm) for SWCNTs (MWCNTs).

Formally, each nanotube is entirely determined by the chiral vector $\vec{C}_h = n\vec{a}_1 + m\vec{a}_2 = (n, m)$, where n and m are integer numbers with $0 \leq \mid m \mid \leq n$, while a_1 and a_2 define the unit cell of the graphite sheet (see Fig. 4). An equivalent way of characterizing the nanotube is to define its diameter $d = \mid \vec{C}_h \mid /\pi$ and chiral angle

$$\theta = \arccos\left(\frac{\vec{C}_h \cdot \vec{a}_1}{\mid \vec{C}_h \mid\mid \vec{a}_1 \mid}\right) = \arccos\left(\frac{(2n+m)}{2\sqrt{n^2+m^2+nm}}\right) \tag{1.28}$$

that together determine the chiral vector.

Based on the parameters just described, the nanotubes are classified in three groups: armchair, when $m = n$ and $\theta = \pi/6$; zigzag, when $m = 0$ and $\theta = 0$; and chiral, when $0 < \mid m \mid < n$ and $0 < \theta < \pi/6$. Although the three types of nanotubes have similar shapes and are all consisting of carbon, it turns out that the way the graphite layer is rolled up plays a fundamental role in the electronic properties of this material. It was observed that armchair CNTs are metallic, while zigzag and chiral CNTs are metallic when $n - m = 3l$ (l is an integer). In the case $n - m \neq 3l$, CNTs are semiconductors with an energy gap of the order of ~ 0.5 eV, being the energy gap inversely proportional to the diameter d [13].

More recently, in 2004, a new sort of material arose with the first fabrication of truly two-dimensional crystals. While working on graphite thin films, researchers at Manchester University succeeded in isolating films consisting of just few layers of graphite and even one atom thick single layer, named *graphene*. Amazingly, these structures proved to be high quality and stable even under ambient conditions [14, 15, 16], refuting previous

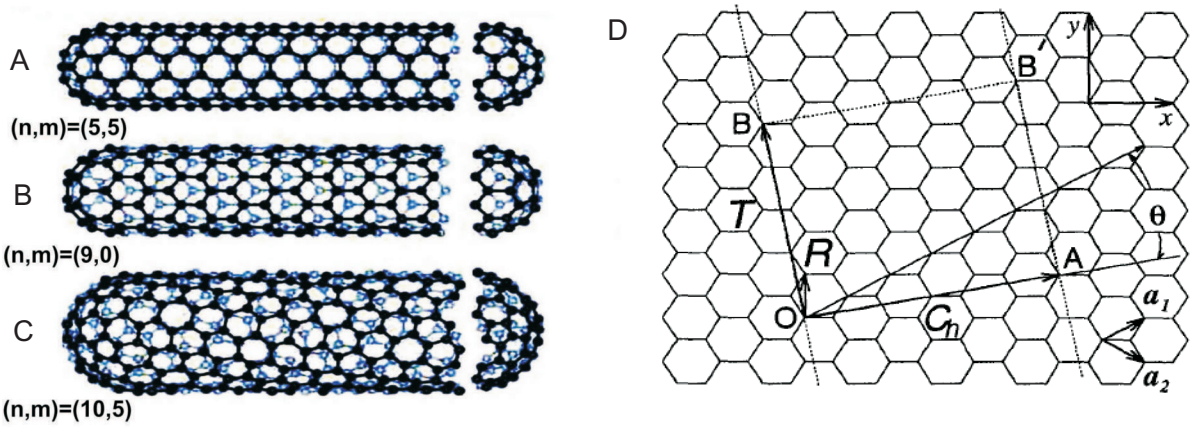

Figure 4: The three types of nanotubes:(A) armchair, (B) zigzag, (C) chiral. (D) Schematic view of an unrolled nanotube, showing the translational and chiral vectors.

theoretical studies that stated such two-dimensional crystals to be thermodynamically unstable [17, 18]. Ever since this first report, graphene has received a lot of attention from the science community, and it has been proving to have very peculiar and interesting properties that could possibly generate new graphene-based electronic devices. As a consequence of this boom in graphene related research, Andre Geim and Konstantin Novoselov were awarded a nobel prize in physics *for groundbreaking experiments regarding the two-dimensional material graphene* [19].

Graphene itself is a two-dimensional crystal made exclusively of carbon atoms arranged in a honeycomb lattice. Each atom is in sp^2 hybridization and is bound to other three, by means of strong σ bonds, forming a trigonal plane structure as discussed before. The pure half-filled p_z orbitals left out of the hybridization are perpendicular to the plane of atoms and make weak delocalized π bonds with the neighbors atoms. In order to try to explain why the π bonds are called delocalized let us think what would be the situation if the bonds were in fact well-localized. In that case, each hexagon would have three alternate double bonds and we would expect that the pair of atoms joined by them would be more tightly bond and consequently, closer to each other. However, all the atoms are apart by the same distance, 0.142 nm. The theoretical explanation for this fact says that the p_z orbital of a given carbon atom is not superposed to an specific neighbor p_z orbital, on the contrary, it is constantly changing the direction of the superposition around the three neighbors, making delocalized π bonds. Then, it is as if the unpaired electrons in the p_z orbitals could hop from atom to atom as the π bonds are formed. These π electrons are the main responsible for the transport properties of graphene [5, 20].

1.3 Graphene Fabrication Techniques

A significant part of the academic research on graphene uses samples obtained by micro-mechanical cleavage, which was the technique used to obtain the first graphene samples [14]. That is an extremely simple and inexpensive technique that basically consists in using a scotch tape to peel off graphene layers from a bulk crystal of HOPG (highly ordered pyrolytic graphite), and then rub the sample onto a 300 nm thick silicon oxide (SiO_2) substrate. The substrate area is covered with different numbers of layers and a key part of the process is to identify the area where there is a single layer of graphene.

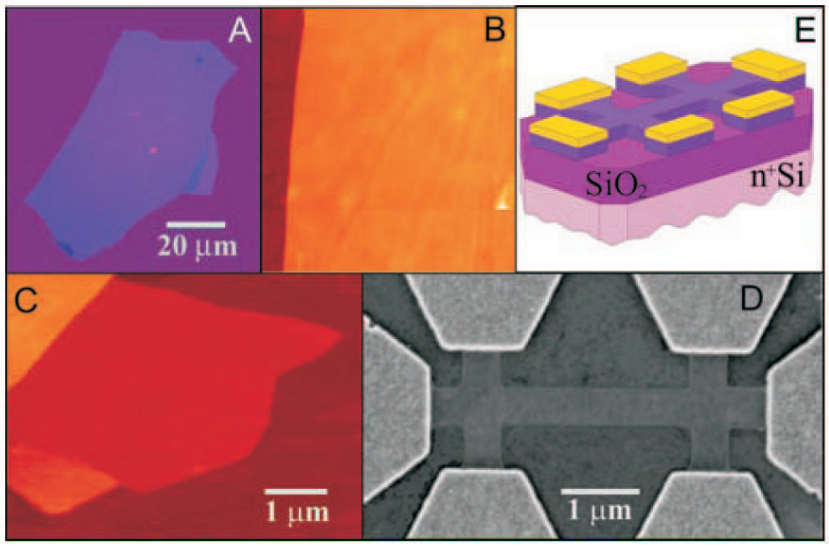

Figure 5: Thin films of graphite. (A) Picture of a $\approx$ 3 nm thick multi-layer graphene. (B) Atomic force microscope (AFM) image of this flake near its edge. The dark brown area is the SiO_2 surface and the orange part corresponds to 3 nm height above the SiO_2 surface.(C) AFM image of single-layer graphene. (D) Scan electronic microscope (SEM) image of an experimental device prepared from few-layer graphene. (E) Schematic view of the device in (D) [14].

Graphite films less than 50 nm thick are transparent under the optical microscope (OM). Nonetheless, due to an addition on the optical path, films with different thicknesses have unique interference patterns on the SiO_2 substrate, producing different colorings. The color for 300 nm SiO_2 wafer is violet-blue and the extra thickness d due graphite films shifts the color to blue. Then, the role of the OM is define the region where the monolayer is most likely located, while the further task of identifying the single-layer is carried out using the atomic force microscope (AFM), since films with thickness $d < 1.5$ nm are no longer visible even by way of interference shift [21].

Although this mechanical exfoliation is a rather simple technique, which makes the academic research on graphene possible in many research groups, this kind of fabrication is unfeasible for large scale production of graphene-based devices. Consequently, more sophisticated techniques are needed, such as: chemical vapor deposition (CVD) and epitaxial growth by thermal decomposition of Silicon carbide SiC.

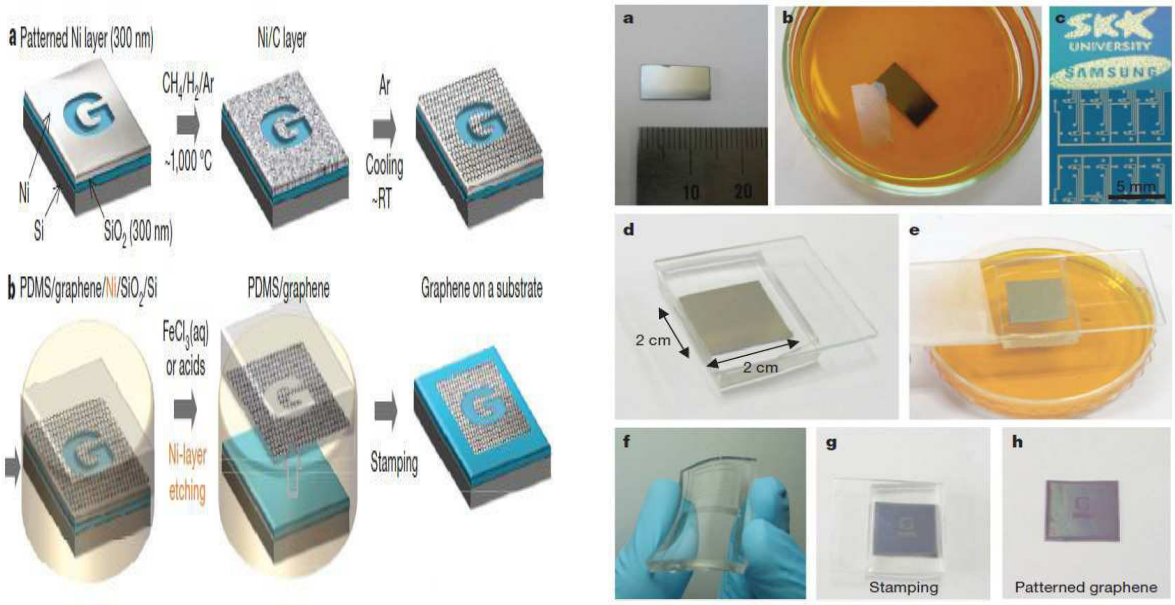

Figure 6: (Left panel) **a** Synthesis of patterned graphene films on thin nickel layers. **b** Removing Ni using FeCl3 (or acids) and transfer of graphene films using a PDMS stamp. (Right panel) **a** A centimetre-scale graphene film grown on a Ni(300 nm)/SiO2(300 nm)/Si substrate. **b** A floating graphene film after etching the nickel layers in 1M FeCl3 aqueous solution. After the removal of the nickel layers, the floating graphene film can be transferred by direct contact with substrates. **c** Various shapes of graphene films can be synthesized on top of patterned nickel layers. **d**,**e** The dry-transfer method based on a PDMS stamp is useful in transferring the patterned graphene films. After attaching the PDMS substrate to the graphene (**d**), the underlying nickel layer is etched and removed using FeCl3 solution (**e**). **f** Graphene films on the PDMS substrates are transparent and flexible. **g**,**h** ThePDMSstamp makes conformal contact with a silicon dioxide substrate. Peeling back the stamp (**g**) leaves the film on a SiO2 substrate (**h**) [26].

By means of chemical vapor deposition it is possible to make large area graphene samples (order of cm^2) that can be seen with naked eye. This technique has been applied to produce layers that can be used as stretchable transparent electrodes for touch screens. The growth is made on the top of metal substrates such as Nickel Ni [25, 26, 27] and Cooper Cu [28, 27]. The left panel in Fig. 6 illustrates all the steps of the process: from the growth of the graphene sample on the top of etched Ni crystal (**a**) to the separation of the Ni/graphene and the deposition of the graphene layer onto a polydimethylsiloxane (PDMS) soft substrate (**b**). The left panel in Fig. 6 shows pictures of the actual process.

When one is interested in nanostructured graphene, epitaxial growth (EG) on SiC is probably the most suitable fabrication technique. One can highlight three features that make it a promising method: first, it is compatible with the large-scale electronics processing methods, since the graphene structure is oriented grown with respect to the SiC large gap semiconductor substrate; second, the high temperatures involved in the fabrication process ensure contamination-free and defect-free samples with well-defined interfaces; in addition, the growth on structured SiC surfaces permits the production of graphene nanostructures without post-growth lithograthy process, resulting in atomically smooth edges structures that are fundamental in controlling electronic properties of the material. [22, 24].

The EG technique itself consists of the high-vacuum thermal decomposition of SiC. The silicon carbide is annealed at temperatures above 1500 K, at this stage the Silicon atoms sublimate leaving the graphene layers. The quality, smoothness and width of the graphene layers can be better controlled by processing the sample in inert gas atmosphere instead of high vacuum. Doing this one can increase the temperature without necessarily increasing the sublimation rate, once the gas pressure helps to control the sublimation rate [23]. Another possibility is to enclose the sample in a furnace with a leak that can control the pressure of the sublimated Si gas (see Fig. 7(B)) [24]. It is worth to mention that the electronic and structural quality of the samples strongly depends on which face of the SiC the growth is made. The samples grown on the C-terminated face usually have larger areas and higher mobilities than those grown on Si-terminated face.

1.4 What makes graphene interesting?

Although many theoretical studies on graphene have been done over the last 60 years [29, 30, 31], the experimental realization of this material is still a fresh event that keep attracting people's interests. Besides belonging to a new and unexpected group of materials, the two-dimensional crystals, graphene has a variety of odd properties that attracted a lot of attention from the academic community.

A single graphene sheet exhibit exceptional electronic quality. The first Measurements performed in this material revelled high mobilities μ, achieving values as high as $15,000$ $\mathrm{cm}^2/\mathrm{Vs}$ at room temperature [14, 16, 33, 34]. In addition, it was observed that μ values were nearly independent of the temperature. This fact gave an indication that the value of μ, for instance, at 300 K was still limited by scattering process by impurities [32]. In

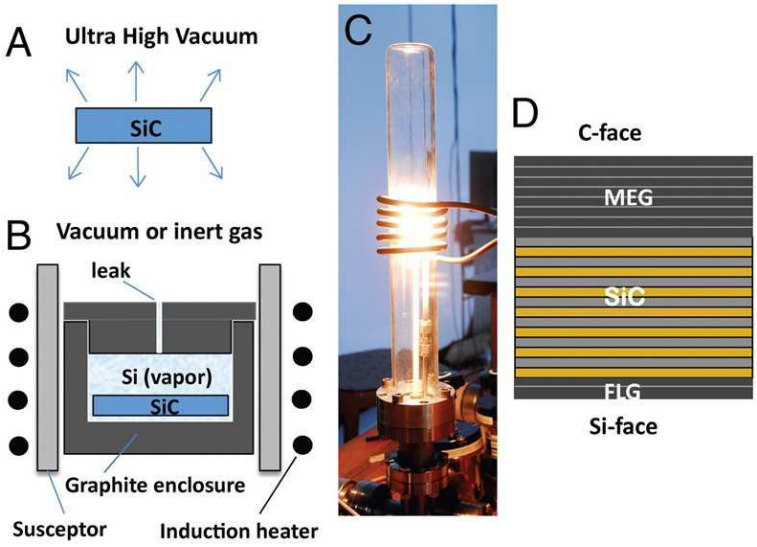

Figure 7: (A) SiC wafer in ultra high vacuum: sublimed silicon is not confined, causing rapid, out of equilibrium graphene growth. (B) The confinement sublimation method: sublimed Si gas is confined in a graphite enclosure so that growth occurs in near thermodynamic equilibrium. Growth rate is controlled by the enclosure aperture (leak), and the background gas pressure. (C) Photograph of the induction furnace. (D) Under these conditions few layer graphite (FLG, from 1 to 10 layers) grows on the Si-terminated face, and multilayer epitaxial graphene (MEG, from 1 to 100 layers) grows on the C-terminated face.[24]

fact, more recent experiments succeed to obtain mobilities higher than $200,000$ cm^2/Vs [35] at room temperature, which exceed the μ values known for any other semiconductor [36].

From a fundamental point of view, maybe the most striking feature of graphene is that its charge carriers are governed by the Dirac equation, the same equation that rules the spin 1/2 particles in quantum electrodynamics [37]. As a consequence, it is usually stated that electrons in graphene behave like zero-mass relativistic particles that travel with an effective speed of light $v_F = 10^6$ m/s (see chapter 2), exhibiting a gapless conical spectrum at low energies ($E < 1$ eV). Some effects arising from this fact are: ambipolar electric field effect (AEFE), minimum conductivity, anomalous quantum Hall effect and Klein tunnelling.

By AEFE we can understand that the charge carriers can be continuously changed from holes to electrons by just changing the electric field direction. Fig. 8 shows a measurement of this effect in graphene. The conductivity increases linearly with the gate voltage V_g, changing its sign around $V_g = 0$. This behavior suggests that, by means of adding or subtracting electrons from the substrate, a positive (negative) gate voltages induce electrons (holes) concentration on graphene.

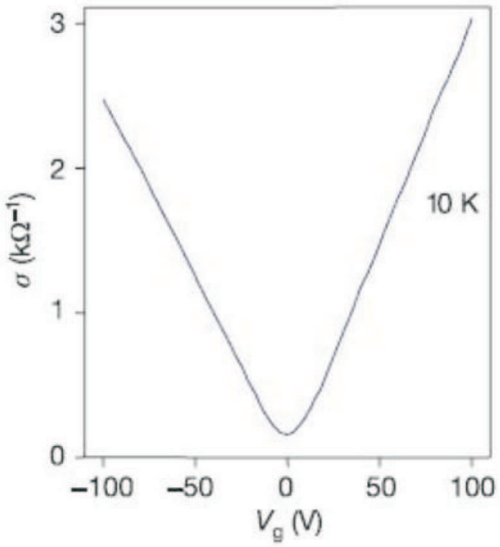

Figure 8: Ambipolar electric field effect in graphene [33].

It is well-known that the quantum Hall effect (QHE) describes the Hall conductivity σ_{xy} quantization. Differently from the classical version, where σ_{xy} depends linearly on the magnetic field, in the QH regime, σ_{xy} exhibits plateaus at integer multiples of e^2/h [38]. Unlike an ordinary 2DEG, in graphene it was found that the plateaus are shifted by half of the expected values, presenting $\sigma_{xy} = \pm 4e^2/h(n + 1/2)$ quantization [33, 34], where factor 4 appears due the valley and spin degeneracy and n is the Landau level (LL) index. This behavior is explained as a consequence of an unique LL spectrum $E_n = \pm v_F\sqrt{2e\hbar Bn}$ that allows a zero energy level which is shared for both electrons and holes. Figure 9(a) shows the behavior of the Hall conductivity σ_{xy} and the longitudinal resistivity ρ_{xx} as a function of the density of carries for a graphene sample under a 14 T magnetic field for a temperature of 4 K. Another experimental indication of the high electronic quality of graphene was the room temperature QHE observation [39] (see Fig. 9(b)). Usually the QH regime requires very low temperatures, lower than the boiling point of liquid helium. Some factors that allowed this observation in graphene are the high density of carriers (up to 10^{13} cm^{-2}) which populates the lowest LL even at very high magnetic fields, and the high mobility of the sample.

Another peculiar characteristic of the charge carriers in graphene emerges when one try to confine then by means of electrostatic potentials. Electrons in graphene can not be trapped by such structures, they can tunnel any electrostatic barrier with a 100% probability [40]. Figure 10 illustrates how the the tunnelling happens: when the incoming electron in the red branch hits the barrier it always finds a hole state available at the

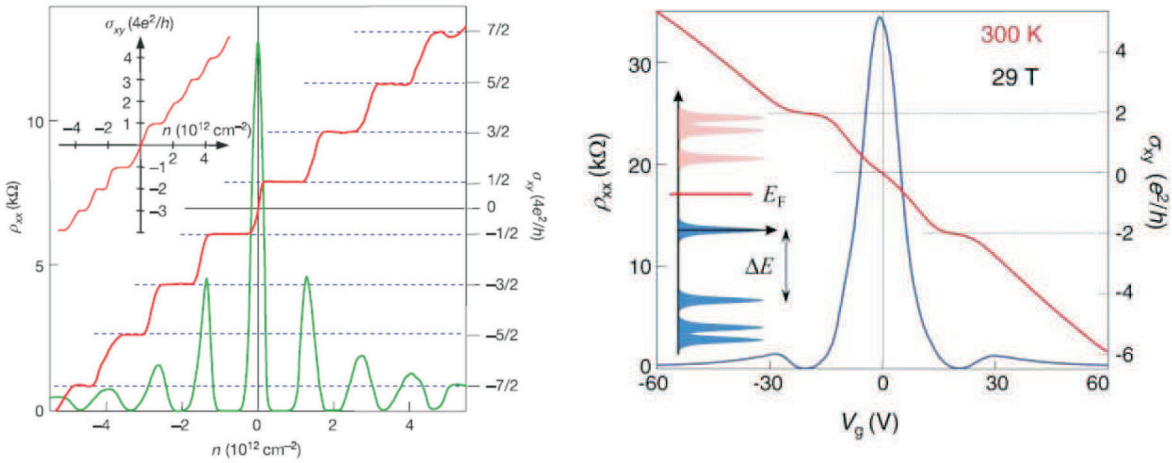

(a) (b)

Figure 9: (a) Hall conductivity and longitudinal resistivity as a function of the density of carriers in graphene at $B = 14$ T and temperature of 4 K [33]. (b) Room-temperature QHE in graphene [39].

same branch through which it can propagate [4]. This effect is usually mentioned as Klein paradox or Klein tunnelling in graphene, in analogy to the so called Klein paradox in quantum electrodynamics, where particles start to penetrate a potential barrier when its height exceeds $2mc^2$. From this point on the transmission is approximately independent of the height of the barrier and approaches to 1 for very high barriers.

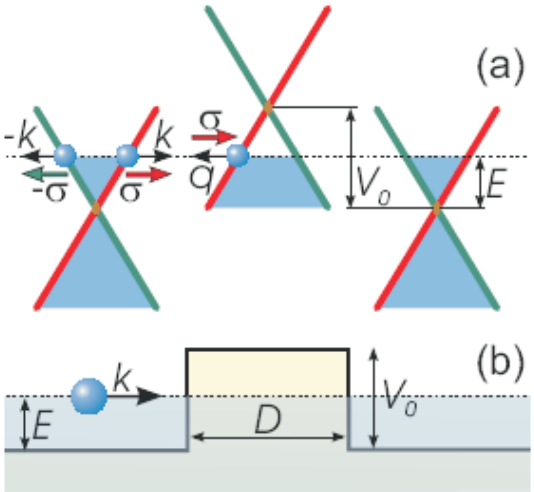

Figure 10: (a) Schematic view of graphene low energy bands. The blue filling indicates occupied states. The three diagrams illustrates the position of the Fermi energy through the barrier potential showed in (b) [40].

[4] For an interesting way of understanding this effect read [41]

Owing to the features just reported and many others not included here, there is a great spirit in generating technology by exploring the new physics of graphene. Some possibilities were already explored, such as using graphene as a gas sensor [42]. *Schedin et al* reported that graphene can be used to detect even a single molecule by means of measurable changes in its electric resistivity. Since graphene is an excellent conductor, another possible application is create graphene transistors, which eliminates the need for metallic junctions, making possible to miniaturize even more the current electronic devices. On the other hand, the problem of switching off the current still remains (Klein tunnelling). Because of that, now the aim is try to combine graphene and semiconductor materials in order to take advantage of the exceptional electronic quality of graphene and still be able to control the on/off current [43, 44]. Large graphene samples fabricated by CVD technique were also used to replace indium tin oxides electrodes in flexible touch screen panel devices [26, 27].

1.5 Outline

Along the subsequent chapter, we will develop the mathematical framework that helps to explain the basic electronic properties of graphene. More precisely, we will present the tight-binding model applied to graphene and perform the continuum limit approximation in order to obtain an effective Hamiltonian valid for a low density of carriers, which allows the analogy with quantum electrodynamics. The formation of the Landau levels as a result of an applied external magnetic field is also analyzed.

In chapter 3, we turn our attention to graphene nanoribbons, a system where the edge details strongly influence its electronic properties. In this context, we use the tight-binding model to study the effect of a simple shear strain on the electronic spectrum of zigzag and armchair ribbons.

In chapter 4, the stacking of two and three layers of graphene are introduced and their free electron spectra are presented. The effect of the gate voltage on the gap opening, as well as the role played by the stacking order of the trilayer graphene in the spectrum, is analyzed.

Chapter 5 and 6 are devoted to the study of the Landau Levels on differently stacked trilayer graphene and their transitions. In the former, starting from the 6×6 Hamiltonian we obtain analytical expressions for the energy levels of ABA and ABC trilayers in external magnetic field. While, in the latter, we obtain the spinor wavefunctions and calculate,

within the dipole approximation, the oscillator strengths of the allowed transitions, as well as the cyclotron resonance spectrum.

Finally, in chapter 7 we summarize the main results.

2 Graphene's basic electronic properties

This chapter is devoted to deriving the basic electronic properties of graphene. It starts by developing the tight-binding model for graphene, followed by the continuum model approximation that leads to a low-energy effective Hamiltonian. Finally, the formation of Landau levels as a result of an applied homogeneous magnetic field is described.

2.1 Tight-binding Approximation

Let us start describing the crystalline structure of the considered material. Graphene is made of carbon atoms arranged in a two-dimensional honeycomb lattice. This kind of arrangement does not constitute a Bravais lattice, however it can be considered as two superposed triangular sublattices A and B, or yet a single triangular lattice with a base of two atoms in the unit cell [29]. The primitive vectors are given by:

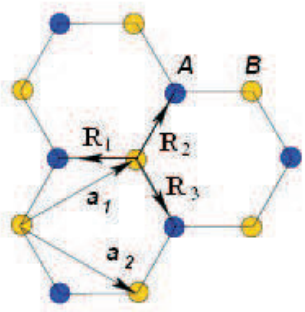

Figure 11: The crystalline structure of graphene with two sublattices A and B. $\mathbf{a_1}$ and $\mathbf{a_2}$ are the primitive vectors that span the lattice, while $\mathbf{R}_i$ (with $i = 1, 2, 3$) localize the nearest neighbors.[45]

$$\vec{a}_1 = \frac{3a}{2}\hat{x} + \frac{\sqrt{3}a}{2}\hat{y}, \quad \vec{a}_2 = \frac{3a}{2}\hat{x} - \frac{\sqrt{3}a}{2}\hat{y}, \tag{2.1}$$

where $a \approx 1,42\ \mathring{A}$ is the $C-C$ distance, $\hat{x}$ and $\hat{y}$ are the unit vectors along x and y-directions, respectively. The vectors defining the reciprocal lattice are the followings:

$$\vec{b}_1 = \frac{2\pi}{3a}\hat{x} + \frac{2\sqrt{3}\pi}{3a}\hat{y}, \quad \vec{b}_2 = \frac{2\pi}{3a}\hat{x} - \frac{2\sqrt{3}\pi}{3a}\hat{y}. \tag{2.2}$$

Now that we have defined graphene from the crystallographic point of view, let us focus on the tight-binding approximation itself. The tight-binding model is one of the most simple microscopic description of electrons in a crystal. The basic idea behind this model is to assume that the electron is tightly bound to the atom, such that its wave function is peaked at the atomic site. As consequence, the wave function of the crystal can be expanded in terms of the wave functions of isolated atoms. Here we are going to consider that the range of the atomic wave function is of the order of the lattice spacing a, which means that the electron can just hop between the nearest neighbors (NN). In addition, we are going to leave out the $\sigma-$orbitals and consider just the $\pi-$orbitals, since the π bands are the most important for determining the solid state properties of graphene when one is interested in low-energy excitations [5].

In second quantization language, tight-biding Hamiltonian that describes electrons in graphene [1], including only the hopping between the NN [2], can be written as:

$$\mathbf{H} = -\sum_{i,j} \gamma_0 (\mathbf{a}_i^\dagger \mathbf{b}_j + \mathbf{b}_j^\dagger \mathbf{a}_i), \tag{2.3}$$

where $\gamma_0 \approx 2,8\ eV$ [45] is the NN hopping parameter. The operators $\mathbf{a}_i^\dagger$ and $\mathbf{a}_i$ create and annihilate electrons on the site i of the sublattice A , respectively, whereas $\mathbf{b}_j^\dagger$ and $\mathbf{b}_j$ act likewise on the j-sites of sublattice B.

By considering an infinite ideal lattice, it is possible to perform a Fourier transformation of the creation and annihilation operators. In order to do so, let us write

$$\mathbf{a}_i = \frac{1}{\sqrt{N}} \sum_k e^{i\vec{k}\cdot\vec{r}_i} \mathbf{a}_k, \quad \mathbf{a}_i^\dagger = \frac{1}{\sqrt{N}} \sum_k e^{-i\vec{k}\cdot\vec{r}_i} \mathbf{a}_k^\dagger \tag{2.4}$$

$$\mathbf{b}_j = \frac{1}{\sqrt{N}} \sum_{k'} e^{i\vec{k}'\cdot\vec{r}_j} \mathbf{b}_{k'}, \quad \mathbf{b}_j^\dagger = \frac{1}{\sqrt{N}} \sum_{k'} e^{-i\vec{k}'\cdot\vec{r}_j} \mathbf{b}_{k'}^\dagger\ . \tag{2.5}$$

[1] Although the treatment of this problem in first quantization language is more intuitive, we have chosen the second quantization because of the cleanness and simplicity of its notation. The reader interested in the former treatment can find it on the second chapter of reference [5].

[2] The term that accounts for on-site energy was omitted, since A and B atoms are both carbon atoms with the same on-site energy and its presence in Hamiltonian would simply cause a shift in the spectrum.

Substituting (2.4) e (2.5) into (2.3), the Hamiltonian takes the form of

$$\mathbf{H} = -\sum_{i,j}\frac{\gamma_0}{N}\left[\sum_{k,k'} e^{-i\vec{k}\cdot\vec{r}_i}e^{i\vec{k}'\cdot\vec{r}_j}\mathbf{a}_k^\dagger\mathbf{b}_{k'} + \sum_{k,k'} e^{-i\vec{k}'\cdot\vec{r}_j}e^{i\vec{k}\cdot\vec{r}_i}\mathbf{b}_{k'}^\dagger\mathbf{a}_k\right], \tag{2.6}$$

which can be rewritten as:

$$\mathbf{H} = -\frac{\gamma_0}{N}\sum_{i,j}\sum_{k,k'}[e^{-i(\vec{k}-\vec{k}')\cdot\vec{r}_i}e^{i\vec{k}'\cdot(\vec{r}_j-\vec{r}_i)}\mathbf{a}_k^\dagger\mathbf{b}_{k'} + e^{-i(\vec{k}'-\vec{k})\cdot\vec{r}_i}e^{-i\vec{k}'\cdot(\vec{r}_j-\vec{r}_i)}\mathbf{b}_{k'}^\dagger\mathbf{a}_k]. \tag{2.7}$$

Since each atom has three nearest neighbors (NN), if we put the origin of the system on a site i and make j vary over the NN, localized by $\vec{R}_1 = (-a, 0)$, $\vec{R}_2 = \big(a/2, a\sqrt{3}/2\big)$, $\vec{R}_3 = \big(a/2, -a\sqrt{3}/2\big)$, we obtain:

$$\begin{aligned}\mathbf{H} = -\frac{\gamma_0}{N}\sum_{i}\sum_{k,k'}[&e^{-i(\vec{k}-\vec{k}')\cdot\vec{r}_i}\mathbf{a}_k^\dagger\mathbf{b}_{k'}(e^{-ik_x'a} + e^{ik_x'a/2}e^{ik_y'\sqrt{3}a/2} + e^{ik_x'a/2}e^{-ik_y'\sqrt{3}a/2})\\ &+e^{-i(\vec{k}'-\vec{k})\cdot\vec{r}_i}\mathbf{b}_{k'}^\dagger\mathbf{a}_k(e^{ik_x'a} + e^{-ik_x'a/2}e^{-ik_y'\sqrt{3}a/2} + e^{-ik_x'a/2}e^{ik_y'\sqrt{3}a/2})]\end{aligned} \tag{2.8}$$

$$\mathbf{H} = -\gamma_0\sum_{k}[g(\vec{k})\mathbf{a}_k^\dagger\mathbf{b}_k + g^*(\vec{k})\mathbf{b}_k^\dagger\mathbf{a}_k], \tag{2.9}$$

where

$$g(\vec{k}) = e^{ik_xa} + 2\cos(k_y\sqrt{3}a/2)e^{-ik_xa/2} \tag{2.10}$$

is the structure factor of the crystal. Note that the above Hamiltonian can be written as

$$\mathbf{H} = \sum_k\langle\Psi_k|\mathbf{H}_k|\Psi_k\rangle \tag{2.11}$$

where $|\Psi_k\rangle = (\mathbf{a}_k \;\; \mathbf{b}_k)^T$ and $\mathbf{H}_k$ represent the electronic state and the Hamiltonian for a given $\vec{k}$, respectively. The $\mathbf{H}_k$ is

$$\mathbf{H}_k = \begin{pmatrix} 0 & -\gamma_0 g(\vec{k}) \\ -\gamma_0 g^*(\vec{k}) & 0 \end{pmatrix}. \tag{2.12}$$

The eigenvalues of $\mathbf{H}_k$ can be easily obtained as

$$E\pm_k = \pm\;\; \gamma_0|g(\vec{k})| = \pm\;\; \gamma_0\sqrt{3 + f(\vec{k})}, \tag{2.13}$$

with $f(\vec{k}) = 4\cos(3k_xa/2)\cos(\sqrt{3}k_ya/2) + 2\cos(\sqrt{3}k_ya)$.

Figure 12 exhibits the electronic band structure found in Eq. (2.13). The structure

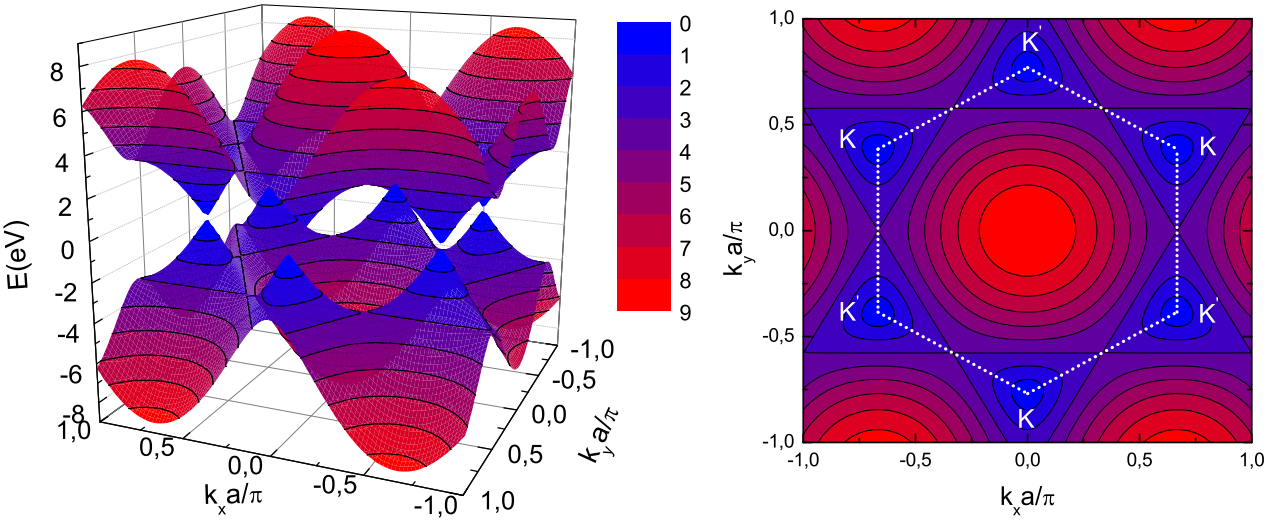

(a) (b)

Figure 12: (a) The π bands of graphene obtained by the tight-biding approximation. (b) The contour plot of the conduction band on first Brillouin zone (white dotted line).

is composed of two parts: the valence ($E_v \leq 0$) and conduction ($E_c \geq 0$) bands [3]. These bands touch at six points in the reciprocal space, the so called Dirac points. In order to find their coordinates we have to find the points where $E(k_x, k_y) = 0$, which means $g(k_x, k_y) = 0$. This requirement is fulfilled when

$$Re[g(k_x, k_y)] = \cos k_x a + 2\cos k_y\sqrt{3}a/2\cos k_x a/2 = 0, \tag{2.14}$$

and

$$Im[g(k_x, k_y)] = \sin k_x a - 2\cos k_y\sqrt{3}a/2\sin k_x a/2 = 0, \tag{2.15}$$

which lead to

$$\begin{aligned} \vec{k_1} &= \left(0, \tfrac{-4\pi}{3\sqrt{3}a}\right), \quad \vec{k_3} = \left(\tfrac{-2\pi}{3a}, \tfrac{2\pi}{3\sqrt{3}a}\right), \quad \vec{k_5} = \left(\tfrac{2\pi}{3a}, \tfrac{2\pi}{3\sqrt{3}a}\right), \\ \vec{k_2} &= \left(\tfrac{-2\pi}{3a}, \tfrac{-2\pi}{3\sqrt{3}a}\right), \quad \vec{k_4} = \left(0, \tfrac{4\pi}{3\sqrt{3}a}\right), \quad \vec{k_6} = \left(\tfrac{2\pi}{3a}, \tfrac{-2\pi}{3\sqrt{3}a}\right). \end{aligned} \tag{2.16}$$

Coincidentally, these points are located at the crystallographic points K and K' in the corner of the first Brillouin zone. Then, the points $\vec{k_1}$, $\vec{k_3}$ and $\vec{k_5}$ ($\vec{k_2}$, $\vec{k_4}$ and $\vec{k_6}$) are equivalents, since they are associated to the K (K') points that are connected by the

[3] It is worth to mention that the electronic dispersion in Fig. 12 has electron-hole symmetry, which means that $E_c = -E_v$. This symmetry just occurs because we have neglected the electronic hopping between the next-near neighbors atoms.

reciprocal lattice vector $\vec{G}$.

2.2 Continuum Model

The Dirac points are of particular importance for the investigation of the electronic properties of graphene, since the Fermi energy lies on the Dirac points[4][46] and, for low-energy excitations, the only electrons involved in the physical process are the ones around the Fermi level. Because of that it can be useful obtain an approximate Hamiltonian for wave vectors around the K and K' points. When such approximation is made we lose microscopic information of the system, and then, it is said that we move from a discrete to a continuum model. In order to do that, let us expand the nonzero terms of the Hamiltonian in (2.12) in Taylor's series around these points an retain just the first order terms in k_x and k_y. For the sake of simplicity, we perform the expansion of $g(k_x, k_y)$ around $\vec{k_1}$ and obtain:

$$g(\delta\vec{k}) \approx g(\vec{k_1}) + \frac{\partial g}{\partial k_x}\Big|_{\vec{k}=\vec{k_1}}(k_x - k_{1x}) + \frac{\partial g}{\partial k_y}\Big|_{\vec{k}=\vec{k_1}}(k_y - k_{1y}) + O(\delta k^2), \tag{2.17}$$

where $\delta\vec{k} = \vec{k} - \vec{k_1}$. After evaluating $g(\vec{k})$ and its derivatives at $\vec{k_1}$ we obtain:

$$g(\delta\vec{k}) \approx \frac{3a}{2}e^{i\pi/2}(k_x - ik_y). \tag{2.18}$$

The phase $e^{i\pi/2}$ appearing on the right side of the Eq. (2.18) can be included in the eigenstate without no physical change, since its norm is one[5]. Then, the Hamiltonian describing the states around the $\vec{k_1}$ (K) point is

$$\mathbf{H}_K = \begin{pmatrix} 0 & \hbar v_F(k_x - ik_y) \\ \hbar v_F(k_x + ik_y) & 0 \end{pmatrix}, \tag{2.19}$$

with $\hbar v_F = 3a\gamma_0/2$. This Hamiltonian has exactly the same form of the two-dimensional Dirac Hamiltonian that describes relativistic electrons with a zero mass, but in this case, the light velocity c is replaced by the Fermi velocity $v_F \approx 1 \times 10^6$ m/s [46]. That is the reason why it is commonly said that electrons in graphene behave like massless relativistic

[4]Recalling that each carbon atom contributes with an unpaired π electron and that each energy state accommodates two electrons (spin up and down), the band should be completely filled up to the top (bottom) of the valence (conduction) band.

[5]If the same approximation had been made around the other K points we would have got the same Hamiltonian, however the eigenstates would have different phase factors: $e^{i7\pi/6}$ in k_5, and $e^{i11\pi/6}$ in k_3.

fermions. The equation (2.19) can be rewritten in a succinct way as

$$\mathbf{H}_K = v_F \boldsymbol{\sigma} \cdot \boldsymbol{p}, \tag{2.20}$$

where $\boldsymbol{\sigma} = (\sigma_x, \sigma_y, \sigma_z)$ are the Pauli matrices. In the original Dirac approach, the Pauli matrices are related to the spin degree of freedom. Nevertheless, in this case the spin was not taken into account, and the σ operator appears as a consequence of the crystallographic structure of graphene. Because of that $\boldsymbol{\sigma}$ is called *sublattice pseudospin* and the eigenstate $|\Psi_K\rangle = (\psi_A, \psi_B)$ is called a pseudospinor, where ψ_A (ψ_B) gives the probability of finding the electron on the A (B) sublattice. Diagonalizing the above Hamiltonian we find a spectrum $E = \pm\hbar v_F k$ [6] that is linear in k and the corresponding eigenstates

$$|\Psi_K^{\pm}\rangle = \frac{1}{\sqrt{2}} \begin{pmatrix} 1 \\ \pm e^{i\theta} \end{pmatrix}, \tag{2.21}$$

with $\theta = \arctan(k_y/k_x)$.

If we go through the same approximation around the $\vec{K'}$ ($\vec{k_4}$) point, we will find that

$$\mathbf{H}_{K'} = v_F \boldsymbol{\sigma}^* \cdot \boldsymbol{p}, \tag{2.22}$$

$$|\Psi_{K'}^{\pm}\rangle = \frac{1}{\sqrt{2}} \begin{pmatrix} 1 \\ \pm e^{-i\theta} \end{pmatrix}. \tag{2.23}$$

The Hamiltonian around the pair of Dirac points are related to each other through the time-reversal symmetry, which states that $\mathbf{H}_k = \mathbf{H}_{-k}^*$, and, consequently, they exhibit the same energy spectrum.

The equation describing the low-energy electronic excitations in graphene is then given by the contribution of the two nonequivalent $\vec{K}$ and $\vec{K'}$ points as follows:

$$\begin{pmatrix} v_F \boldsymbol{\sigma} \cdot \boldsymbol{p} & 0 \\ 0 & v_F \boldsymbol{\sigma}^* \cdot \boldsymbol{p} \end{pmatrix} |\Psi\rangle = E|\Psi\rangle, \tag{2.24}$$

with $E = \pm\hbar v_F k$ and $|\Psi\rangle = (\psi_K, \psi_K') = (\psi_A, \psi_B, \psi_A', \psi_B')^T$. In the absence of off-diagonal terms that scatter the electron from K to K' and vice-versa, the states corresponding to these points are said to be *valley degenerated*, and because of that, from now on, we will work only with $\mathbf{H}_K$.

Figure 13 exhibits a direct experimental measurement of graphene's valence band

[6] This is a striking difference between graphene and the usual 2D electron gas (2DEG), where $E = \hbar^2 k^2/2m$. In the usual 2DEG the Fermi velocity $v_F = \hbar k/m = \sqrt{2E/m}$ of the carriers increase as we increase the energy, while in graphene the Fermi velocity does not depend on the energy.

by means of Angle-resolved photoemission spectroscopy (ARPES) [47], which shows the linear spectrum and the appearence of two Dirac cones, confirming that the continuum model is in fact a good approximation for energies lower than 1 eV.

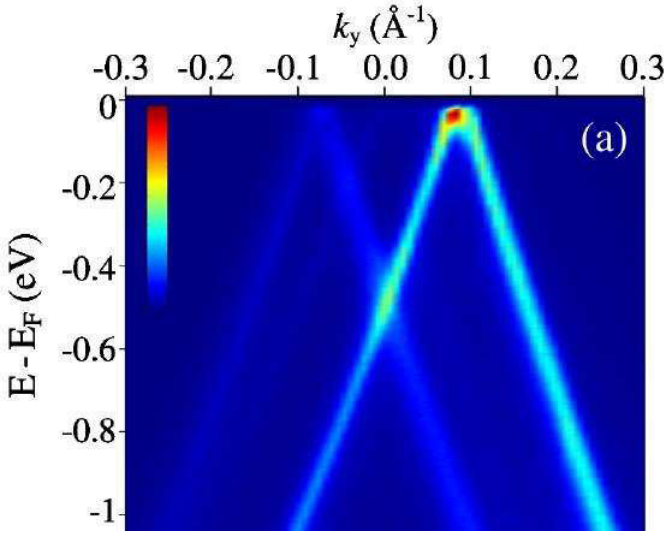

Figure 13: Direct measurement of graphene's valence band by means of Angle-resolved photoemission spectroscopy (ARPES)[47].

2.3 Graphene in Homogeneous Magnetic Field

When we are describing free electrons in the presence of an external magnetic field, the canonical momentum gives place to the kinetic momentum in the Hamiltonian[7], and we have $\mathbf{p} \to \mathbf{p} + e\mathbf{A}$, where e is the absolute value of the electric charge and $\mathbf{A}$ is the vector potential. Then, the Hamiltonian for graphene is written as

$$\mathbf{H} = v_F \boldsymbol{\sigma} \cdot (\boldsymbol{p} + e\boldsymbol{A}). \tag{2.25}$$

Let us treat the case for an uniform magnetic field $\mathbf{B} = B\hat{z}$ generated by the Landau gauge $\mathbf{A} = Bx\hat{y}$. The eigenvalue problem we have to solve is

$$-i\hbar v_F \begin{pmatrix} 0 & \frac{\partial}{\partial x} - i\left(\frac{\partial}{\partial y} + i\frac{eB}{\hbar}x\right) \\ \frac{\partial}{\partial x} + i\left(\frac{\partial}{\partial y} + i\frac{eB}{\hbar}x\right) & 0 \end{pmatrix} \Psi = E\Psi, \tag{2.26}$$

with $\Psi = (\psi_A(x,y) \;\; \psi_B(x,y))^T$. Since the y coordinate does not appear in the Hamiltonian, $[\mathbf{H}, \mathbf{p}_y] = 0$ which means the eigenstates of the Hamiltonian should be also

[7]For a better understanding of the difference between kinetic momentum and canonical momentum read appendix III of [48].

eigenstates of $\mathbf{p}_y$ with eigenvalue given by $\hbar k_y$. Consequently, we can write $\psi_C(x,y) = e^{ik_y y}\varphi_C(x)$, with $C = A,\ B$. Then the Eq. (2.26) takes the form

$$\left(\frac{d}{d\bar{x}} + l_B k_y + \bar{x}\right) = i\frac{E\ell_B}{\hbar v_F}\varphi_A \tag{2.27}$$

$$\left(\frac{d}{d\bar{x}} - l_B k_y - \bar{x}\right) = i\frac{E\ell_B}{\hbar v_F}\varphi_B, \tag{2.28}$$

where we have defined $\ell_B = \sqrt{\frac{\hbar}{eB}}$, and $\bar{x} = x/\ell_B$. If we decouple the above equations for the φ_B component, we end up with the following second-order differential equation

$$\left(\frac{d^2}{d\bar{x}^2} - (x + \ell_B k_y)^2 + \frac{\ell_B^2 E^2}{\hbar^2 v_F^2} + 1\right)\varphi_B = 0. \tag{2.29}$$

This well-known equation just have physical solutions that converge for all $\bar{x}$ values when

$$\frac{\ell_B^2 E^2}{\hbar^2 v_F^2} + 1 = 2n + 1, \tag{2.30}$$

with n being a non-negative integer. Then, we obtain a discrete spectrum given by the Landau levels (LL)

$$E_n = \pm\frac{\hbar v_F}{\ell_B}\sqrt{2n}, \tag{2.31}$$

and wave functions

$$\Psi_n(x,y) = A_n e^{ik_y y} e^{-(\bar{x}+l_B k_y)^2/2}\begin{bmatrix} \mp i\sqrt{2n}\mathcal{H}_{n-1}(\bar{x}+l_B k_y) \\ \mathcal{H}_n(\bar{x}+l_B k_y) \end{bmatrix}, \tag{2.32}$$

where

$$A_n = \begin{cases} \left(\frac{1}{\sqrt{\pi}}\right)^{1/2}, & n = 0 \\ \left(\frac{1}{\sqrt{\pi}2^{n+1}n!}\right)^{1/2}, & n > 0 \end{cases} \tag{2.33}$$

and $\mathcal{H}_n$ stand for the Hermite polynomials.

Note that if we had solved the Eqs. (2.27) and (2.28) for the φ_A component, we would have found that $E_n = \pm\frac{\hbar v_F}{\ell_B}\sqrt{2(n+1)}$. There are two aspects that are worth highlighting. First, the LL in graphene are unequally spaced and follow a $\sqrt{B}$ dependence, which is a peculiar behavior, since the LLs of ordinary 2DEG have a set of equally spaced levels $E_n = \hbar\frac{eB}{m}(n+1/2)$ with a linear B-dependence. Another new feature found is the presence of $E = 0$ LL, which is supported just by the φ_B component of the wave function[8], leading to the half-degeneracy of the 0 level [33, 34].

[8]If we were solving the problem around the K' point, we would find that when $E = 0$ just the φ_A component survive. Because of that, it is usually said that the 0 level is valley-polarized.

The odd behavior of the LL in graphene was experimentally verified by means of infrared spectroscopy [49, 50, 51, 52]. Roughly speaking, this technique consists of shining light on a graphene sample and observing for which energy of the incoming light a given transition occurs. After repeating this procedure for several values of magnetic field, the plot of the transition energy $\Delta E = E_m - E_n$ versus the magnetic field can be plotted in order to give the B-dependence of the levels (See Fig. 14).

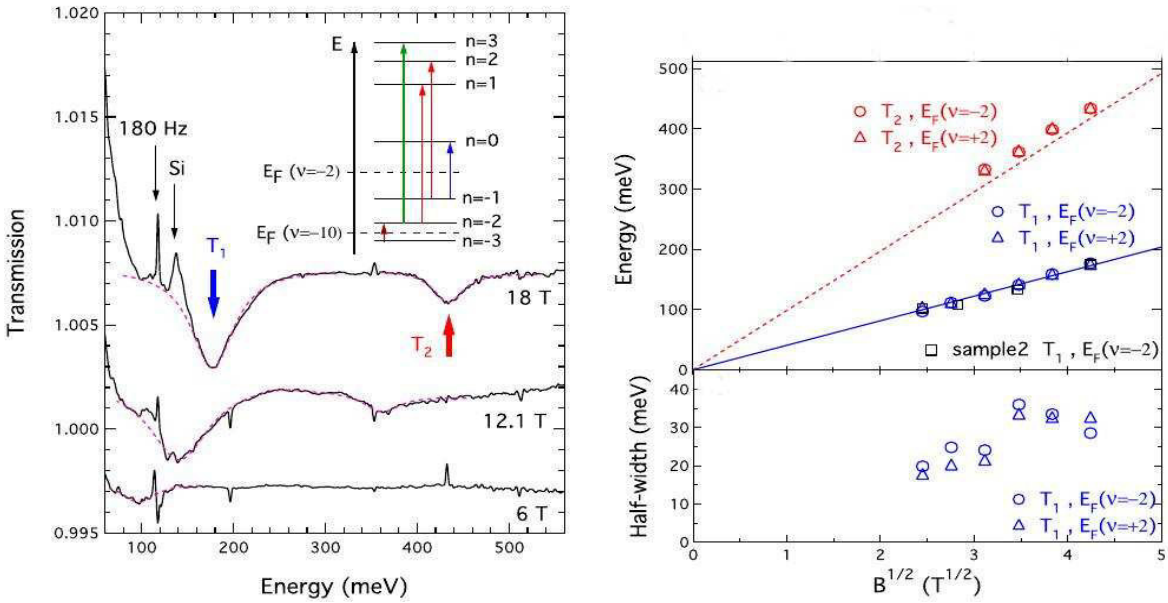

(a) (b)

Figure 14: (a) Infrared absorption spectra of holes in graphene at three different magnetic fields. The two LL resonances are denoted by $T1$ and $T2$. The inset shows a schematic LL ladder with allowed transitions indicated by arrows. (b) Resonance energies versus $\sqrt{B}$ [50].

3 Graphene and graphene ribbons under simple shear strain

The fact that graphene is a zero gap material, together with its linear energy spectrum, leads to the absence of confinement by electric potentials. In order for gating to be used as an effective way to manipulate the conductance, one needs a way to control the energy gap. In particular, it was shown that in bilayer graphene it is possible to create a gap at the K-point by using chemical doping or by the application of an electric field perpendicular to the bilayer, i.e., by applying a gate potential[54, 53, 55, 56]. A similar approach does not work for a single graphene layer. The electronic properties of these graphene layers or ribbons depend strongly on its geometry or size[57, 58, 59, 60, 61, 62, 63, 64, 65, 66]. Attempts to tune the electronics properties of these ribbons are focused on the study of chemical edge modification[58], application of uniaxial strain[61], and boron-doped graphene ribbons[67], where a substitutional boron atom is introduced at some specific sites of the graphene lattice. The introduction of a line of impurities can also open a gap in a graphene ribbon[68].

3.1 Model

In the present chapter we show how simple shear strain can tune the electronic properties of graphene and also graphene ribbons. We found that a specific simple shear strain applied to the system is able to induce a variety of different energy spectra depending on the strength of the lattice displacement and the ribbon geometry. Simple shear is an isochoric plane deformation where the elementary unit cell is deformed in one direction and constant in another. It can be defined by the shear mapping

$$\begin{bmatrix} x_i' \\ y_i' \end{bmatrix} = \begin{bmatrix} 1 & f(\delta/a) \\ 0 & 1 \end{bmatrix} \begin{bmatrix} x_i \\ y_i \end{bmatrix}, \tag{3.1}$$

where x_i and y_i are the coordinates of the i-th atom line. The determinant of the matrix transformation is equal to one, then the volume of the system is preserved. This simple shear does not generate any effective magnetic field since the stress tensor depends only on y pointing in the x-direction, i.e., $\mathbf{u} = g(y)\hat{x}$.

The system is defined as a honeycomb lattice of carbon atoms with two sublattices A and B under a simple shear strain. The graphene sheet is infinite in the x direction and has N carbon lines in the y direction. The simple shear is a plane deformation (isochoric) in which there are a set of line elements with a given reference orientation that do not change length and orientation during the deformation. Here, the simple shear is introduced in the x-direction where the new distances between atoms for the armchair and zigzag configurations are shown in Fig.15. The atoms at the top are shifted from their regular site to the right by the displacement parameter δ, the middle atoms are unchanged, while the atoms at the bottom are displaced by δ to the left. For the ribbon case, the distances are given by

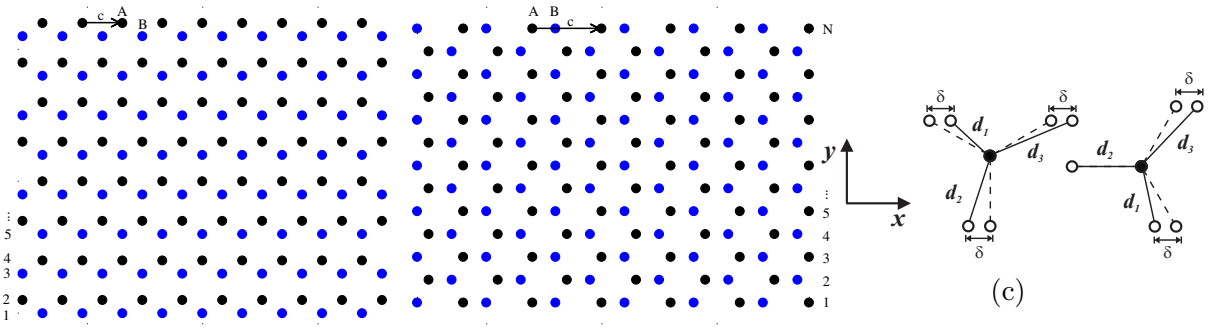

Figure 15: The lattice of ribbons with zigzag (a) and armchair (b) edges along the x-direaction. The numbers on the sides show how we number the atomic lines. (c) The distortion of zigzag (left) and armchair (right) graphene. Delta (δ) is the displacement in the x-direction. The full circles indicate sublattice A and the open circles are the sites of sublattice B

$$d_i = \sqrt{a^2 + \delta^2 + \Delta_i \delta}, \tag{3.2}$$

where $i = 1, 2, 3$, a is the lattice parameter, and Δ_i depends on the ribbon configuration and is given in Table I.

The microscopic model is based on the tight-binding Hamiltonian

$$H = -\sum_{i,j} t_{ij} a_i^\dagger b_j + h.c., \tag{3.3}$$

where for simplicity, we have taken the hopping term the same at the ribbon edges,

but it depends on the distance between the electrons in sublattice A interacting with its neighbors in sublattice B and vice-versa. It is defined as $t_{ij} = t_m = te^{-3.37(d_m/a-1)}$[69], with $m = 1, 2, 3$. The operator $a_i^\dagger(a_i)$ creates (annihilates) an electron on site i in sublattice A and the operators $b_i^\dagger(b_i)$ act on the sublattice B.

For a graphene sheet, the system is periodic in both x and y-direction allowing us to use a Fourier transformation like

$$c_i = \frac{1}{\sqrt{N}} \sum_{q_x,q_y,n,m} c_{q_x,q_y,n,m}, \tag{3.4}$$

with

$$c_{q_x,q_y,n,m} = c_0 e^{iq_x l_x n} e^{iq_y l_y m}, \tag{3.5}$$

where c stands for both operators a and b, n and m labels the lines and columns of the atoms in the graphene sheet. After straightforward algebra we obtain the equations below

$$\begin{aligned} \omega(q_x, q_y, \delta) a_{q_x,q_y,n,m} = {} & t_2 b_{q_x,q_y,n,m-1} + \\ & t_1 b_{q_x,q_y,n+1,m+1} + \\ & t_3 b_{q_x,q_y,n-1,m+1} \end{aligned} \tag{3.6}$$

$$\begin{aligned} \omega(q_x, q_y, \delta) b_{q_x,q_y,n,m-1} = {} & t_2 a_{q_x,q_y,n,m} + \\ & t_1 a_{q_x,q_y,n-1,m-2} + \\ & t_3 a_{q_x,q_y,n+1,m-2}, \end{aligned} \tag{3.7}$$

from which we arrive at the dispersion relation for the non distorted graphene sheet

$$\begin{aligned} \left(\frac{\omega(\mathbf{q})}{t}\right)^2 = {} & 1 + 4\cos\left(\frac{\sqrt{3}}{2} q_x a\right) \cos\left(\frac{1}{2} q_y a\right) \\ & + 4\cos^2\left(\frac{\sqrt{3}}{2} q_x a\right). \end{aligned} \tag{3.8}$$

Next we apply shear in the x-direction. This results in two different dispersion relations depending on the choice of the configuration (see Fig. 15). For the armchair we have the

following dispersion relation

$$\begin{aligned}\omega(\mathbf{q},\delta)^2 = t_1^2 + t_2^2 + t_3^2 + \\ 2t_1t_2\cos\left(\frac{\sqrt{3}}{2}q_y a - \frac{3}{2}q_x a + \delta q_x\right) \\ + 2t_2t_3\cos\left(\frac{\sqrt{3}}{2}q_y a + \frac{3}{2}q_x a + \delta q_x\right) \\ + 2t_1t_3\cos\left(\sqrt{3}q_y a + 2\delta q_x\right),\end{aligned} \tag{3.9}$$

and for the zigzag configuration we have

$$\begin{aligned}\omega(\mathbf{q},\delta)^2 = t_1^2 + t_2^2 + t_3^2 + \\ 2t_1t_2\cos\left(2\delta q_x - \frac{\sqrt{3}}{2}q_x a - \frac{3}{2}q_y a\right) \\ + 2t_2t_3\cos\left(2\delta q_x + \frac{\sqrt{3}}{2}q_x a - \frac{3}{2}q_y a\right) \\ + 2t_1t_3\cos\left(\sqrt{3}q_x a\right).\end{aligned} \tag{3.10}$$

When considering a ribbon the periodicity is only in the x-direction, and the operators depend on the one-dimensional ($1D$) wave vector $\mathbf{q} = q_x$ parallel to the ribbon edge. The hamiltonian is now written in the wavevector/energy space through its Fourier transform.

$$H = -\sum_{\mathbf{q}nn'} \tau_{nn'}(\mathbf{q},\delta) a^\dagger_{\mathbf{q}n} b_{\mathbf{q}n'} + h.c. \tag{3.11}$$

The structure factor $\tau_{nn'}(\mathbf{q},\delta)$ carries the dependence on the wavevector q_x and includes the effect of shear δ. In order to find the band structure of the system we apply the standard equation of motion $i\hbar da/dt = [a, H]$ to the operators $a^\dagger_n$ and a_n in line n. Taking $\hbar = 1$ and assuming that the modes behave like $exp[-i\omega(q_x)t]$ we arrive at the set of coupled equations

$$\omega(q_x,\delta) a_{q_x,n} = \sum_{n'} \tau_{n,n'}(q_x,\delta) b_{q_x,n'}, \tag{3.12}$$

$$\omega(q_x),\delta) b_{q_x,n} = \sum_{n'} \tau^*_{n',n}(q_x,\delta) a_{q_x,n'}. \tag{3.13}$$

The matrix elements $\tau_{n,n'}(q_x,\delta)$ are given by

Table 1: Value of the matrix elements in the hopping matrix

Parameter	Zig-zag	Armchair
Δ_1	$-a\sqrt{3}$	$-a$
Δ_2	0	$-\delta$
Δ_3	$a\sqrt{3}$	a
α	0	$t_2 e^{-iq_x a}$
β	$t_2 e^{-iq_x \delta}$	$t_1 e^{iq_x(a/2-\delta)}$
γ	$t_1 e^{-iq_x(a\sqrt{3}/2-\delta)} + t_3 e^{iq_x(a\sqrt{3}/2+\delta)}$	$t_3 e^{iq_x(a/2+\delta)}$

$$\tau_{n,n'}(q_x,\delta) = \alpha\delta_{n,n'} + \beta\delta_{n',n+1} + \gamma\delta_{n',n-1} \tag{3.14}$$

for the armchair configuration and

$$\tau_{n,n'}(q_x,\delta) = \beta\delta_{n',n+1} + \gamma\delta_{n',n-1}, \tag{3.15}$$

for the zigzag ribbon. The above set of equations can be written in matrix form

$$\omega(q_x,\delta)\begin{bmatrix} a_{q_x n} \\ b_{q_x n} \end{bmatrix} = \begin{bmatrix} 0 & T(q_x,\delta) \\ T(q_x,\delta)^* & 0 \end{bmatrix}\begin{bmatrix} a_{q_x n} \\ b_{q_x n} \end{bmatrix}. \tag{3.16}$$

The energy levels are now the solutions of

$$det\begin{bmatrix} \omega(q_x,\delta)I_N & T(q_x,\delta) \\ T(q_x,\delta)^* & \omega(q_x,\delta)I_N \end{bmatrix} = 0, \tag{3.17}$$

with I_N the unit matrix and T the hopping matrix:

$$T = \begin{bmatrix} \alpha & \beta & 0 & 0 & 0 & \dots \\ \beta & \alpha & \gamma & 0 & 0 & \dots \\ 0 & \gamma & \alpha & \beta & 0 & \dots \\ 0 & 0 & \beta & \alpha & \gamma & \dots \\ \vdots & \vdots & \vdots & \vdots & \vdots & \ddots \end{bmatrix}, \tag{3.18}$$

where the parameters α, β, and γ are given in Table I.

3.2 Results

Before analyzing the results for the ribbon, it is worth investigating the effect of this simple shear on the energy band of a graphene sheet. For comparison we show in Figure 16 a contour plot of the energy band for the graphene sheet that has a zigzag configuration

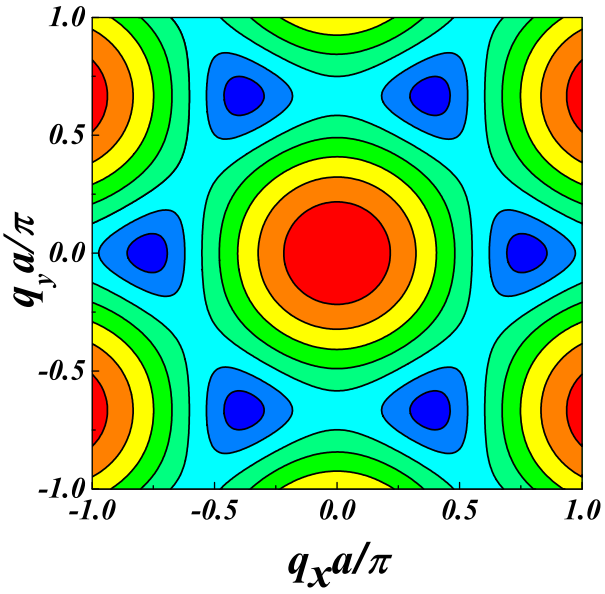

Figure 16: (Color online) The contour plot for a graphene sheet energy dispersion relation. The energy scale is from blue (zero energy) to red ($E/t = 3$)

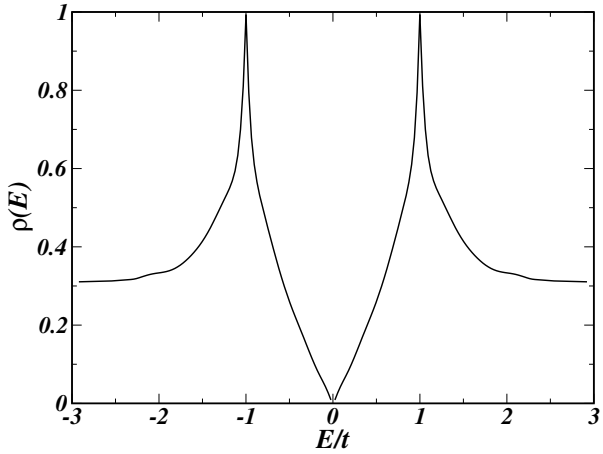

Figure 17: The density of states for a graphene sheet.

in the x-direction in the absence of any shear. There are six points where the gap between the conduction and the valence band is zero. For the armchair configuration in the x-direction the energy band is rotated by 90° from the one shown in Fig. 16. We also plot the energy histogram for the graphene sheet in Fig. 17. That gives us the density of states (DOS) per unit cell which is linear close to the Dirac points.

For a small applied shear, i.e., small distortion of the lattice ($\delta = 0.1a$), the top panels in Figure 18 show a distortion in the contour plot of the energy band for both armchair (left) and zigzag (right) configurations. The shear shifts the Dirac cones from their original position and the energy minima of the bands are getting closer in pairs. When looking to the DOS shown in Fig. 19, the top panels correspond to the the energy

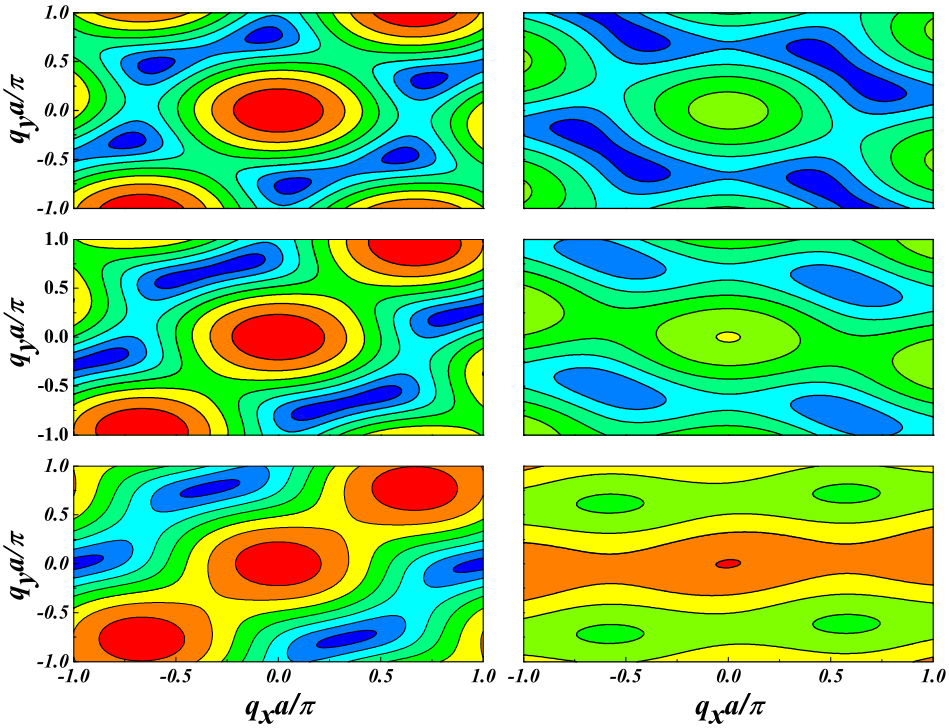

Figure 18: (Color online) Contour plot of the dispersion relation for a graphene sheet with shear applied in the x-direction. The left(right) panels are the spectrum for the armchair(zigzag) configuration. From the top to the bottom, $\delta = 0.1a, 0.25a, 0.5a$. The energy increases from blue to red, ranging from $E/t = 0$ to $E/t = 3.01(E/t = 4.5)$.

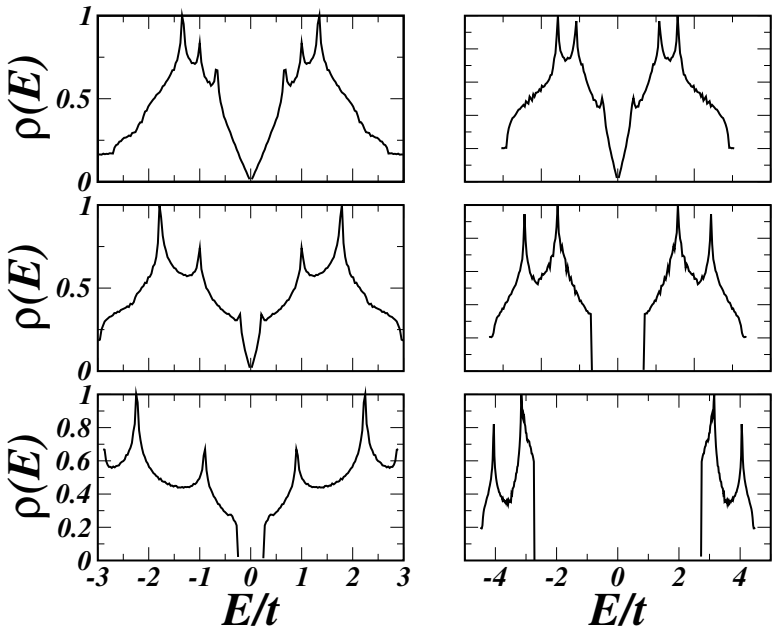

Figure 19: The density of states for a graphene sheet under shear. The left(right) panels are the spectrum for the armchair(zigzag) configuration. From the top to the bottom, $\delta = 0.1a, 0.25a, 0.5a$.

bands as in Fig. 18. The DOS has now much more structure than the one with no shear. As one increases the shear strength ($\delta = 0.25a$) we still find six minima in the energy for the armchair configuration but only four in the zigzag case. For the later case, they are no longer Dirac cones and now a gap opens in the dispersion relation. When considering the maximum distortion, $\delta = 0.5a$, instead of six minima points we have only four. The new structure created by the shear gives a complete different dispersion relation, as if we have a different material for each configuration.

From Figure 19 we notice that as δ increases the DOS has no resemblance to the one for the non stretched graphene. For the zigzag orientation the DOS shows clearly that the gap increases with δ. There are no states with energy less than $E/t \approx 1.7$. These forbidden energies increases as δ/a increases. For such a simple strain there are no indications that the dispersion relation is linear around the minimum of the conduction band.

It is interesting to see the effect of the shear intensity against q_x for a specific value of q_y. This plot is shown in Figure 20. For $q_y = 0$, the graphs show a reciprocal energy for both configurations which satisfy $E(q_x) = E(-q_x)$. As the shear increases the energy oscillates from a maximum to a minimum in both configurations, unless for $q_x = 0$. In particular for the zigzag configuration, the right panel in the figure, there is a value of δ where the number of maximum points form a continuum. The graphs are not periodic,

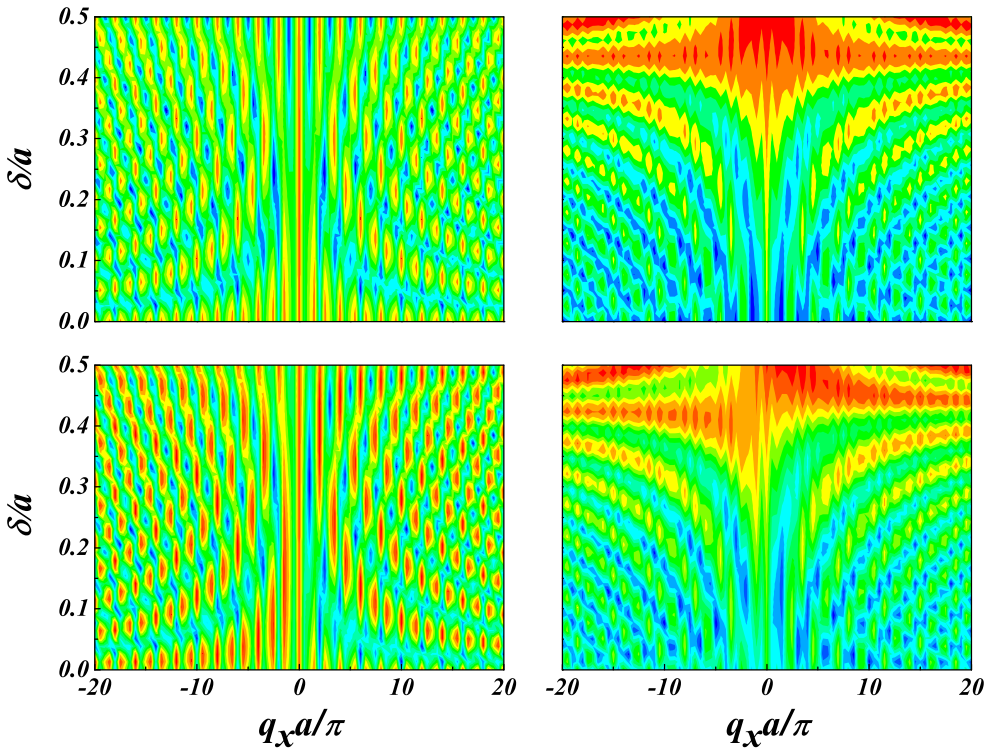

Figure 20: Contour plot of the graphene dispersion relation with shear applied in the x-direction. The left(right) panels are the spectrum for the armchair(zigzag) configuration. From the top to the bottom, $q_y = 0.0, 0.7$. The energy increases from blue to red, ranging from $E/t = 0$ to $E/t = 3.01$ in the left graphs and to $E/t = 4.5$ in the right graphs

as q_x increases new structures appear in the figures forming bands with maximum and minimum energy. For $q_y = 0.7$ the reciprocity is lost, i.e. $E(q_x) \neq E(-q_x)$. But there are still bands of maximum and minimum energy as in the $q_y = 0$ case. From the spectrum, it is clear that the shear strength tunes the size of the energy gap.

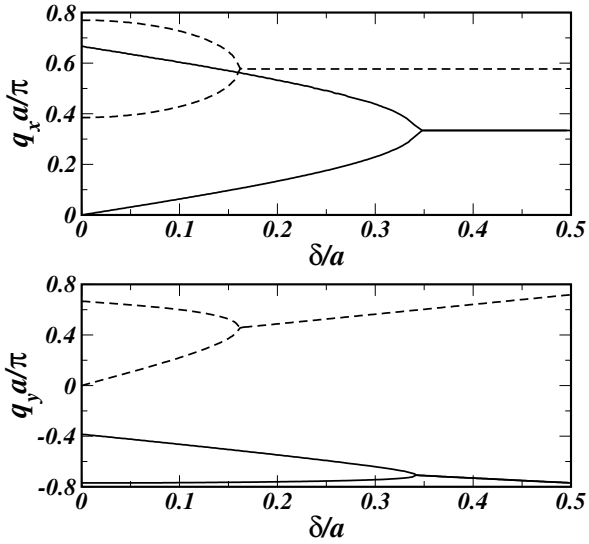

Figure 21: The location of the energy minima in the Brillouin zone against δ/a. Solid (Dashed) curves for the minima in the armchair (zigzag) configuration.

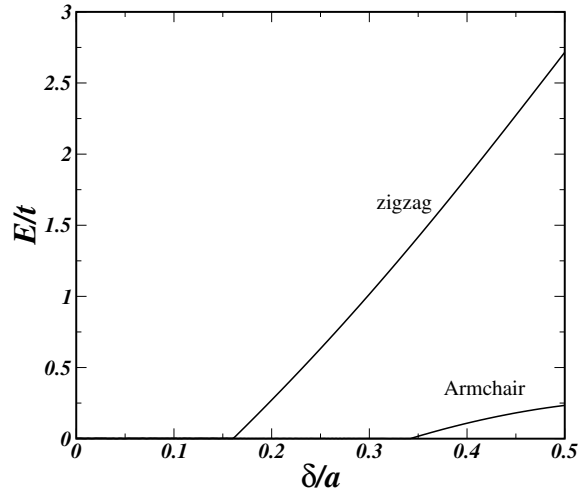

Figure 22: The value of the conduction energy minimum as a function of δ/a

We choose two minima in the top graphs of figure 20 to follow as the shear line displacement increases. In Fig. 21, we show how these two minima get close to each other for the armchair and zigzag configuration. The initial location of the minima are $q_x = 0.0, q_y = -0.78$ and $q_x = 0.68, q_y = -0.4$ for the armchair and $q_x = 0.4, q_y = -0.65$ $q_x = 0.8, q_y = 0.0$ for the zigzag. In the armchair case the two minima joint at the value of $\delta/a \approx 0.34$ and $\delta/a \approx 0.16$ for the zigzag case. In both cases these are the

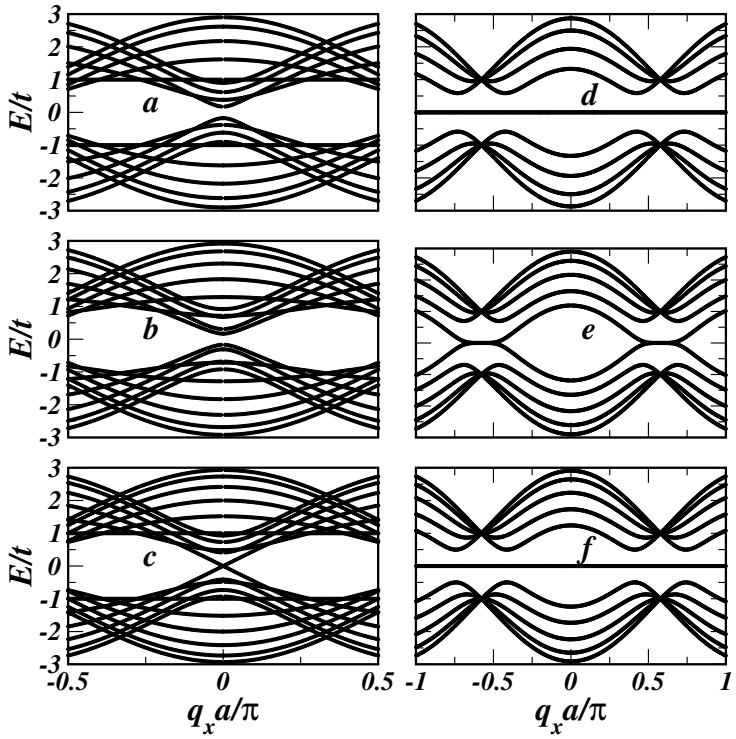

Figure 23: Dispersion relation for graphene ribbons for armchair $(a) - (c)$ and zigzag $(d) - (f)$ edges with $N = 9$, 10, and 11 atomic lines.

values where the gap in the energy band starts as can be seen in Fig. 22. The figure shows that the lowest energy value starts to grow quadratically. For the armchair case we are able to fit the curve with $E/t = -1.1666 + 4.7338\delta/a - 3.8655(\delta/a)^2$ and $E/t = -1.0077 + 5.68\delta/a + 3.5658(\delta/a)^2$ for the zigzag

In order to study the effect of this shear in ribbons Fig. 23 shows, for the armchair and zigzag configuration, the dispersion relation for ribbons with 9, 10, and 11 atomic lines. Depending on the number of lines, the ribbon can present three (two) kinds of energy bands for the armchair[64] (zigzag) configuration where the main difference is related to the type of ribbon edge.

It is worth mention here that the way we define the number of atoms lines is different for example than in Ref. [57], there N is the number of dimer lines or zigzag lines, that is a group of two lines, one with A atoms and another with B atoms, what means that when the N is odd they have an even number of lines of atoms. Here we define N as the number of single atoms lines (see Fig. 15), then when we say that our ribbon has $N = 9$ means that both edges have the same type of atoms (A or B), this make the ribbon zigzag in the bottom edge, for instance, but creates a flat top edge that is responsible for a dispersionless $E = 0$ mode.

As we start distorting the zigzag ribbon with 10 atomic lines the spectrum starts to change in such a way that the crossing modes disappear completely and the zero energy gap around $q_x = \pm 1/\sqrt{3}$ is becoming more localized. Increasing δ even further there is a pronounced gap in the electronic structure and the modes behave like sinusoidal waves, see Fig. 24. For $N = 11$, the effect of the distortion is to remove any crossover between the modes in the dispersion relation. As δ increases all the modes but the zero one gets more and more energetic in modulus, this is shown in Fig. 25.

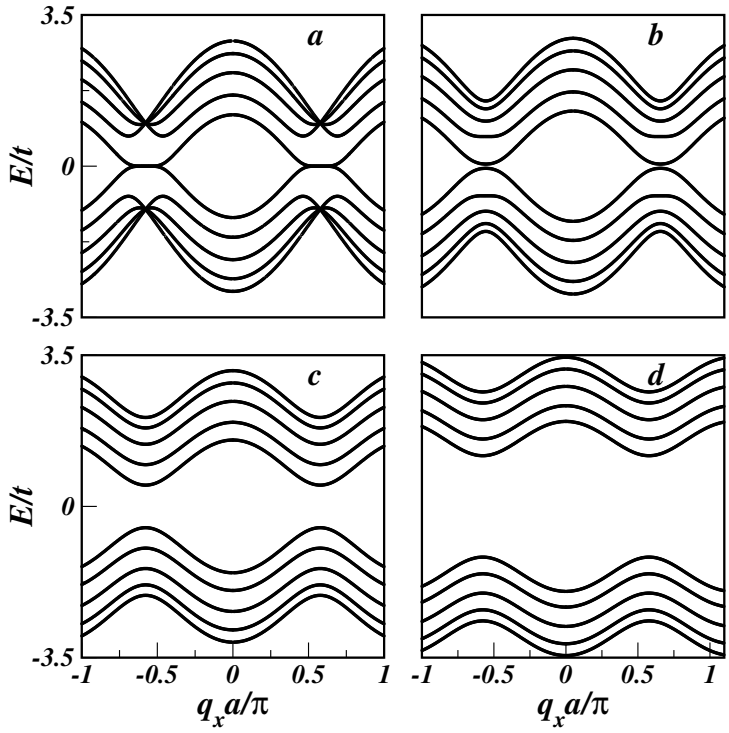

Figure 24: Dispersion relation for zigzag graphene ribbons with 10 atomic lines, with shear (a) $\delta = 0$, (b) $\delta = 0.1a$, (c) $\delta = 0.2a$ and (d) $\delta = 0.3a$.

Next, we analyze the effect of shear on an armchair ribbon. For this geometry the ribbon is metallic when we have $3i - 1$ atomic lines, where $i = 1, 2, 3, \ldots$, and semiconductor otherwise. Each of these arrangements results in a different energy band. Figs. 23(a)-(c) show the usual behavior of dispersion relation for a normal armchair ribbon, i.e, the top of the valence band and the bottom of the conduction band are located at $q_x = 0$. Applying shear to the ribbon with 10 lines, Fig. 26 shows the lower energy modes that starts to get detached from the others lowering its energy. As δ increases the gap vanishes and the system becomes metallic. When applying the same shear to the ribbon with 11 lines, the shear decreases the energy of the lower mode, and the zero gap is extended beyond a single value of q_x.

From the results shown here it is clear that shear affects the dispersion relationship for

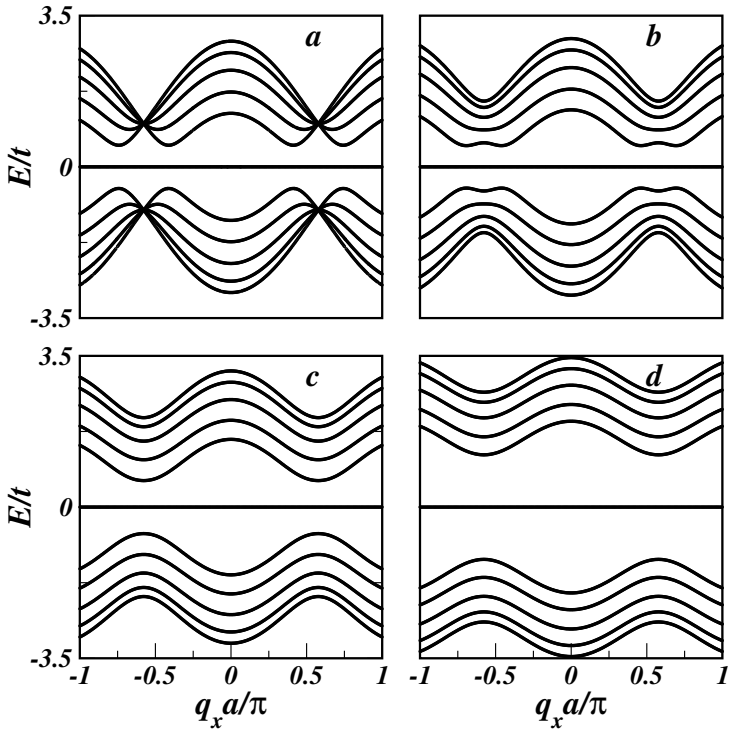

Figure 25: The same as in Fig. 24, but now for $N = 11$.

the ribbons in a very unusual way. That can be seen explicitly in Figs. 28 and 29 where the behavior of the energy levels for zigzag and armchair ribbons are shown as function of δ/a . For a zigzag ribbon with ten atomic lines, we choose to study the specific value of the wave vector $q_x a/\pi = 1/\sqrt{3}$ where there is no energy gap between the conduction and valence bands. For this value of the wave vector there is one level with zero energy and four others are degenerate at $E/t = 1$ when no stress is applied. As the net is distorted a gap starts to appear, and the other levels spread. As the stress is increased the modes start to grow almost linearly. When we do the same analysis for the armchair configuration, a gap is closed for $N = 10$ and $N = 9$, and there is a very small opening of energy gap for $\delta/a \approx 0.25$ (see inset of Fig. 29).

In summary, we have shown here that a simple tight-binding model is able to extract very interesting features of graphene and graphene ribbon when a simple shear is applied to the system. This simple shear does not generate an effective magnetic field, and the main feature is the fact that controlling the net displacement one can modify the gap in the energy spectrum of graphene and graphene ribbons. This is expected to be a very effective mechanism for tuning the electronic properties of these systems.

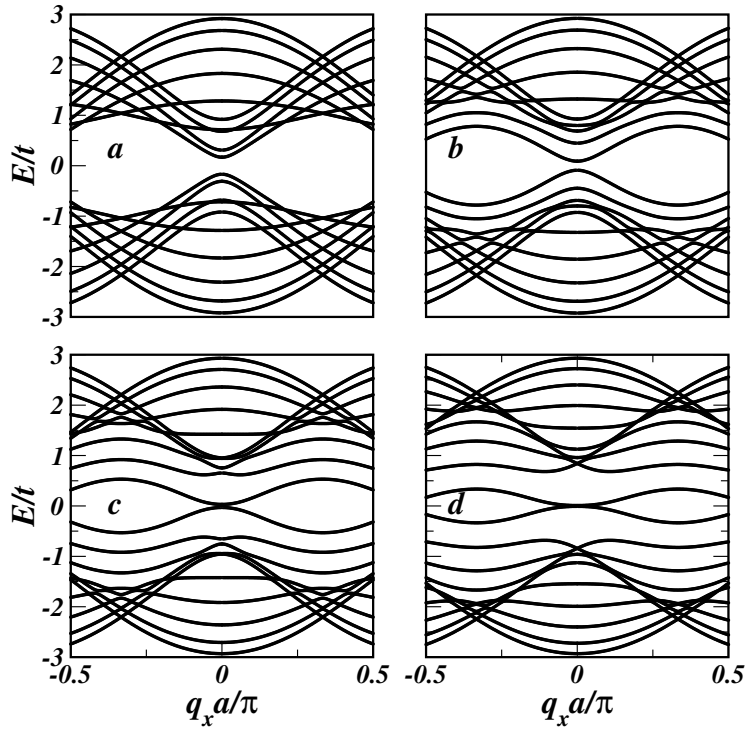

Figure 26: Dispersion relation for an armchair ribbon with ten lines or carbon atoms, with shear (a) $\delta = 0$, (b) $\delta = 0.1a$, (c) $\delta = 0.2a$ and (d) $\delta = 0.3a$.

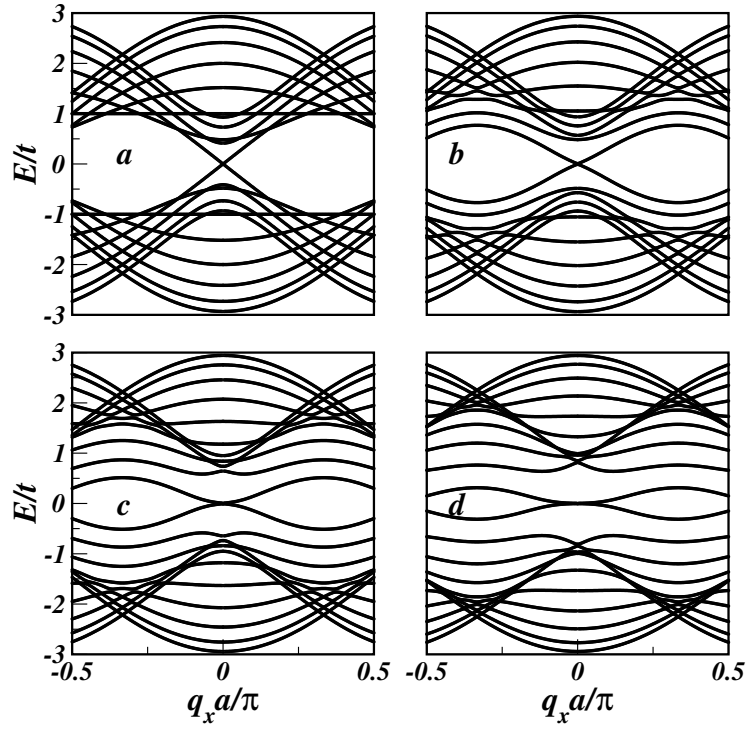

Figure 27: The same as in Fig. 26, but now for $N = 11$.

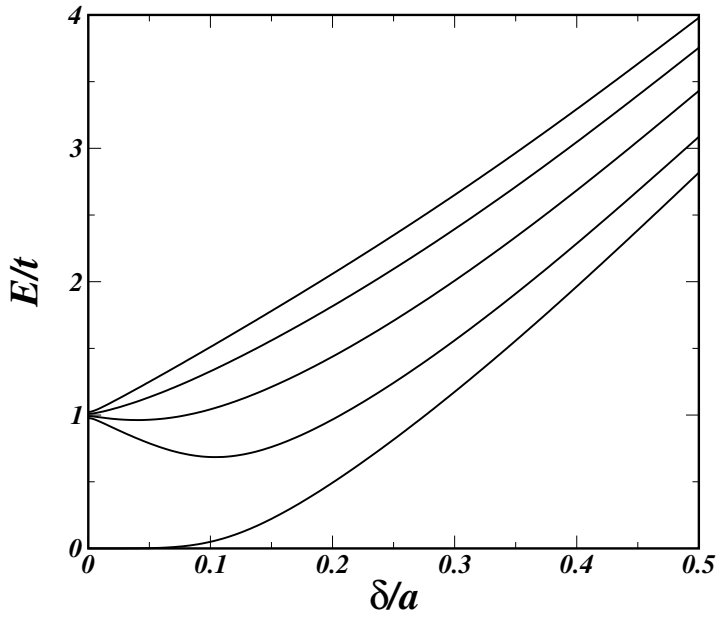

Figure 28: The energy at $q_x = 1/\sqrt{3}$ for a graphene sheet with 10 atomic lines and zigzag edges as function of the strength of the stress.

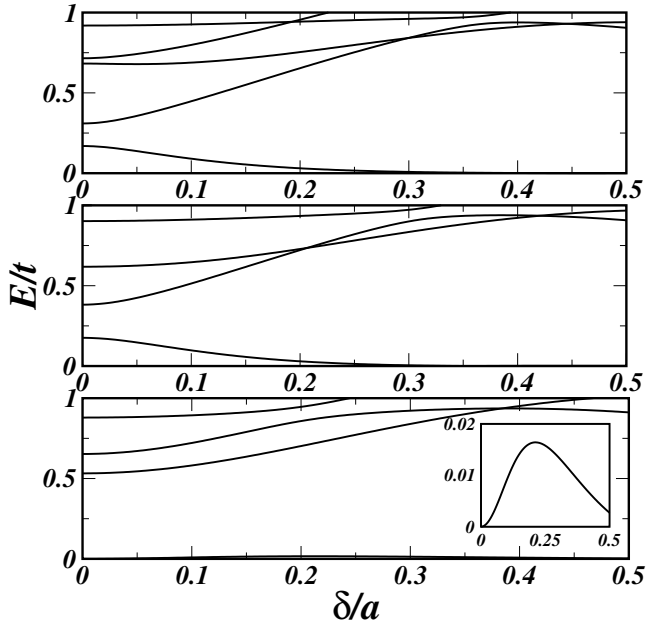

Figure 29: The energy behavior of a graphene sheet in the armchair configuration for $q_x = 0$. The number of atomic lines increases from 9 to 11 from the top to the bottom. The inset in the bottom panel displays the first mode around $E/t = 0$, showing the oppening of a small gap for values of δ/a around 0.25

4 Graphene stacks

The advances in the experimental fabrication of high quality graphene samples and the study of their many unusual properties raised a great curiosity about thin films of graphite. How does the spectrum change when two or three graphene layers are stacked? And still, how many layers do one need to stack in order for the properties of the bulk graphite start to appear? Many works have been done trying to answer these questions [70, 71, 72, 73], and along the rest of this chapter we will discuss some of the properties of bilayers and trilayers of graphene.

4.1 Bilayer graphene

The bilayer graphene (BLG) consists of two stacked single layers separated by a distance of $\approx$ 3.35 Å. The layers are positioned in such way that the B_2 atoms from the top layer are exactly on the top of the A_1 atoms from the bottom layer, while the A_2 atoms lie on the middle of the hexagons from the bottom layer. Figure 15 shows how the top view of this structure should look like.

The tight-binding model for graphite can be adapted for every finite number of stacked layers, with the simplest case being the BLG [77]. The Hamiltonian describing the bilayer system is given in Eq. (4.1). The first line of Eq. (4.1) is the Hamiltonian of two independent single layers, where $\mathbf{a}^{\dagger}_{i,m}$ ($\mathbf{a}_{i,m}$) creates (annihilates) electrons on the i sites of sublattice A of layer m, whereas $\mathbf{b}^{\dagger}_{j,m}$ ($\mathbf{b}_{j,m}$) act likewise on the j sites of sublattice B. The terms containing γ_1 represent the direct coupling between the dimer sites A_1 and B_2, the γ_3 terms describe the hopping between non-dimer sites B_1 and A_2, and the γ_4 terms

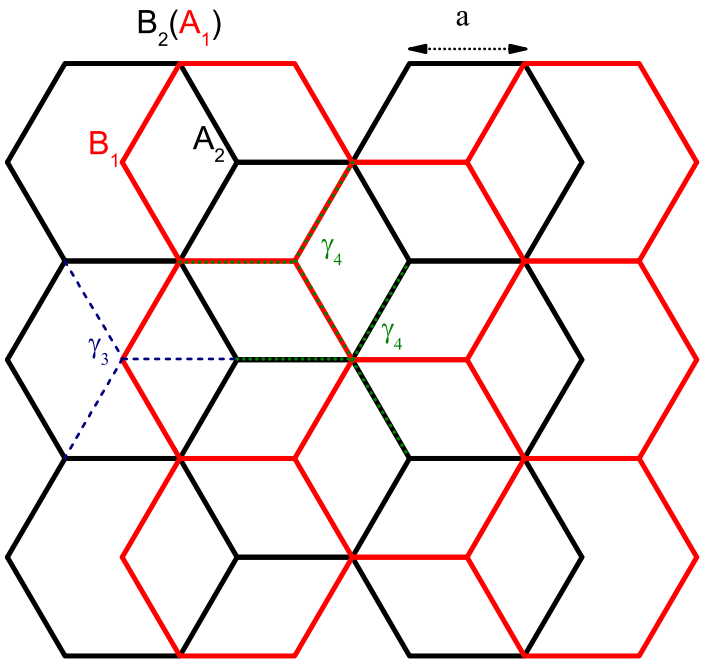

Figure 30: Top view of the crystalline structure of bilayer graphene. The bottom (red) and top (black) layers are connected by the hopping parameters γ_1 (coupling the dimer sites A_1 and B_2), γ_3 (coupling non-dimer sites B_1 and A_2), and γ_4 (coupling dimer and non-dimer sites A_1 and A_2 or B_1 and B_2).

couples the dimer sites A_1 and B_2 with the non-dimer sites A_2 and B_1, respectively.

$$\begin{aligned}\mathbf{H} = &-\gamma_0 \sum_{i,j}\sum_{m=1}^{2}(\mathbf{a}_{i,m}^{\dagger}\mathbf{b}_{j,m} + \mathbf{b}_{j,m}^{\dagger}\mathbf{a}_{i,m}) \\ &-\gamma_1 \sum_{i,j}(\mathbf{a}_{i,1}^{\dagger}\mathbf{b}_{j,2} + \mathbf{b}_{j,2}^{\dagger}\mathbf{a}_{i,1}) \\ &-\gamma_3 \sum_{i,j}(\mathbf{a}_{i,2}^{\dagger}\mathbf{b}_{j,1} + \mathbf{b}_{j,1}^{\dagger}\mathbf{a}_{i,2}) \\ &-\gamma_4 \sum_{i,j}(\mathbf{a}_{i,1}^{\dagger}\mathbf{a}_{j,2} + \mathbf{a}_{j,2}^{\dagger}\mathbf{a}_{i,1} + \mathbf{b}_{i,1}^{\dagger}\mathbf{b}_{j,2} + \mathbf{b}_{j,2}^{\dagger}\mathbf{b}_{i,1}) \\ &+\sum_{i,j}\sum_{m=1}^{2}(E_{A_m}\mathbf{a}_{i,m}^{\dagger}\mathbf{a}_{i,m} + E_{B_m}\mathbf{b}_{j,m}^{\dagger}\mathbf{b}_{j,m}). \end{aligned} \tag{4.1}$$

The last term of the Hamiltonian represent the on-site energy of the sublattices A and B in both layers. Differently from the single layer graphene, we can divide the atoms in two subgroups with different distributions of neighbors atoms around them: dimer and non-dimer atoms. The dimer atoms are those which are connected by γ_1 parameter. The

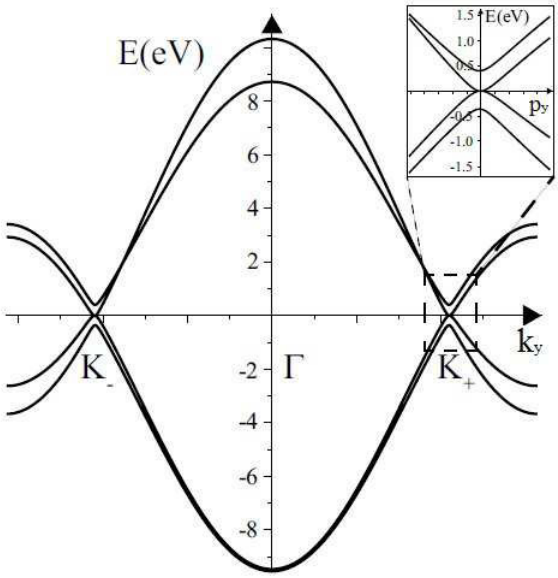

Figure 31: Energy bands of bilayer graphene plotted along the k_y direction. The inset shows the behavior of the energies in the vicinity of the Dirac point [76].

on-site energies are described by:

$$E_{A_1} = U_1 + \Delta, \tag{4.2}$$

$$E_{B_1} = U_1, \tag{4.3}$$

$$E_{B_2} = U_2 + \Delta, \tag{4.4}$$

$$E_{A_2} = U_2, \tag{4.5}$$

where U_1 and U_2 describe interlayer asymmetry, and Δ is the energy difference between dimer and non-dimer sites. Table 2 shows the experimental values of the tight-binding parameters for graphite, bilayer and trilayer graphene. The values with * were not experimentally determined by the cited experiment.

If we go through the same steps as before for single layer graphene, we obtain

$$\mathbf{H}_k = \begin{pmatrix} E_{A_1} & -\gamma_0 g(\vec{k}) & -\gamma_1 & -\gamma_4 g^*(\vec{k}) \\ -\gamma_0 g^*(\vec{k}) & E_{B_1} & -\gamma_4 g^*(\vec{k}) & -\gamma_3 g(\vec{k}) \\ -\gamma_1 & -\gamma_4 g(\vec{k}) & E_{B_2} & -\gamma_0 g^*(\vec{k}) \\ -\gamma_4 g(\vec{k}) & -\gamma_3 g^*(\vec{k}) & -\gamma_0 g(\vec{k}) & E_{A_2} \end{pmatrix}. \tag{4.6}$$

The eigenenergies of the above Hamiltonian are plotted in Fig. 31 along the k_y direction. In order to obtain the Hamiltonian around the K point, let us substitute the first-order

expansion of $g(\vec{k})$ given in Eq. (2.18) into Eq. (4.6) and find

$$\mathbf{H}_K = \begin{pmatrix} U_1 + \Delta & v\pi^\dagger & \gamma_1 & v_4\pi \\ v\pi & U_1 & v_4\pi & v_3\pi^\dagger \\ \gamma_1 & v_4\pi^\dagger & U_2 + \Delta & v\pi \\ v_4\pi^\dagger & v_3\pi & v\pi^\dagger & U_2 \end{pmatrix}, \tag{4.7}$$

where $v = \frac{3a\gamma_0}{2\hbar}$, $v_3 = \frac{3a\gamma_3}{2\hbar}$, $v_4 = \frac{3a\gamma_4}{2\hbar}$, $\pi = p_x + ip_y$, $\pi^\dagger = p_x - ip_y$, and the corresponding eigenfunction is $\Psi_K = (\psi_{A_1}, \psi_{B_1}, \psi_{B_2}, \psi_{A_2})^T$. This full Hamiltonian can not be analytically diagonalized, nevertheless Fig. 32(a) shows the contour plot of the first conductance band obtained by numerical diagonalization of the full Hamiltonian in Eq. (4.7). The energy values range from 0 (blue) to 10 meV (red). On the right panel of Fig. 32, the conductance band is plotted taking into account just the parameter γ_1. We can see from this result that the inclusion of γ_3 and γ_4 breaks the cylindrical symmetry of the bands, leading to distortion of the bands at low energies called trigonal warping. Actually a more detailed study reveals that the γ_3 terms are responsible for this effect, whereas the γ_4 and Δ terms introduce an electron-hole asymmetry [77, 76].

By ignoring the γ_4 terms and the on-site energies, analytical solutions of the bilayer bands can be found as [77]:

$$E_\alpha^2 = \frac{\gamma_1^2}{2} + \left(v^2 + \frac{v_3^2}{2}\right)p^2 + (-1)^\alpha \left[\frac{\left(\gamma_1^2 - v_3^2p^2\right)^2}{4} + v^2p^2\left(\gamma_1^2 + v_3^2p^2\right) - 2\gamma_1 v_3 v^2 p^3 \cos(3\phi)\right]^{1/2}, \tag{4.8}$$

where $\alpha = 1(2)$ for the lower (upper) bands and $\phi = \arctan(p_y/p_x)$. Notice that for a given momentum p, the maximum energies are found for $\phi = 0, 2\pi/3, 4\pi/3$ as can be seen in Fig. 32(a). When one makes $\gamma_3 = 0$ we recover cylindrically symmetric bands

$$E_\alpha^2 = \frac{\gamma_1^2}{2}\left[1 + (-1)^\alpha \sqrt{\frac{4v^2p^2}{\gamma_1^2} + 1}\right] + v^2p^2. \tag{4.9}$$

Although the trigonal warping is an important effect at very low energies, as the energy exceeds few meV ($\approx$ 10 meV) this distortion on the bands are negligible. Since the current experimental techniques do not have access to this range of energy, from now on we are going to ignore γ_3 and γ_4 terms and work with the minimal coupling γ_1 term.

As single layer graphene, BLG has also shown very unique properties. Presenting a parabolic gapless spectrum at low energies, BLG can be easily converted into a semicon-

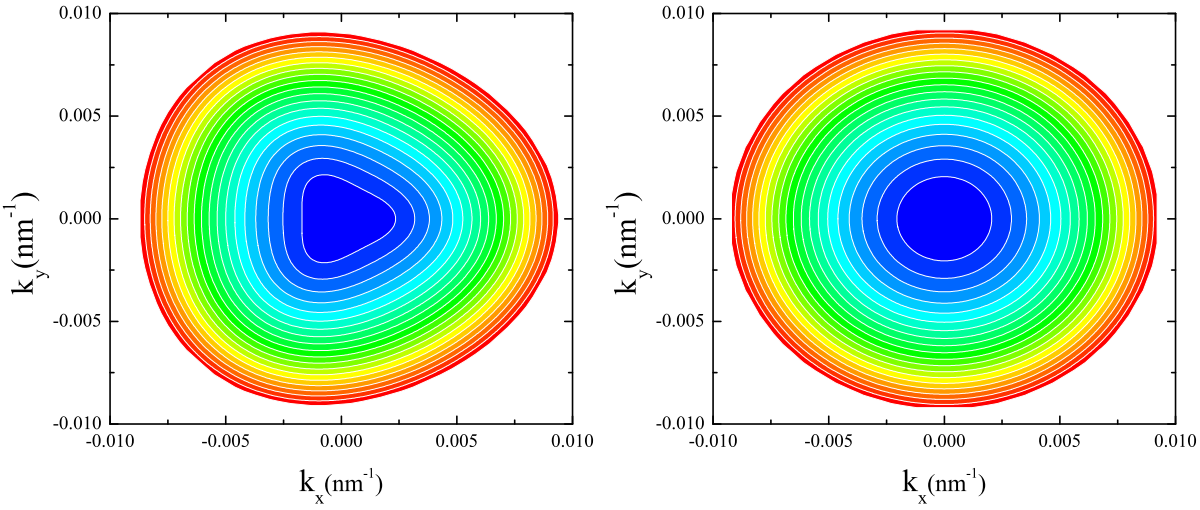

(a) (b)

Figure 32: (a) Contour plot of the first conductance band of bilayer graphene for the full-parameters model. (b) The same plot as in (a) for $\gamma_3 = \gamma_4 = \Delta = 0$. The energy values range from 0 (blue) to 10 meV (red).

ductor with tunable gap by applying an external electric field that breaks the two layers inversion symmetry [54, 55, 56]. Figure 33 shows the spectrum of neutral (black solid lines) and biased (green dashed lines) BLG. The band gap in the K point is given by $U = |U_1 - U_2|$, while the actual band gap E_g occurs at momentum k_g

$$k_g = \frac{U}{2\hbar v}\sqrt{\frac{2\gamma_1^2 + U^2}{\gamma_1^2 + U^2}}, \quad E_g = \frac{U\gamma_1}{\sqrt{\gamma_1^2 + U^2}}. \tag{4.10}$$

Figure 33 shows the energy bands of BLG for three different values of U: $U = 0$ (solid black lines), $U = 0.1$ eV (dashed green lines) and $U = 0.2$ eV (dotted orange lines). The inset shows the formation of the Mexican hat shaped band gap as U in increased.

In the presence of a magnetic field the BLG spectrum splits into LLs presenting a rather intricate dependence on Landau index and magnetic field B. *Pereira et al.* found that, in the absence of bias, the explicit form of the LLs are given by [78]:

$$\epsilon_n = \pm\frac{\gamma_1'}{\sqrt{2}}\left[1 + \frac{2}{\gamma_1'^2}(2n+1) \pm \sqrt{\left[1 + \frac{2}{\gamma_1'^2}(2n+1)\right]^2 - \frac{16}{\gamma_1'^4}n(n+1)}\right]^{1/2}, \tag{4.11}$$

where $\epsilon_n = \frac{E_n \ell_B}{\hbar v}$ and $\gamma_1' = \frac{\gamma_1 \ell_B}{\hbar v}$. When $n/\gamma_1' \ll 1$ the above expression can be simplified to

$$\epsilon_n = \pm\frac{2}{\gamma_1'}\sqrt{n(n+1)}, \tag{4.12}$$

Parameter	Graphite [74]	Bilayer [75]	Trilayer [89]
γ_0	3.16(5) eV	3.16(3) eV	3.1*[1]
γ_1	0.39(1) eV	0.381(3) eV	0.39*
γ_2	-0.020(2) eV	–	-0.028(4)
γ_3	0.315(15) eV	0.38(6) eV	0.315* eV
γ_4	0.044(24) eV	0.14(3) eV	0.041(10) eV
γ_5	0.038(5) eV	–	0.05(2) eV
Δ	-0.008(2)eV	0.022(3) eV	-0.03(2) eV

Table 2: Values of the Tight-binding parameters experimentally determined for graphite, bilayer and trilayer graphene.

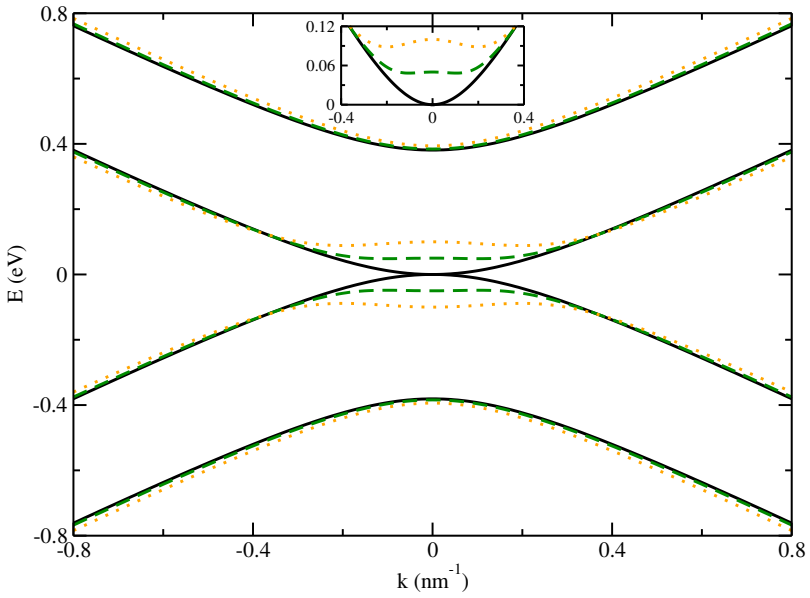

Figure 33: Energy bands of BLG for $U = 0$ (solid black lines), $U = 0.1$ eV (dashed green lines) and $U = 0.2$ eV (dotted orange lines). The inset shows an enlargement of the low-energy conductance bands.

assuming a linear B-dependence for small energies. Then, these LLs move from a linear in B spectrum, characteristic of an ordinary 2D electron gas, to a $\sqrt{B}$ dependence as the energy increases [79], creating another type of IQHE [80]. Left panel of Fig. 34 shows the behavior of the LLs in BLG, while the right panel shows a schematic illustration of the QHE in BLG. Alike the standard QHE, the plateaus in Hall conductivity σ_{xy} occur at integer values of e^2/h. Nonetheless, like in single layer graphene, the zero plateau is still missing as a consequence of the LL $E = 0$.

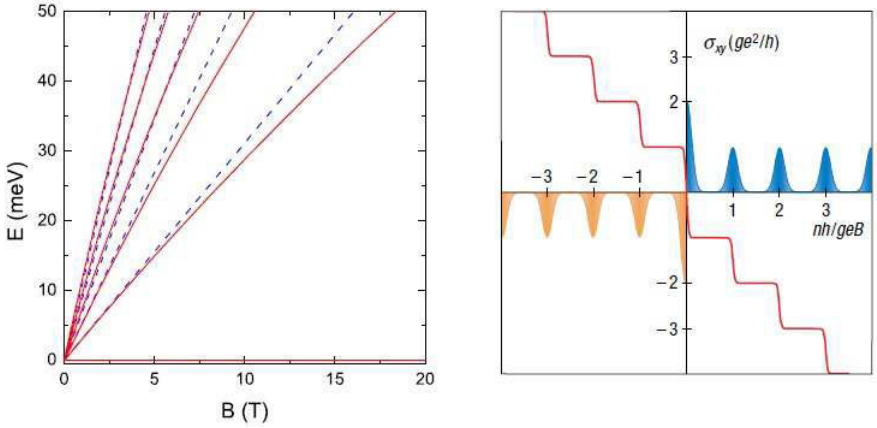

Figure 34: (Left panel) Landau levels ($n = 0, \cdots, 5$) in an unbiased BLG as a function of the magnetic field. The red solid lines result from Eq. 4.11 and the blue dashed ones are the approximate results from Eq. 4.12 [78]. (Right panel) Schematic illustration of the QHE in BLG [80].

4.2 Trilayer graphene

When three or more layers of graphene are stacked, the way these layers lie on top of each other can be considerably determining on the electronic properties of the thin film. Among the multilayer graphene films, trilayer graphene (TLG) has received a lot of attention recently. The two more relevant stacking orders are the rhombohedral, or ABC stacking, and the Bernal, or ABA stacking. In each case, the relative positions of the lowermost layer (C in one case and A in the other) helps dictate the possible symmetries of the subsequent wavefunctions associated with each layer [81, 82, 83]. The ABA stacking is the most common one and a great part of the natural graphite has this crystalline structure. In that case, the second layer is shifted in relation to the first one, just as in bilayer, whereas the third layer lies exactly on the top of the first one. Although the ABC stacking is less common, it has recently been reported that 16% of the synthesized graphite [73] and around 15% of exfoliated TLG [85] has rhombohedral (ABC) stacking. In ABC stacking, differently from ABA case, the third layer is shifted in relation to both previous layers. Figure 35 illustrates both types of stacking orders.

In a similar way as in BLG, a tight-binding model can be applied to TLG and, if we follow the same procedure, considering just the minimal coupling between adjacent layers, we arrive in following Hamiltoninans for ABA and ABC TLG around the K point:

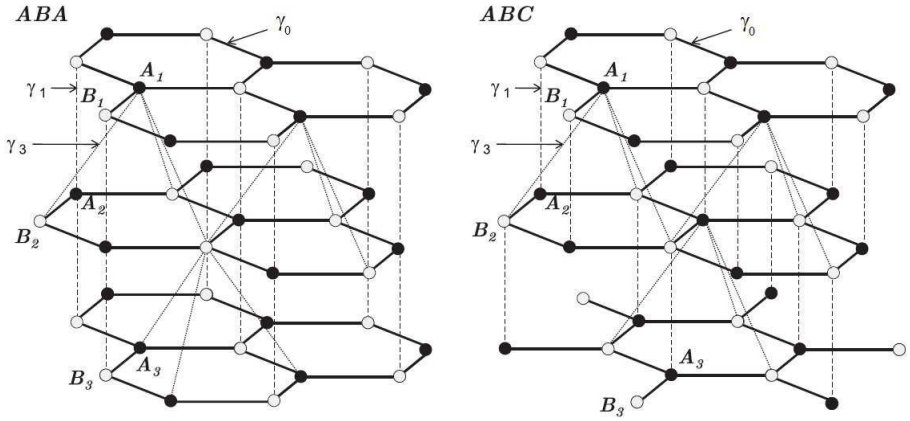

Figure 35: Crystalline structure of ABA and ABC-stacked TLG.[84].

$$\mathbf{H_K^{ABA}} = \begin{pmatrix} U_1 & v_F\pi^\dagger & \gamma_1 & 0 & 0 & 0 \\ v_F\pi & U_1 & 0 & 0 & 0 & 0 \\ \gamma_1 & 0 & U_2 & v_F\pi & \gamma_1 & 0 \\ 0 & 0 & v_F\pi^\dagger & U_2 & 0 & 0 \\ 0 & 0 & \gamma_1 & 0 & U_3 & v_F\pi^\dagger \\ 0 & 0 & 0 & 0 & v_F\pi & U_3 \end{pmatrix}, \tag{4.13}$$

$$\mathbf{H_K^{ABC}} = \begin{pmatrix} U_1 & v_F\pi^\dagger & \gamma_1 & 0 & 0 & 0 \\ v_F\pi & U_1 & 0 & 0 & 0 & 0 \\ \gamma_1 & 0 & U_2 & v_F\pi & 0 & 0 \\ 0 & 0 & v_F\pi^\dagger & U_2 & 0 & \gamma_1 \\ 0 & 0 & 0 & 0 & U_3 & v_F\pi^\dagger \\ 0 & 0 & 0 & \gamma_1 & v_F\pi & U_3 \end{pmatrix}, \tag{4.14}$$

By diagonalizing the above Hamiltonians, one finds the spectra shown in Fig. 36. Left panels show the electronic spectra of ABA TLG for (a) $U_1 = U_2 = U_3 = 0$; (c) $U_1 = 0.05$ eV, $U_2 = 0$, $U_3 = -0.05$ eV; (e) $U_1 = 0.1$ eV, $U_2 = 0.05$ eV, $U_3 = 0.025$ eV. The right panels show the spectra for ABC TLG with the same potential values. In the first row of figures all the six bands are shown, whereas the others show just the low energy bands ($E < \gamma_1$). Notice from Fig. 36 (a) that trilayers with ABA stacking have 4 low energy bands, which look like superposition of monolayer and bilayer spectrum. While panel (b) shows just 2 bands lying in this region. In addition, the two types of TLG behave very differently when subjected to gate potentials. In ABC stacking the gate voltage opens a

gap in the spectrum (see fig. 36(d) and (f)), whereas the potentials $U_1 = 0.05$ eV, $U_2 = 0$, $U_3 = -0.05$ cause a band overlap in TLG with ABA stacking. This behavior was recently experimentally observed by C. H. Lui *et al.* [86].

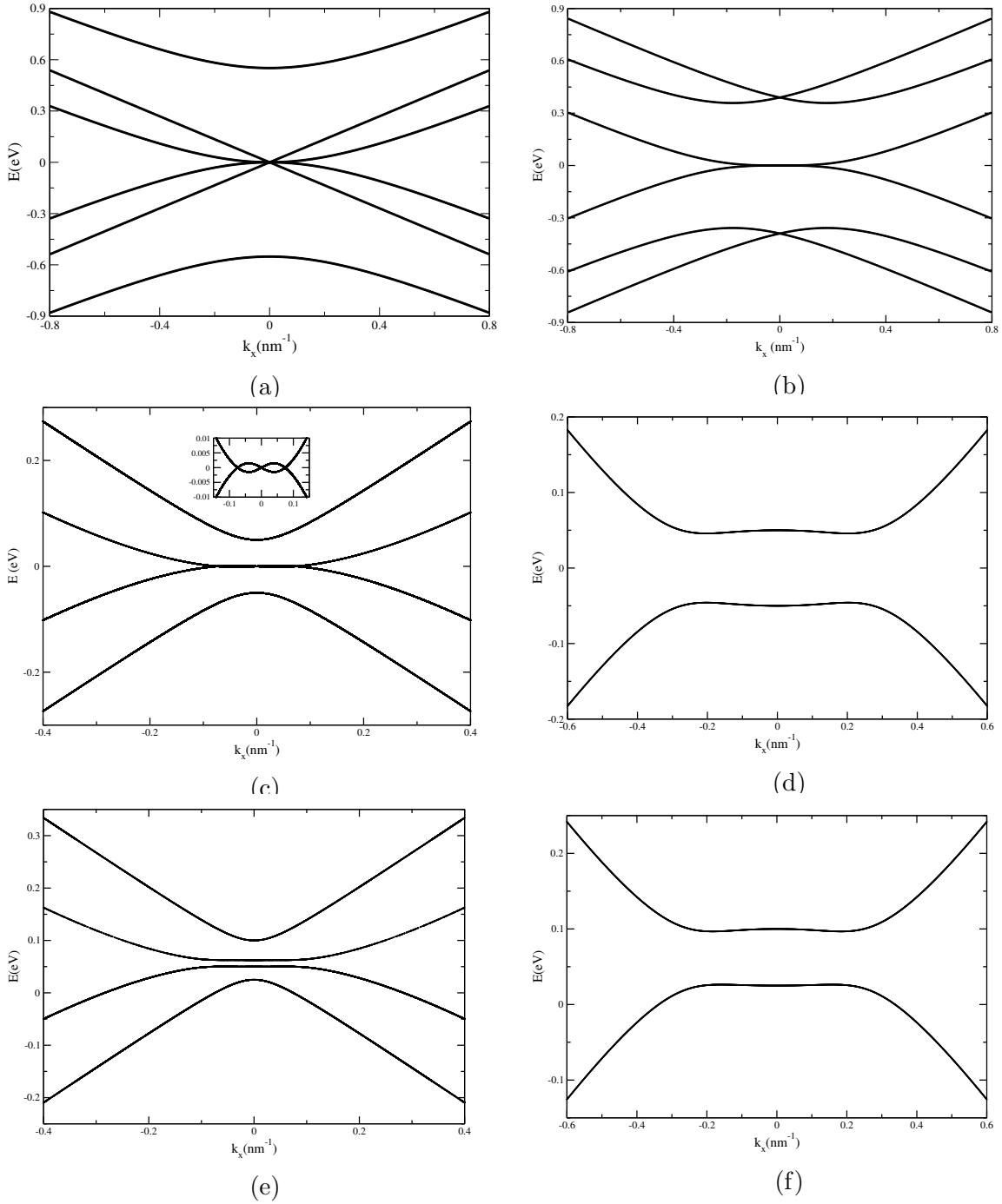

Figure 36: (Left panels) Free electronic spectrum of ABA TLG for (a) $U_1 = U_2 = U_3 = 0$; (c) $U_1 = 0.05$ eV, $U_2 = 0$, $U_3 = -0.05$ eV; (e) $U_1 = 0.1$ eV, $U_2 = 0.05$ eV, $U_3 = 0.025$ eV. (Right panels) The same as in the left panels for ABC TLG.

The next two chapters will be devoted to a detailed studying of LLs in TLG.

5 Landau levels in asymmetric graphene trilayers

In this chapter we investigate the properties of three coupled layers of graphene, i.e. trilayer graphene (TLG) in the presence of an external magnetic field perpendicular to the plane of the layers. The properties of TLG in the absence of a magnetic field have been considered in the literature within a tight-binding model (see, e.g. [70, 87]), as well as through first principles calculations [88]. The effect of an external magnetic field was calculated by means of an approximation based on the mapping of stacked graphene layers to an 1D tight-binding chain by Guinea *et al.* [71]. Recent experimental [89, 90, 91] and theoretical [82, 92, 93] studies have investigated the Landau-level spectrum of unbiased TLG and recent magnetoconductance measurements of TLG have been performed [94, 95, 96, 97]. These results showed that one important aspect of TLG is the fact that the energy bands at the vicinity of the Fermi energy are very sensitive to the particular type of stacking of the layers. The type of stacking is also relevant to the properties of the Landau levels of the TLG. The goal of the present chapter is to present analytical results for the spectrum of TLG in a magnetic field considering different potentials in each layer. In order to do that we perform a direct diagonalization of the six-band continuum model and obtain analytical expressions for the the Landau level spectrum as function of magnetic field and the potentials at each layer, for both the ABC and ABA stackings. In particular, we calculate the TLG spectrum in the presence of electric fields that break the layer symmetry. It has recently been shown that these different potentials can lead to the opening of a gap in the TLG spectrum [87, 98, 81, 86]. In the present work we focus on the modifications of the Landau levels as function of the layer potential.

5.1 ABA Stacking

Let us consider a system consisting of three coupled graphene layers, in the context of the tight-binding model. We assume nearest neighbor hopping between sites within

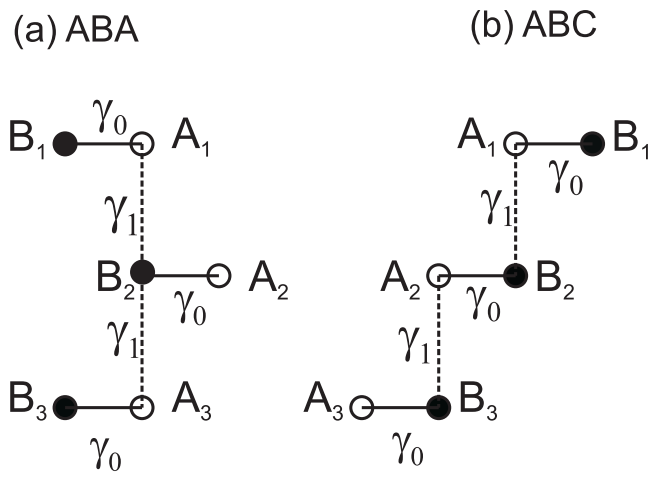

Figure 37: Diagramatic scheme of couplings in graphene trilayers for ABA (a) and ABC (b) stackings.

each layer, described by the coupling parameter γ_0. In the continuum approximation, this parameter determines the magnitude of the Fermi velocity $v_F = \gamma_0 a\hbar^{-1}3/2 \approx 10^6$ m/s. The nearest neighbor interlayer coupling scheme is $A_1 - B_2 - A_3$, with coupling parameter γ_1 (see Fig. 37). The Hamiltonian is given as

$$\mathbf{H} = \begin{pmatrix} U_1 + U_0 & v_F\pi^\dagger & \gamma_1 & 0 & 0 & 0 \\ v_F\pi & U_1 & 0 & 0 & 0 & 0 \\ \gamma_1 & 0 & U_2 + U_0 & v_F\pi & \gamma_1 & 0 \\ 0 & 0 & v_F\pi^\dagger & U_2 & 0 & 0 \\ 0 & 0 & \gamma_1 & 0 & U_3 + U_0 & v_F\pi^\dagger \\ 0 & 0 & 0 & 0 & v_F\pi & U_3 \end{pmatrix} \tag{5.1}$$

where $\pi = p_x + ip_y$, with $p_{x,y}$ being the components of the in-plane momentum; $U_{1,2,3}$ is the potential in each layer, respectively, U_0 is the onsite energy at sublattices A_1, B_2 and A_3, and we defined the eigenstates as $\Psi = [\psi_{A1}, \quad i\psi_{B1}, \quad \psi_{B2}, \quad i\psi_{A2}, \quad \psi_{A3}, \quad i\psi_{B3}]^T$. In the presence of a uniform magnetic field in the z direction, with the gauge $\vec{A} = (0, Bx, 0)$ and, for a given sublattice L, $\psi_L(y) = \phi_L e^{ik_y y}$, one obtains the following system of equations:

$$\mathcal{A}^+\phi_{B1} + \gamma_1'\phi_{B2} = (\epsilon - u_1 - u_0)\phi_{A1}, \tag{5.2a}$$

$$\mathcal{A}^-\phi_{A1} = -(\epsilon - u_1)\phi_{B1}, \tag{5.2b}$$

$$\mathcal{A}^-\phi_{A2} + \gamma_1'\phi_{A1} + \gamma_1'\phi_{A3} = (\epsilon - u_2 - u_0)\phi_{B2}, \tag{5.2c}$$

$$\mathcal{A}^{+}\phi_{B2} = -(\epsilon - u_2)\phi_{A2}, \tag{5.2d}$$

$$\mathcal{A}^{+}\phi_{B3} + \gamma_1'\phi_{B2} = (\epsilon - u_3 - u_0)\phi_{A3}, \tag{5.2e}$$

$$\mathcal{A}^{-}\phi_{A3} = -(\epsilon - u_3)\phi_{B3}, \tag{5.2f}$$

where $\epsilon = E/\hbar v_F$, $u_i = U_i/\hbar v_F$, $\gamma_1' = \gamma_1/\hbar v_F$ and $\beta = eB/\hbar$ and we defined the operators

$$\mathcal{A}^{\pm} = \frac{d}{dx} \pm (k_y - \beta x), \tag{5.3}$$

which obey the commutation relation $[\mathcal{A}^{+}, \mathcal{A}^{-}] = 2\beta$.

For $U_1 = U_2 = U_3 = U$ the system can be easily solved by making use of its reflection symmetry. Thus, we can define symmetric and antisymmetric combinations of the spinor components. For the antisymmetric case we obtain $\phi_G \equiv \frac{1}{\sqrt{2}}(\phi_{A1} - \phi_{A3})$, and $\phi_H \equiv \frac{1}{\sqrt{2}}(\phi_{B1} - \phi_{B3})$. That leads to the following pair of coupled equations

$$\mathcal{A}^{-}\phi_G = -(\epsilon - u)\phi_H, \tag{5.4a}$$

$$\mathcal{A}^{+}\phi_H = (\epsilon - u - u_0)\phi_G. \tag{5.4b}$$

For the sake of convenience, let us now define the operator

$$Z \equiv \mathcal{A}^{-}\mathcal{A}^{+} = \frac{d^2}{dx^2} - (k_y - \beta x)^2 - \beta. \tag{5.5}$$

We can now decouple the equations to obtain

$$(Z + 2\beta)\phi_G = -[(\epsilon - u')^2 - (\delta u)^2]\phi_G, \tag{5.6}$$

which corresponds to the equation that gives the spectrum for a *single* graphene layer under an effective electrostatic potential $U' = U + U_0/2$ as well as a finite gap term given by $\delta U = U_0/2$. Thus, the Landau level spectrum in this case is given by $\epsilon = u' \pm \sqrt{2\beta n + (\delta u)^2}$. Thus, the effect of the term U_0 is only to introduce a small shift of the dispersion branches and to generate a small gap in the energy spectrum.

For the symmetric case we have $\phi_C \equiv \frac{1}{\sqrt{2}}(\phi_{A1} + \phi_{A3})$ and $\phi_D \equiv \frac{1}{\sqrt{2}}(\phi_{B1} + \phi_{B3})$. The equations become

$$\mathcal{A}^{+}\phi_D + \sqrt{2}\gamma_1'\phi_{B2} = (\epsilon - u - u_0)\phi_C, \tag{5.7a}$$

$$\mathcal{A}^{-}\phi_C = -(\epsilon - u)\phi_D, \tag{5.7b}$$

and

$$\mathcal{A}^{-}\phi_{A2} + \sqrt{2}\gamma_1'\phi_C = (\epsilon - u - u_0)\phi_{B2}, \tag{5.7c}$$

$$\mathcal{A}^{+}\phi_{B2} = -(\epsilon - u)\phi_{A2}, \tag{5.7d}$$

These equations can be decoupled, resulting in the fourth-order differential equation

$$\{Z^2 + \lambda_1 Z - \lambda_2\}\phi_C = 0 \tag{5.8}$$

where $\lambda_1 = 2(\epsilon - u - u_0)(\epsilon - u) + 2\beta$, and $\lambda_2 = -(\epsilon - u - u_0)^2(\epsilon - u)^2 + 2(\gamma_1')^2(\epsilon - u)^2$. This equation is similar to the one describing bilayer graphene. A second-order equation can be obtained by calculating the roots of the second-order equation as

$$\{Z - z_+\}\{Z - z_-\}\phi_C = 0 \tag{5.9}$$

with

$$z_\pm = -\frac{\lambda_1}{2} \pm \sqrt{\left(\frac{\lambda_1}{2}\right)^2 + \lambda_2}, \tag{5.10}$$

where we set $k_y = 0$, since this term only introduces a shift of the wavefunction In particular, for $u_0 = 0$ the equations yield results that are identical to those of a gapless single-layer and bilayer graphene, i.e. the Landau levels are found as the solutions of $2\beta(n+1) = z_\pm$. As in the previous case, the addition of remote coupling terms introduces a gap in the spectrum.

A more realistic description of TLG structures should take into account asymmetries between the different layers, which can be brought about by the interaction with a substrate or by gating. In order to assess the effect of layer symmetry breaking in the spectrum, let us now consider the case $U_1 \neq U_2 \neq U_3$. In addition, we now consider $U_0 = 0$, since we assume that the shifts caused by the layer potentials are more significant than the effect of this term. A simple substitution allows us to write

$$[\mathcal{A}^{+}\mathcal{A}^{-} + (\epsilon - u_1)^2]\phi_{A1} = \gamma_1'(\epsilon - u_1)\phi_{B2},$$

$$[\mathcal{A}^{+}\mathcal{A}^{-} + (\epsilon - u_3)^2]\phi_{A3} = \gamma_1'(\epsilon - u_3)\phi_{B2}. \tag{5.11}$$

In addition, we also have

$$[\mathcal{A}^-\mathcal{A}^+ + (\epsilon - u_2)^2]\phi_{B2} = \gamma_1'(\epsilon - u_2)(\phi_{A1} + \phi_{A3}). \tag{5.12}$$

As in the previous case, we introduce symmetric and antisymmetric combinations of wavefunctions, and let us also define $\Delta = (u_1 - u_3)/2$, $s = (u_1 + u_3)/2$ and $\delta_j = \epsilon - u_j$, $j = 1, 2, 3$, in order to simplify the notation. Thus, after some algebra, we can obtain the following 6th-order differential equation for ϕ_{B2} as

$$\begin{aligned}\Big\{[\mathcal{A}^-\mathcal{A}^+ \;+\; \delta_1^2 + 2\beta][\mathcal{A}^-\mathcal{A}^+ + {\delta_2}^2][\mathcal{A}^-\mathcal{A}^+ + {\delta_3}^2 + 2\beta] \\ -\gamma_1'^2\delta_2(\epsilon - s)[\mathcal{A}^-\mathcal{A}^+ + {\delta_1}^2 + 2\beta] \\ -\gamma_1'^2\delta_2(\epsilon - s)[\mathcal{A}^-\mathcal{A}^+ + {\delta_3}^2 + 2\beta] \\ +4\gamma_1'^2\Delta^2\delta_2(\epsilon - s)\Big\}\phi_{B2} = 0.\end{aligned} \tag{5.13}$$

It is seen that for $U_1 = U_2 = U_3$ (i.e. $\delta_1 = \delta_2 = \delta_3$, $\Delta = 0$), we recover the previous solutions. One can rewrite Eq. (5.13) as

$$[Z^3 + \alpha_1 Z^2 + \alpha_2 Z + \alpha_3]\phi_{B2} = 0. \tag{5.14}$$

with the Z operator defined above and

$$\alpha_1 \equiv \quad \delta_1^2 + \delta_2^2 + \delta_3^2 + 4\beta, \tag{5.15a}$$

$$\begin{aligned}\alpha_2 \equiv \quad & (\delta_1^2 + 2\beta)(\delta_3^2 + 2\beta) + (\delta_1^2 + 2\beta)\delta_2^2 + (\delta_3^2 + 2\beta)\delta_2^2 \\ & -\gamma_1'^2\delta_2(\delta_1 + \delta_3),\end{aligned} \tag{5.15b}$$

$$\begin{aligned}\alpha_3 \equiv \quad & (\delta_1^2 + 2\beta)\delta_2^2(\delta_3^2 + 2\beta) - 2\beta\gamma_1'^2\delta_2(\delta_1 + \delta_3) \\ & -\gamma_1'^2\delta_1\delta_2\delta_3(\delta_1 + \delta_3),\end{aligned} \tag{5.15c}$$

This equation can be written as

$$\{Z - Z_1\}\{Z - Z_2\}\{Z - Z_3\}\phi_{B2} = 0, \tag{5.16}$$

where Z_j, $j = 1, 2, 3$ are the three roots of the cubic equation, Eq. (5.14). Therefore, the

spinor component ϕ_{B2} is a solutions of

$$-\frac{d^2\phi_{B2}}{dx^2} + (k_y - \beta x)^2\phi_{B2} = -(Z_j + \beta)\phi_{B2}. \tag{5.17}$$

For zero magnetic field, this equation allows us to obtain plane wave solutions for each dispersion branch. The dispersion relation can be obtained by setting $Z_j = -k^2$. It can be immediately seen that the energy gap at $k = 0$ can be found by solving the equation $\alpha_3 = 0$. For finite magnetic fields, the solutions are expressed in terms of Hermite polynomials. Therefore, for the Landau levels we obtain the relation $Z_j = -2\beta(n+1)$. Thus, the energies are found by solving the algebraic equation

$$-[2\beta(n+1)]^3 + \alpha_1[2\beta(n+1)]^2 - \alpha_2[2\beta(n+1)] + \alpha_3 = 0. \tag{5.18}$$

It is evident that for $U_1 = U_2 = U_3$, we have $\Delta = 0$ and the last term of Eq. (5.13) vanishes. The spectrum should then consist of a superposition of the spectra of single layer graphene and bilayer graphene.

5.2 ABC Stacking

Let us consider three coupled graphene layers in the ABC stacking configuration. For the sake of simplicity, let us retain only the nearest-neighbor coupling terms. In this case, the Hamiltonian can be written as

$$\mathcal{H} = \begin{pmatrix} U_1 & v_F\pi^\dagger & \gamma_1 & 0 & 0 & 0 \\ v_F\pi & U_1 & 0 & 0 & 0 & 0 \\ \gamma_1 & 0 & U_2 & v_F\pi & 0 & 0 \\ 0 & 0 & v_F\pi^\dagger & U_2 & 0 & \gamma_1 \\ 0 & 0 & 0 & 0 & U_3 & v_F\pi^\dagger \\ 0 & 0 & 0 & \gamma_1 & v_F\pi & U_3 \end{pmatrix} \tag{5.19}$$

where $U_{1,2,3}$ is the potential in each layer, respectively, and we defined the eigenstates as before.

Thus, one can obtain the following system of equations:

$$\mathcal{A}^+\phi_{B1} + \gamma_1'\phi_{B2} = (\epsilon - u_1)\phi_{A1}, \tag{5.20a}$$

$$\mathcal{A}^-\phi_{A1} = -(\epsilon - u_1)\phi_{B1}, \tag{5.20b}$$

$$\mathcal{A}^{-}\phi_{A2} + \gamma_1'\phi_{A1} = (\epsilon - u_2)\phi_{B2}, \tag{5.20c}$$

$$\mathcal{A}^{+}\phi_{B2} - \gamma_1'\phi_{B3} = -(\epsilon - u_2)\phi_{A2}, \tag{5.20d}$$

$$\mathcal{A}^{+}\phi_{B3} = (\epsilon - u_3)\phi_{A3}, \tag{5.20e}$$

$$\mathcal{A}^{-}\phi_{A3} - \gamma_1'\phi_{A2} = -(\epsilon - u_3)\phi_{B3}, \tag{5.20f}$$

where $\epsilon = E/\hbar v_F$, $u_i = U_i/\hbar v_F$, $\gamma_1' = \gamma_1/\hbar v_F$ and $\beta = eB/\hbar v_F$. In order to decouple these equations, let us first obtain ϕ_{B1} and ϕ_{A3} in terms of ϕ_{A1} and ϕ_{B3} from the second and fifth equations as

$$\phi_{B1} = -\frac{1}{(\epsilon - u_1)}\mathcal{A}^{-}\phi_{A1}, \qquad \phi_{A3} = \frac{1}{(\epsilon - u_3)}\mathcal{A}^{+}\phi_{B3}, \tag{5.21}$$

and substitute these expressions in the first and sixth equations, respectively, to give

$$\mathcal{A}^{+}\mathcal{A}^{-}\phi_{A1} - \gamma_1'(\epsilon - u_1)\phi_{B2} = -(\epsilon - u_1)^2\phi_{A1}, \tag{5.22a}$$

$$\mathcal{A}^{-}\mathcal{A}^{+}\phi_{B3} - \gamma_1'(\epsilon - u_3)\phi_{A2} = -(\epsilon - u_3)^2\phi_{B3}. \tag{5.22b}$$

Equations (5.22a) and (5.22b) allow us to obtain ϕ_{B2} and ϕ_{A2} in terms of ϕ_{A1} and ϕ_{B3}, respectively. Thus, by substituting them in Eqs. (5.20c) and (5.20d), respectively, and after some tedious algebra, one can obtain a 6th order differential equation as

$$\begin{aligned}\Big\{&[\mathcal{A}^{-}\mathcal{A}^{+} + \delta_1^2 + 2\beta][\mathcal{A}^{-}\mathcal{A}^{+} + \delta_2^2][\mathcal{A}^{-}\mathcal{A}^{+} + \delta_3^2 - 2\beta] \\ &- \gamma_1'^2\delta_2\delta_3[\mathcal{A}^{-}\mathcal{A}^{+} + \delta_1^2 + 2\beta] \\ &- \gamma_1'^2\delta_1\delta_2[\mathcal{A}^{-}\mathcal{A}^{+} + \delta_3^2 - 2\beta] + \gamma_1'^4\delta_1\delta_3\Big\}\phi_{A1} = 0.\end{aligned} \tag{5.23}$$

It is interesting to compare Eqs. (5.13) and (5.23). The former remains invariant if one switches the potentials in layers 1 and 3. Equation (5.23), on the other hand, is found to be invariant under an interchange of potentials between the topmost and lowest layers together with a reversal of the magnetic field. This reflects the different symmetries of each stacking of TLG.

As before, we can obtain the Landau level spectrum by rewritting Eq. (5.23) as

$$[Z^3 + \gamma_1 Z^2 + \gamma_2 Z + \gamma_3]\phi_{A1} = 0, \tag{5.24}$$

with $Z \equiv \mathcal{A}^{-}\mathcal{A}^{+}$, and

$$\gamma_1 \equiv \quad (\delta_1^2 + \delta_2^2 + \delta_3^2), \tag{5.25a}$$

$$\gamma_2 \equiv \quad (\delta_1^2 + 2\beta)(\delta_3^2 - 2\beta) + (\delta_1^2 + 2\beta)\delta_2^2 + (\delta_3^2 - 2\beta)\delta_2^2$$

$$-(\gamma_1')^2(\delta_1 + \delta_3)\delta_2 \tag{5.25b}$$

$$\gamma_3 \equiv \quad -(\gamma_1')^2\delta_2[\delta_3(\delta_1^2 + 2\beta) + \delta_1(\delta_3^2 - 2\beta)] + (\gamma_1')^4\delta_1\delta_3$$

$$+(\delta_1\delta_2\delta_3)^2 + 2\beta(\delta_3^2 - \delta_1^2)\delta_2^2 - 4(\beta\delta_2)^2, \tag{5.25c}$$

This equation can be written as

$$\{Z - Z_1\}\{Z - Z_2\}\{Z - Z_3\}\phi_{A1} = 0, \tag{5.26}$$

where Z_j, $j = 1, 2, 3$ are the three roots of the cubic equation, Eq. (5.24). Therefore the spinor component ϕ_{A1} is found as a solution of

$$-\frac{d^2\phi_{A1}}{dx^2} + (k_y - \beta x)^2\phi_{A1} = -(Z_j + \beta)\phi_{A1}. \tag{5.27}$$

For the particular case of $U_1 = U_2 = U_3 = 0$ and zero magnetic field, we can obtain plane wave solutions by setting $Z_j = -k^2$, where k is the in-plane wavevector. Thus, Eq. (5.24) can be rewritten as

$$\epsilon^6 - (3k^2 + 2\gamma_1'^2)\epsilon^4 + (3k^4 - 2k^2\gamma_1'^2 + \gamma_1'^4)\epsilon^2 - k^6 = 0. \tag{5.28}$$

Let us now consider the low-energy limit $\epsilon << \gamma_1'$. That allows us to neglect the higher-order powers of ϵ to obtain

$$\epsilon \approx \frac{k^3}{\gamma_1'^2}\frac{1}{\sqrt{1 - 2k^2/\gamma_1'^2 + 3k^4/\gamma_1'^4}}. \tag{5.29}$$

Thus, for small wavevectors, the dispersion relation increases with the third power of k.

The Landau levels can be obtained using the relation $Z_j = -2\beta(n + 1)$, which leads to the algebraic equation

$$-[2\beta(n + 1)]^3 + \gamma_1[2\beta(n + 1)]^2 - \gamma_2[2\beta(n + 1)] + \gamma_3 = 0. \tag{5.30}$$

As seen above, for zero potential in each layer, we can find a simpler algebraic relation

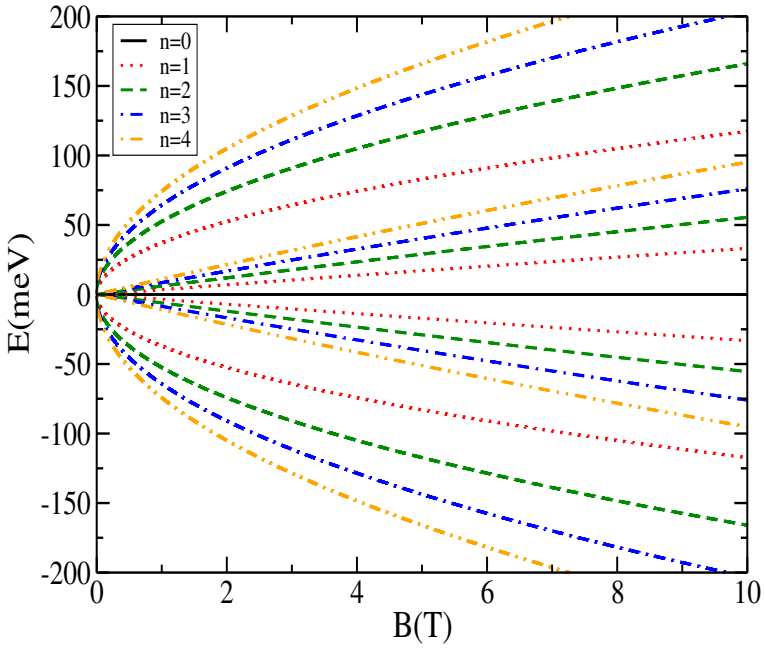

Figure 38: The lowest Landau levels as function of magnetic field for ABA-stacked graphene trilayers calculated from Eq. (5.18), with $U_1 = U_2 = U_3 = 0$, for $n = 0$ (black solid lines), $n = 1$ (red dotted lines), $n = 2$ (green dashed lines), $n = 3$ (blue dot-dashed lines) and 4 (yellow dot-dot-dashed lines).

for the energy, namely

$$\epsilon^6 - [6\beta(n+1) + 2\gamma_1'^2]\epsilon^4$$

$$+[12\beta^2(n+1)^2 - 4\beta(n+1)\gamma_1'^2 + \gamma_1'^4 - 4\beta^2]\epsilon^2$$

$$-8\beta^3(n+1)^3 + 8\beta^3(n+1) = 0. \tag{5.31}$$

For $\epsilon << \gamma_1$ we can then obtain

$$\epsilon \approx \pm \frac{(2\beta)^{3/2}}{\gamma_1'^2}\sqrt{n(n+1)(n+2)}F(\beta, n), \tag{5.32}$$

where

$$F(\beta, n) = \left[1 - 4\frac{\beta}{\gamma_1'^2}(n+1) - 4\frac{\beta^2}{\gamma_1'^4} + 12\frac{\beta^2}{\gamma_1'^4}(n+1)^2\right]^{-1/2}. \tag{5.33}$$

For small fields (i.e. $\beta << \gamma_1'^2$), $F(\beta, n) \approx 1$. Therefore, in the limit of low energies and small fields, the Landau levels should approximately depend on the magnetic field as $B^{3/2}$, in agreement with the results of Ref. [70].

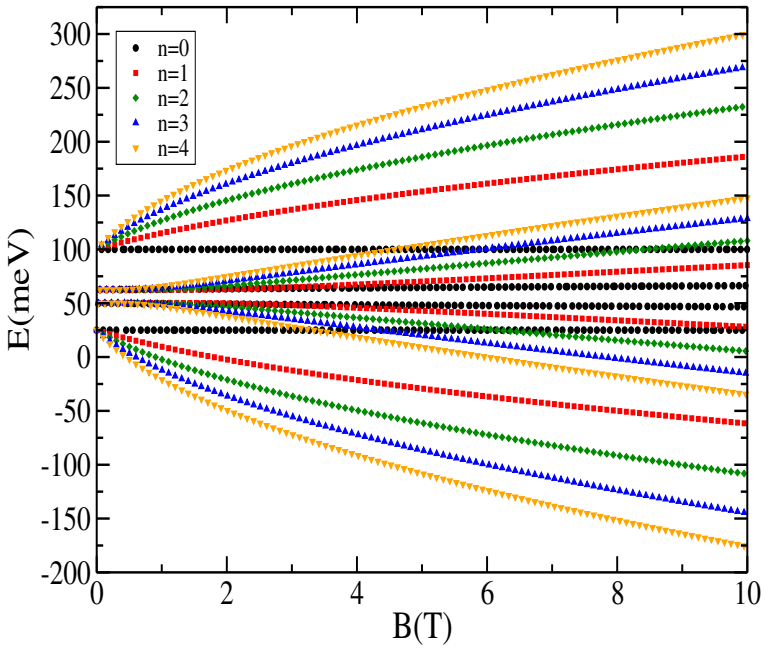

Figure 39: Energy spectrum as function of magnetic field for ABA-stacked graphene trilayers, for $U_1 = 100$ meV, $U_2 = 50$ meV and $U_3 = 25$ meV, $n = 0$ (black dots), $n = 1$ (red squares), $n = 2$ (blue lozenges), $n = 3$ (green triangles) and 4 (yellow triangles).

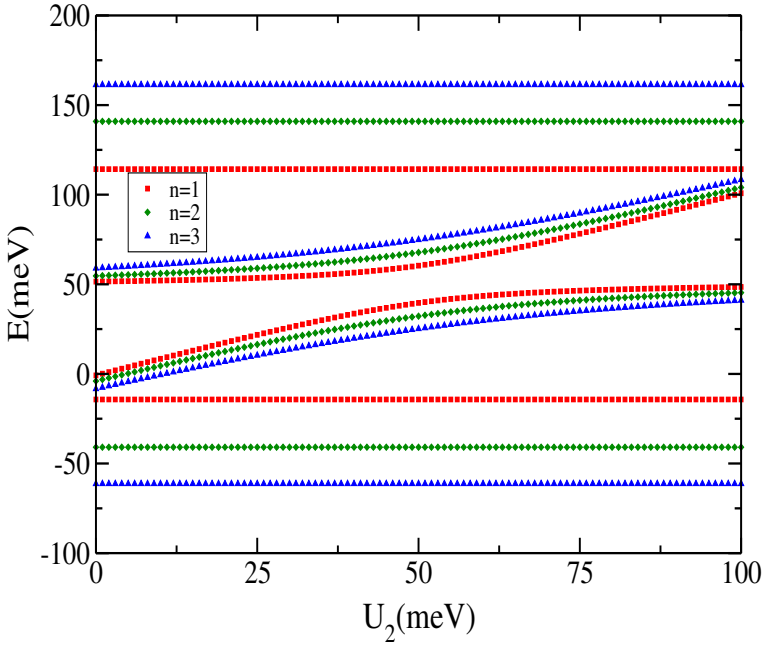

Figure 40: Low-lying Landau levels as function of the potential in the inner layer for ABA-stacked graphene trilayers, for $n = 1$ (red squares), 2 (green lozenges) and 3 (blue squares) for $B = 3$ T, $U_1 = U_3 = 50$ meV.

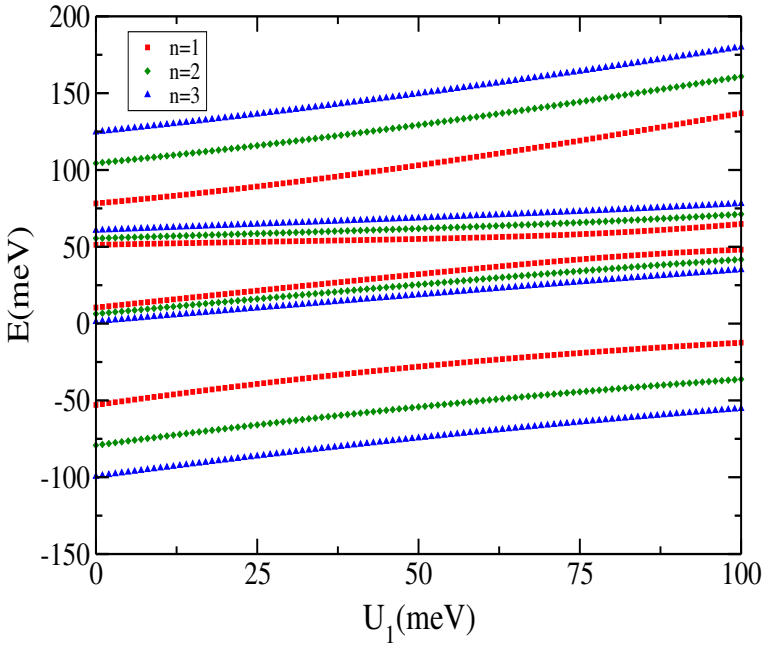

Figure 41: Low-lying Landau levels as function of the potential in the uppermost layer for ABA-stacked graphene trilayers, for $n = 1$ (red squares), 2 (green lozenges) and 3 (blue squares) for $B = 3$ T, $U_2 = 50$ meV, $U_3 = 25$ meV.

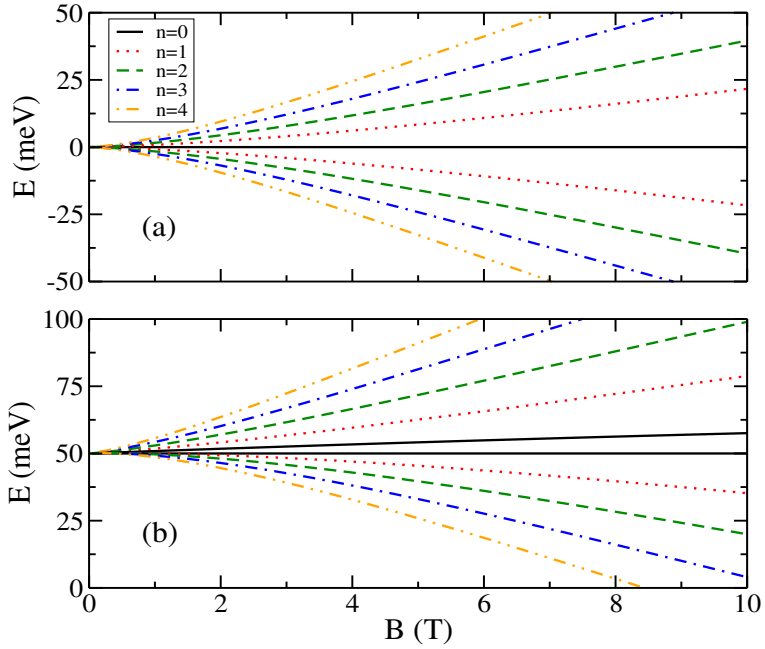

Figure 42: Landau level spectrum for the trilayer graphene for the ABC stacking, as function of magnetic field, with $U_1 = U_2 = U_3 = 0$ (a), and $U_1 = U_3 = 50$ meV, $U_2 = 100$ meV (b) for $n = 0$ (black solid lines), $n = 1$ (red dotted lines), $n = 2$ (green dashed lines), $n = 3$ (blue dot-dashed lines) and 4 (yellow dot-dot-dashed lines).

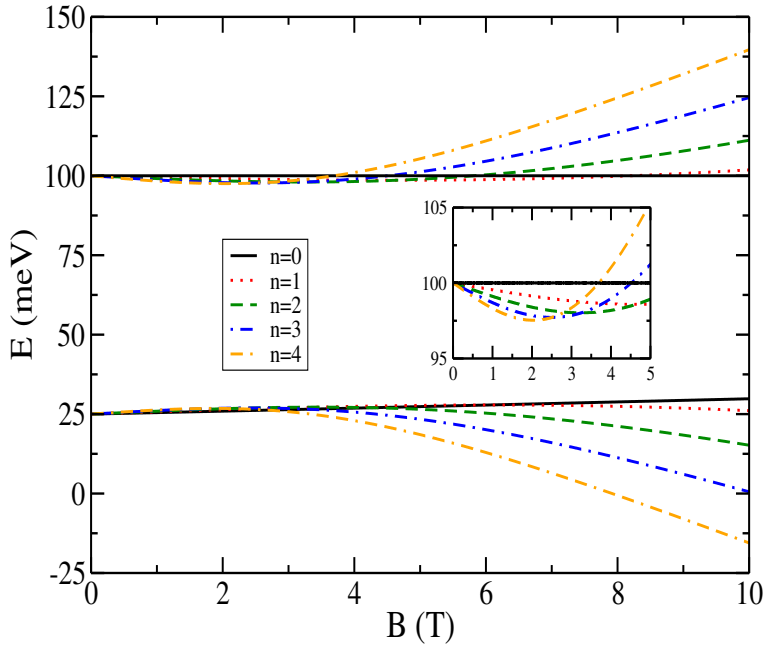

Figure 43: Landau level spectrum for the trilayer graphene for the ABC stacking, as function of magnetic field, with $U_1 = 100$ meV, $U_2 = 50$ meV, and $U_3 = 25$ meV, for $n = 0$ (black solid lines), $n = 1$ (red dotted lines), $n = 2$ (green dashed lines), $n = 3$ (blue dot-dashed lines) and 4 (yellow dot-dot-dashed lines).

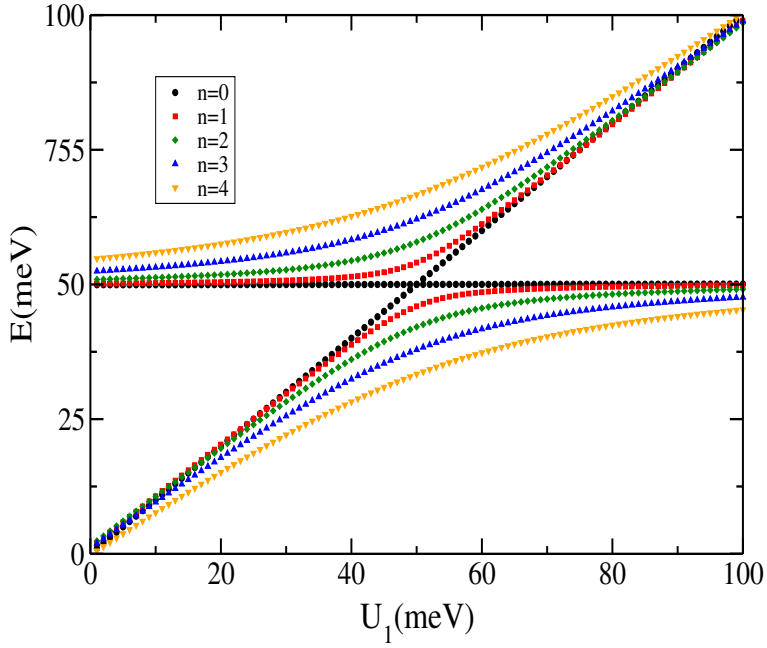

Figure 44: Landau level spectrum for ABC-stacked trilayer graphene as function of U_1, for $B = 3$ T and $U_2 = U_3 = 50$ meV, with $n = 0$ (black dots), $n = 1$ (red squares), $n = 2$ (blue lozenges), $n = 3$ (green triangles) and 4 (yellow triangles).

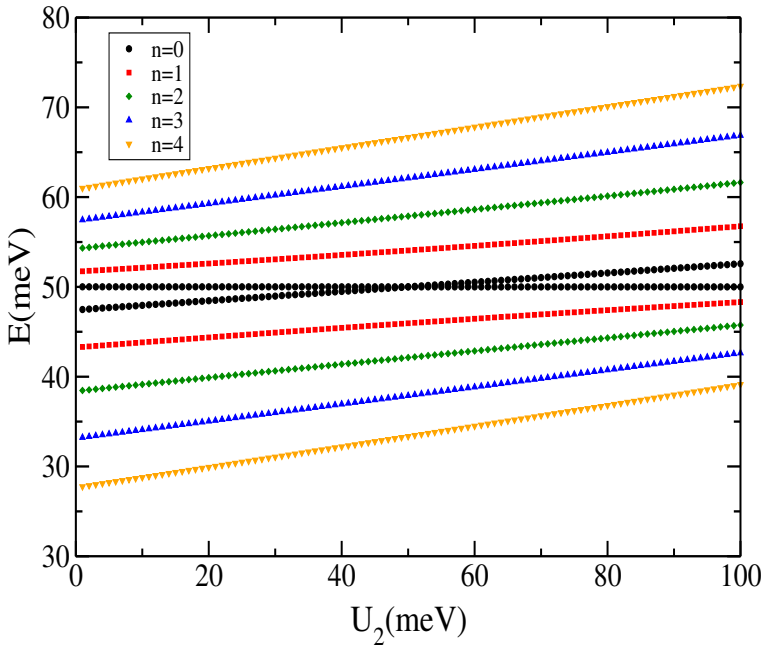

Figure 45: Landau level spectrum for ABC-stacked trilayer graphene as function of U_2, for $B = 3$ T and $U_1 = U_3 = 50$ meV, with $n = 0$ (black dots), $n = 1$ (red squares), $n = 2$ (blue lozenges), $n = 3$ (green triangles) and 4 (yellow triangles).

5.3 Numerical Results

Let us first consider the ABA case. Figure 38 shows the field dependence of the low-lying Landau levels calculated from Eq. (5.18), with $U_1 = U_2 = U_3 = 0$, for $n = 0$ (black solid lines), $n = 1$ (red dotted lines), $n = 2$ (green dashed lines), $n = 3$ (blue dot-dashed lines) and 4 (yellow dot-dot-dashed lines). We find that for every value of n there are two different types of low-energy branches: 1) those that depend linearly on the magnetic field (i.e. "bilayer-like" behavior), and 2) branches that display a $B^{1/2}$ dependence ("monolayer-like" branches). A third set of bilayer-like branches are found around $E = \pm t_1$ not shown in the figure.

The effect of a potential difference between the layers on the energy spectrum as function of magnetic field is shown in Fig. 39. As in the previous case, the figure shows branches corresponding to $n = 0 - 4$. The potentials in the different graphene layers are $U_1 = 100$ meV, $U_2 = 50$ meV and $U_3 = 25$ meV. As seen from Eq. (5.24), for $B \to 0$ we have solutions corresponding to $E = U_j$, $j = 1, 2, 3$ and $E = (U_1 + U_3)/2$. Thus, we find that the "monolayer-like" branches are shifted creating a gap with magnitude $U_1 - U_3$, whereas for the "bilayer-like" states a smaller gap opens with magnitude $(U_1+U_3)/2-U_2$. One consequence of this difference is the appearance of level crossing as the magnetic field

is increased.

Figure 40 shows the low-energy Landau levels as function of the potential in the inner layer, for the ABA case, for $n = 1$ (red squares), 2 (green lozenges) and 3 (blue squares) for $B = 3$ T, $U_1 = U_3 = 50$ meV. Notice that: 1) the lowest energy levels depend linearly on U_2 for small U_2 ($<< U_1 = U_3$) and for large U_2 ($>> U_1 = U_3$) values, and exhibit an anticrossing behavior for $U_2 \approx U_1 = U_3$; 2) the higher energy states are not affected by the bias. A different behaviour is observed when one varies the potential at the uppermost layer (U_1), as seen in Fig. 41. In contrast with the previous case, the bias is seen to cause a significant shift also on higher-energy Landau levels.

The energy spectrum for the ABC case is shown in Fig. 42a, as function of magnetic field and with $U_1 = U_2 = U_3 = 0$, for $n = 0 - 4$. For small B-values we see a doubly-degenerate branch with $E = 0$, and a $B^{3/2}$-behavior for the remaining branches, which turns into a linear behavior at large E. In comparison with the previous case, the results in the ABC case show the presence of pairs of branches at low energies, whereas in the ABA case one finds two sets of energy levels for each Landau index. That is caused by the fact that, in the ABC case, the remaining four branches are found around $E = \pm t$, with $t \approx 400$ meV.

Figure 42b shows results for an ABC TLG with $U_1 = U_3 = 50$ meV, whereas $U_2 = 100$ meV. In this case, the main effect of the potential difference is the lifting of the degeneracy of the $n = 0$ state and a shift of the whole spectrum to lower energy with increasing magnetic field.

In contrast, Fig. 43 shows the LL spectrum for $U_1 = 100$, $U_2 = 50$ and $U_3 = 25$ meV. The inset shows an enlargement of the region around $E = 100$ meV. In this case, the bias creates an energy gap, which can be found by setting $\beta = 0$ in Eq. (5.45), which leads to solutions with $E = U_1$ and $E = U_2$. Notice also the existence of level crossings, as well as the peculiar small magnetic field behavior where there is a reversal of the ordering of the Landau levels as compared to the regular high magnetic field behavior.

Results for the dependence of the energy spectrum on U_1 is shown in Fig. 44, for $B = 3$ T and $U_2 = U_3 = 50$ meV. As seen, the degeneracy of the $n = 0$ is lifted for $U_1 \neq U_2, U_3$. Moreover, when the magnitude of the potential in the uppermost layer is increased, the Landau levels tend to become degenerate. A quite distinct picture emerges if one varies instead the potential in the middle layer (U_2), as shown in Fig. 45, for $B = 3$ T and $U_1 = U_3 = 50$ meV. In contrast with the previous results, the spectrum shows a linear dependence on the potential and there are no degeneracies for the different Landau

indices. As in the previous figure, a single Landau level at $E = 50$ meV is found to be unaffected by the bias.

6 Cyclotron resonance of trilayer graphene

Along the last chapter we investigated how the difference in stacking order affects the LL behavior in trilayer graphene (TLG) [84, 99] and verified that, within the simplest tight-binding model, the LL spectrum of ABA TLG is found to be a superposition of a monolayer-like and bilayer-like LLs[71, 93, 99, 100, 101]. In contrast, the ABC TLG are predicted to have a nearly $B^{3/2}$ field dependence.[71, 99, 101, 102]. These stacking-dependent behavior produce another two new types of integer quantum Hall effect[89, 91].

Along this chapter we will concentrate on the cyclotron resonance transitions in different stacked TLG. We will compare the results of unbiased and biased layers, and discuss as well the different features appearing due to the stacking order in ABC and ABA TLG. We will concentrate on the position of the cyclotron resonance peaks, and the oscillator strength of those transitions.

6.1 ABC Stacking

Let us consider three coupled graphene layers with an ABC stacking configuration in the continuum approximation. In the present work we retain only the nearest-neighbor coupling terms. In this case, the Hamiltonian can be written as

$$\mathcal{H}^{ABC} = \begin{pmatrix} U_1 & v_F\pi^\dagger & \gamma_1 & 0 & 0 & 0 \\ v_F\pi & U_1 & 0 & 0 & 0 & 0 \\ \gamma_1 & 0 & U_2 & v_F\pi & 0 & 0 \\ 0 & 0 & v_F\pi^\dagger & U_2 & 0 & \gamma_1 \\ 0 & 0 & 0 & 0 & U_3 & v_F\pi^\dagger \\ 0 & 0 & 0 & \gamma_1 & v_F\pi & U_3 \end{pmatrix} \tag{6.1}$$

whose eigenstates are defined by the six components spinor $\Psi = [\psi_{A_1},\ \psi_{B_1},\ \psi_{B_2},\ \psi_{A_2},\ \psi_{A_3},\ \psi_{B_3}]^T$. In the above Hamiltonian $\pi \equiv p_x + ip_y$, $\pi^\dagger \equiv p_x - ip_y$, $v_F = \sqrt{3}a\gamma_0/(2\hbar)$ is the Fermi velocity in terms of the in-plane nearest neighbor hopping $\gamma_0 = 3.12$ eV and the carbon-carbon distance $a = 1.42$ $\mathring{A}$. U_i ($i = 1, 2, 3$) is the potential in each layer which we consider constant throughout each layer, and $\gamma_1 = 0.4$ eV is the nearest neighbour coupling term between adjacent layers. In the presence of a magnetic field $\mathbf{p} \rightarrow \mathbf{p}+|e|\mathbf{A}$, where e is the electron charge. By making use of the Landau gauge $\mathbf{A} = B(0, x, 0)$, we have $[p_y, H] = 0$ and the eigenstates are found to be $\Psi_n^{ABC} = A_n \left[id_n\psi_{n+1} \ \ \frac{-d_n}{\delta_1^n l_B}\psi_{n+2} \ \ ic_n\psi_{n+1} \ \ b_n\psi_n \ \ \frac{-i2n}{\delta_3^n l_B}\psi_{n-1} \ \ \psi_n \right]^T$, with ψ_n given by

$$\psi_n = e^{ik_y y} e^{-\bar{x}^2/2} H_n(\bar{x}), \tag{6.2}$$

where $\bar{x} \equiv x/l_B + l_B k_y$, $l_B \equiv \sqrt{\hbar/eB}$ is the magnetic length, $\delta_i^n \equiv (E_n - U_i)/(\hbar v_F)$, $H_n(\bar{x})$ is the Hermite polynomial, and $\psi_n \equiv 0$ for $n < 0$. The other constants appearing in Ψ_n^{ABC} are defined in Appendix A.

The magnetic field dependence of the LL are shown in Fig. 46. The levels for unbiased layers are shown in Fig. 46(a) where they behave as $B^{3/2}$ for low fields and become linear in B for large fields. [99] When a bias is present, we show as an example in Fig. 46(b) the LL for $U_1 = 100$ meV, $U_2 = 50$ meV, $U_3 = 25$ meV. The arrows indicate some of the allowed transitions dictated by the dipole selection rule.

The oscillator strength (OS) of the transition between the initial state $|\Psi_n\rangle$ and the final one $|\Psi_m\rangle$ is usually defined within the dipole approximation in terms of $|\langle\Psi_m|x|\Psi_n\rangle|^2$. Since the only effect of k_y is to shift the symmetry center of the wave function and the system is assumed to be infinitely extended, we set $k_y = 0$ and work with the dimensionless quantity

$$\begin{aligned} f_{mn} =& \frac{1}{{l_B}^2}\left| \int \Psi_m^* x \Psi_n dx \right|^2 \\ =& {l_B}^2 \left| \sum_C \int \Psi_C^{m*} \bar{x} \Psi_C^n d\bar{x} \right|^2, \end{aligned} \tag{6.3}$$

with $C = A_1, B_1, B_2, A_2, A_3, B_3$ that are defined in the inset of Fig. 46(a). The analytical results of these integrals are given in Appendix A. Throughout the chapter we will refer to a transition from the state $|\Psi_n\rangle$ to $|\Psi_m\rangle$ as (n, m).

Figure 47(a) shows the most important energy transitions ΔE in ABC TLG as a function of the magnetic field for the levels displayed in 46(a). The black solid, red dashed and

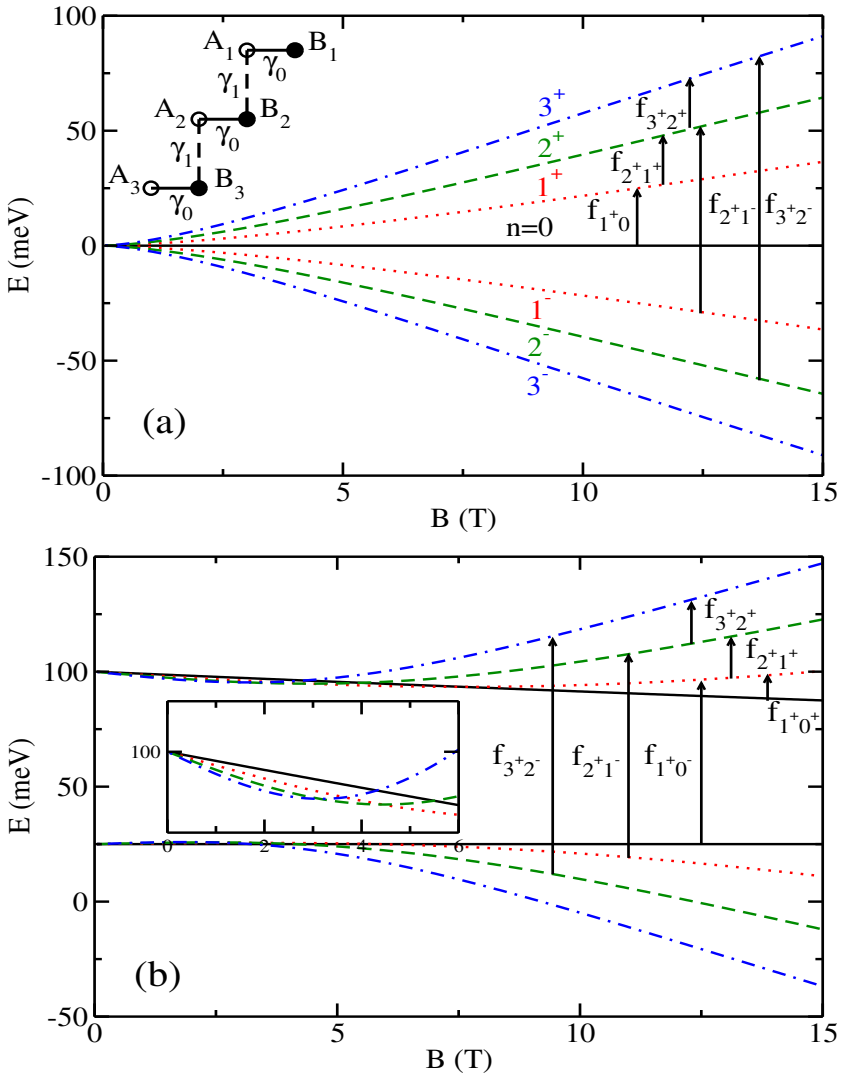

Figure 46: The TLG Landau-level spectrum as a function of magnetic field for ABC stacking with (a) $U_1 = U_2 = U_3 = 0$, and (b) $U_1 = 100$ meV, $U_2 = 50$ meV, $U_3 = 25$ meV for $n = 0$ (black solid lines), $n = 1$ (red dotted lines), $n = 2$ (green dashed lines), and $n = 3$ (blue dot-dashed lines). The inset in (a) shows the coupling between the three layers while in (b) it shows an enlargement of the LLs crossings for low magnetic fields. The vertical arrows indicate some of the allowed optical transitions.

blue dot-dashed lines present the intraband transitions $(0, 1^+)$, $(1^+, 2^+)$ and $(2^+, 3^+)$ while the red dotted and blue dash-dash-dotted lines show the interband transitions $(1^-, 2^+)$ and $(2^-, 3^+)$, respectively. Here the sign "+"("−") stands for electron (hole) states. The transitions follow a $B^{3/2}$ dependence for low magnetic fields ($B < 3$ T) and this behavior turns into a linear B-dependence for higher values of the field ($B > 10$ T). Figure 47(b) shows the corresponding oscillator strength as a function of the magnetic field for the same transitions appearing in the left panel. All transitions show an oscillator strength that monotonically decreases with increasing magnetic field with the exception of the transition involving the zero LL (see inset of Fig. 47(b)). Notice that the OS associated with

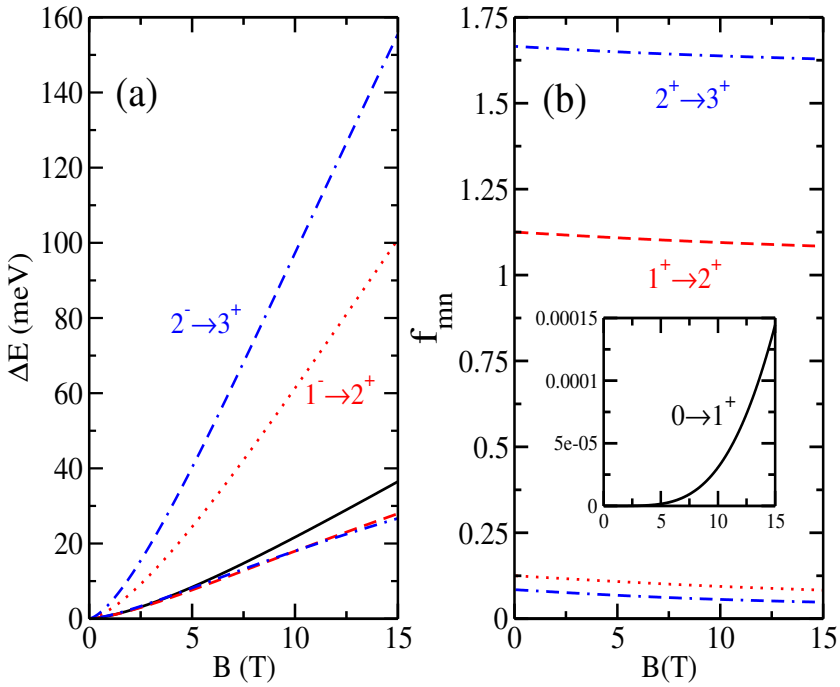

Figure 47: Left panel (a) shows the transition energies as a function of the magnetic field B for unbiased, i.e. $U_1 = U_2 = U_3 = 0$, ABC layers. The right panel (b) presents the oscillator strength of the allowed transitions for the low-lying energy Landau levels.

interband transitions are much smaller than those involving the intraband transitions.

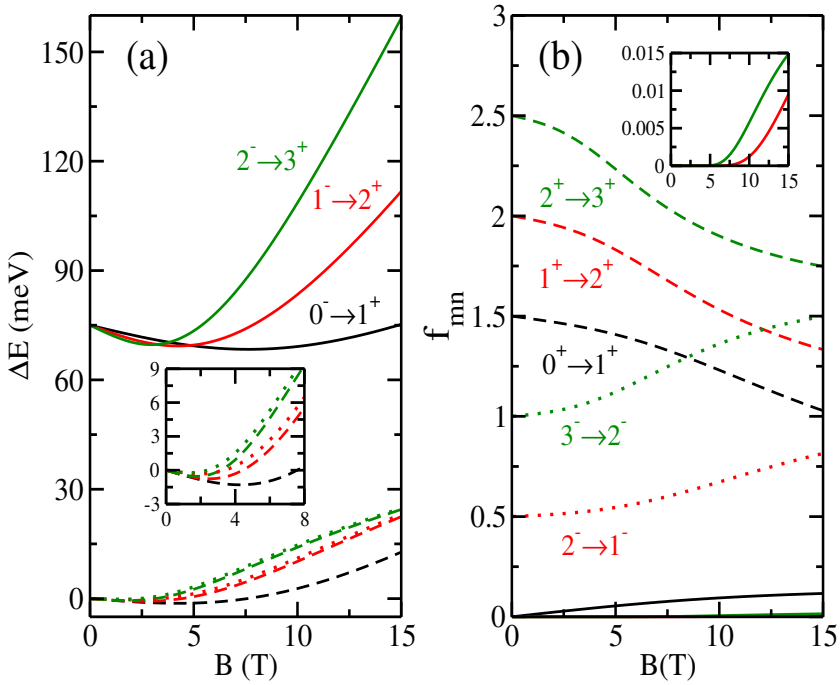

Figure 48: (a) Transition energies between the low-lying energy LL in a biased ABC TLG as a function of the magnetic field for $U_1 = 100$ meV, $U_2 = 50$ meV, $U_3 = 25$ meV. (b) Oscillator strength vs magnetic field B for the transitions presented in (a).

The effect of an applied bias is explored in Fig. 48, where we show the energy

transitions (a) and oscillator strength (b) as function of magnetic field for biased layers with $U_1 = 100$ meV, $U_2 = 50$ meV, $U_3 = 25$ meV. The small difference between the transition energies of the dashed and dotted red (green) lines reveals a clear asymmetry between electron and hole transitions. For low magnetic fields, the energies involved in the intraband electron transitions are slightly negative due to the crossing between the LLs shown in the inset of Fig. 46(b), which are also responsible for the crossings happening between the interband energy transitions (solid lines) in the left panel of Fig. 48. In contrast to the case with unbiased layers, now the OS show a stronger dependence on the magnetic field, and although the electron and hole have very similar intraband energy transitions, their OS are remarkable different and have the opposite magnetic field dependence. While the hole-like transitions $(2^-, 1^-)$, $(3^-, 2^-)$ gain in OS as the magnetic field increases, the electron-like transitions $(1^+, 2^+)$, $(2^+, 3^+)$ experience a considerable decrease in OS. The inset in Fig. 48(b) shows the very small OS of the transitions $(1^-, 2^+)$ and $(2^-, 3^+)$.

Figure 49 shows the TLG Landau-level spectrum as function of U_1 (with $U_2 = U_3 = 0$) (a) and U_3 (with $U_1 = U_2 = 0$) (b) for $n = 0$ (black solid lines), $n = 1$ (red dotted lines), $n = 2$ (green dashed lines), and $n = 3$ (blue dot-dashed lines) for a fixed magnetic field of 10 T. Among the differences between the panels (a) and (b) it can be noticed that the energies increase faster with U_3 and also for $n = 0$ we have that $E = U_3$ is always an eigenenergy, although $E = U_1$ is not. Figure 50 shows the transition energies between some of the levels appearing in Fig. 49. It also shows the behavior of the oscillator strength as U_1 (top left panel) and U_3 (top right panel) increase. The inset in top-right panel shows the transition $(0^+, 1^+)$ which has a very small OS as compared to the other ones. The legend for this graph is the same as in Fig. 48. The transition energies shown in the bottom panels are very similar, but when U_3 is increased the interband (intraband) transitions occur at slightly higher (lower) energies than when U_1 is increased. The difference in the role played by the top and bottom layers can be better noticed when we look at the oscillator strengths, which behave completely different whether we vary U_1 or U_3. Among the discrepancies, we can highlight the transition $(0^-, 1^+)$ (black solid line) that presents a small monotonic increase with U_1 and an accentuated decrease with U_3. It is also worth noticing the hole-like transitions $(2^-, 1^-)$ (red dotted line) and $(3^-, 2^-)$ (green dotted line), that monotonically decrease as U_1 increases, and show the opposite behavior as we increase U_3. On the other hand the electron-like transitions $(1^+, 2^+)$ (red dashed line) and $(2^+, 3^+)$ (green dashed line) decrease as U_3 is increased, while the increase of U_1 causes a gain in their OS.

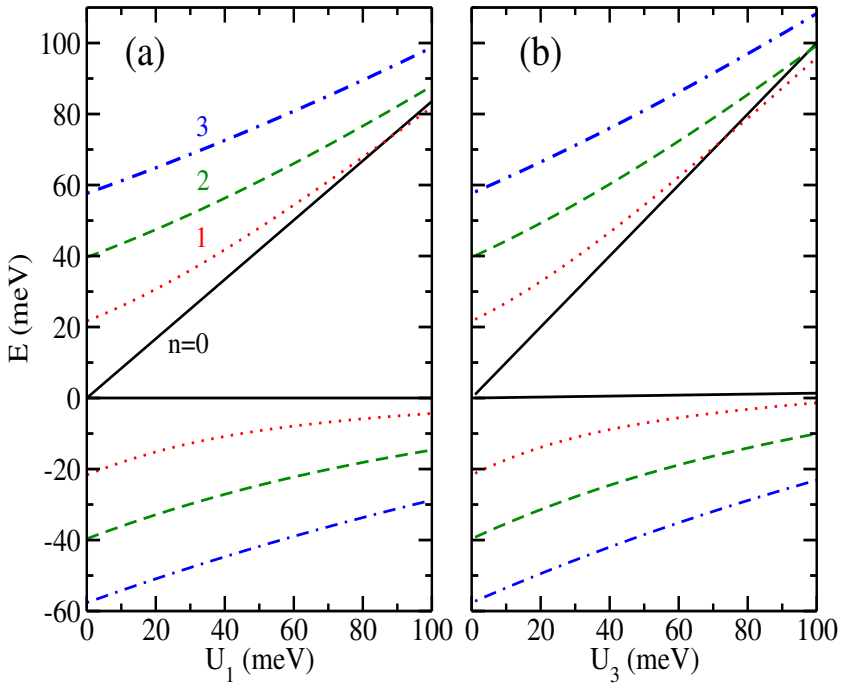

Figure 49: The TLG Landau-level spectrum with a fixed magnetic field of 10 T for the ABC stacking as a function of U_1 with $U_2 = U_3 = 0$ (a) and U_3 with $U_1 = U_2 = 0$ (b) for $n = 0$ (black solid lines), $n = 1$ (red dotted lines), $n = 2$ (green dashed lines), and $n = 3$ (blue dot-dashed lines).

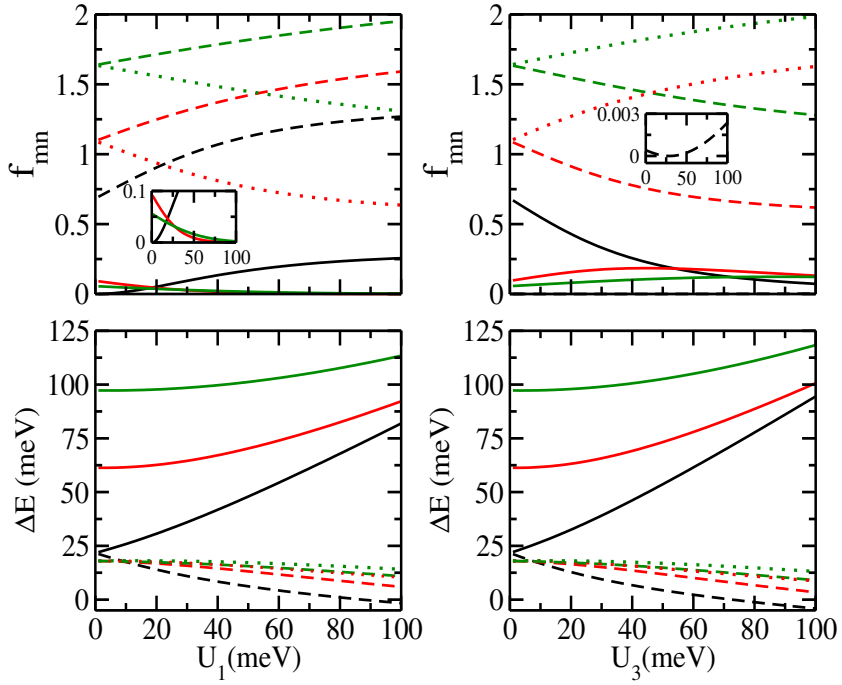

Figure 50: Energy transitions (bottom panels) and oscillator strength (top panels) as a function of U_1 and U_3 for fixed magnetic field of 10 T. The potential in the other two layers is kept zero. The inset in the top-left panel shows the transitions $(1^-, 2^+)$ (red solid line) and $(2^-, 3^+)$ (green solid line), while the inset in the top-right panel shows the transition $(0^+, 1^+)$ (black dashed line).

For completeness we also calculated the CR spectrum as:

$$\sigma(E) = \sum_{n,m} \frac{(\Gamma/2\pi)E_{mn}f_{mn}}{(E - E_{mn})^2 + \Gamma^2/4} f(E_n)[1 - f(E_m)], \tag{6.4}$$

where $E_{mn} = E_m - E_n$ is the transition energy, f_{mn} is the OS defined in Eq. (6.3), Γ is the broadening of the Lorentzian function, and $f(E_n)$ is the Fermi-Dirac distribution. In the numerical results we set the temperature equal to zero and $\Gamma = 2$ meV. The position of the Fermi level E_F is taken between the levels 0 (0^+) and 1^+ (1^+) for the unbiased (biased) case.

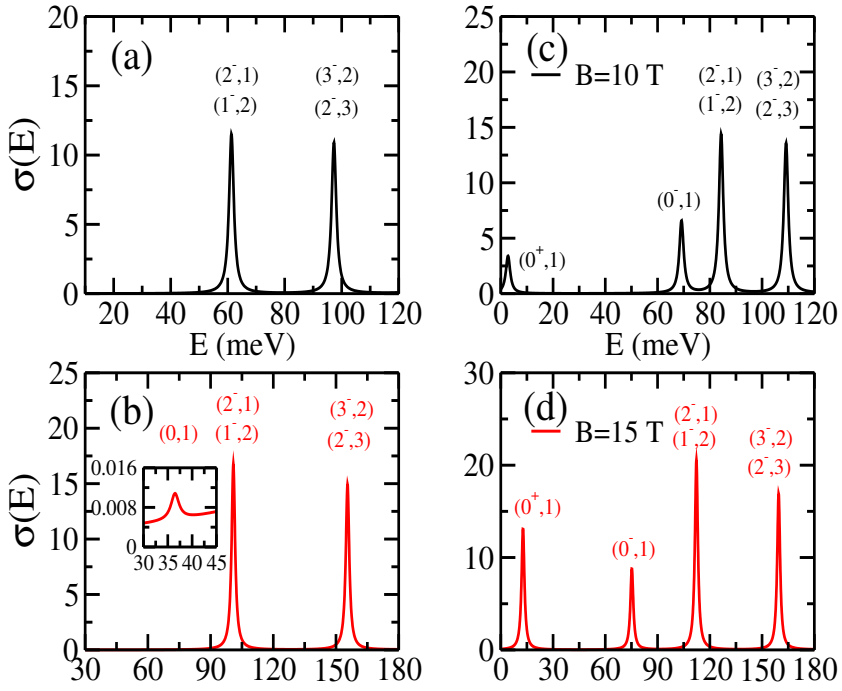

Figure 51: $\sigma(E)$ vs energy in ABC TLG for $B = 10$ T (black lines) and $B = 15$ T (red lines). The left (right) panels correspond to unbiased layers (biased). The inset shows the first absorption peak corresponding to the transition $(0, 1)$.

Figure 51 shows the optical absorption peaks for ABC TLG. Panels (a) and (b) correspond to the unbiased case for $B = 10$ T (black line) and $B = 15$ (red line) T, while the panels (c) and (d) present the absorption for biased layers, respectively. Notice in panel (a) the absence of the peak corresponding to the transition $(0, 1)$ (around $E = 22$ meV), which is caused by the small value of the OS of this transition (see Fig. 47(b)) that makes the contributions of the others transitions outgrow the absorption peak in this region of energy. In panel (b) this first transition peak is now present around 36.5 meV, although very small compared to the other absorption peaks. When a bias is applied we observe the presence of an extra peak due the lifting of the electron-hole degeneracy of the $n = 0$ LL.

6.2 ABA Stacking

Let us now turn our attention to the case of ABA stacking. The Hamiltonian for ABA-stacked TLG around the K point is given by

$$\mathcal{H}^{ABA} = \begin{pmatrix} U_1 & v_F\pi^\dagger & \gamma_1 & 0 & 0 & 0 \\ v_F\pi & U_1 & 0 & 0 & 0 & 0 \\ \gamma_1 & 0 & U_2 & v_F\pi & \gamma_1 & 0 \\ 0 & 0 & v_F\pi^\dagger & U_2 & 0 & 0 \\ 0 & 0 & \gamma_1 & 0 & U_3 & v_F\pi^\dagger \\ 0 & 0 & 0 & 0 & v_F\pi & U_3 \end{pmatrix}. \tag{6.5}$$

In the presence of a magnetic field the six-component spinor of the n^{th} LL is given by $\Psi_n^{ABA} = B_n \left[-il_B\delta_1^n\psi_{n-1},\ \ \psi_n,\ \ ib_1^n\psi_{n-1},\ \ \frac{2(n-1)b_1^n}{l_B\delta_2^n}\psi_{n-2}, \frac{-il_B\delta_3^n b_1^n}{b_3^n}\psi_{n-1},\ \ \frac{b_1^n}{b_3^n}\psi_n\right]^T$ for $n > 0$, where $b_{1(3)}^n$ are given in Appendix A. It is worth highlighting that in the case of unbiased layers the LLs are simply the superposition of the monolayer and bilayer spectrum, and the spinor components that correspond to the third layer are identical to the ones of the first layer, as it should be since the top and bottom layers are then symmetric relative to the middle layer. For this reason, we will refer now to the Landau index no longer as n, but as $n_m = n$ for the monolayer-like levels and as $n_b = n - 1$ for the bilayer-like levels. The case $n_m = 0$ generates two LL, as can be seen in Fig. 52, the level we call 0^+ corresponds to $E_0 = U_1$ and for the level 0^-, $E_0 = U_3$. The spinor associated to these zero levels are $\Psi_{0^+}^{ABA} = 1/(l_B\sqrt{\pi})^{1/2}\,[0,\ \ \psi_0,\ \ 0,\ \ 0,\ \ 0,\ \ 0]$ and $\Psi_{0^-}^{ABA} = 1/(l_B\sqrt{\pi})^{1/2}\,[0,\ \ 0,\ \ 0,\ \ 0,\ \ 0,\ \ \psi_0]$, respectively. While $n_b = 0$ ($n = 1$) produces $E_1 = U_2$ and a level starting from $E_1 = (U_1 + U_3)/2$ that presents a small monotonic decrease with B.

The oscillator strength was calculated according to Eq. (6.3) and the explicit expressions for the ABA stacking are given in Appendix A. Figure 53(a) shows the energies of some possible transitions between monolayer-like levels of the unbiased layers. All these transitions occur at energies that follow a $\sqrt{B}$ dependence. The oscillator strengths related to these transitions are presented in Fig. 53(b), where we can see that the transition involving the zero energy level is the most pronounced one, and the interband transitions are very small (see inset of Fig. 53(b)). Figure 54 presents the same kind of results, but now for transitions between levels characteristic of the bilayer system. These transition energies are linear in B for low values of the magnetic field ($B < 5$ T), however, as B increases the linear behavior turns into a $\sqrt{B}$-dependence. The OS of the bilayer-like

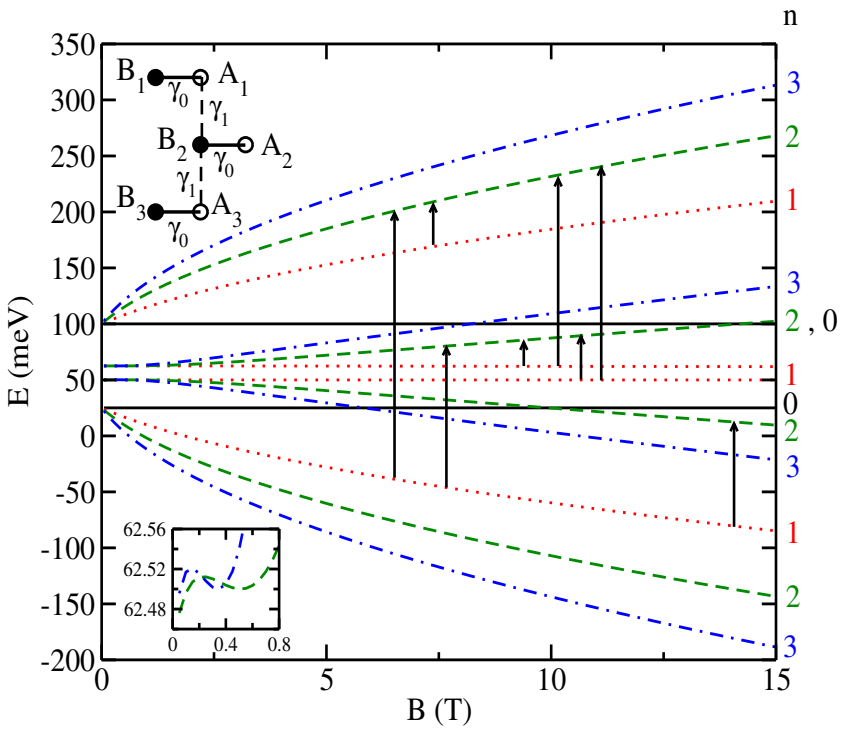

Figure 52: The ABA TLG Landau-level spectrum as a function of B with $U_1 = 100$ meV, $U_2 = 50$ meV, $U_3 = 25$ meV for $n = 0$ (black solid lines), $n = 1$ (red dotted lines), $n = 2$ (green dashed lines), and $n = 3$ (blue dot-dashed lines). The upper inset shows the coupling between the layers and the lower inset shows an enlargment of the non-linear behavior of the levels $n_b = 1^+, 2^+$ for low B.

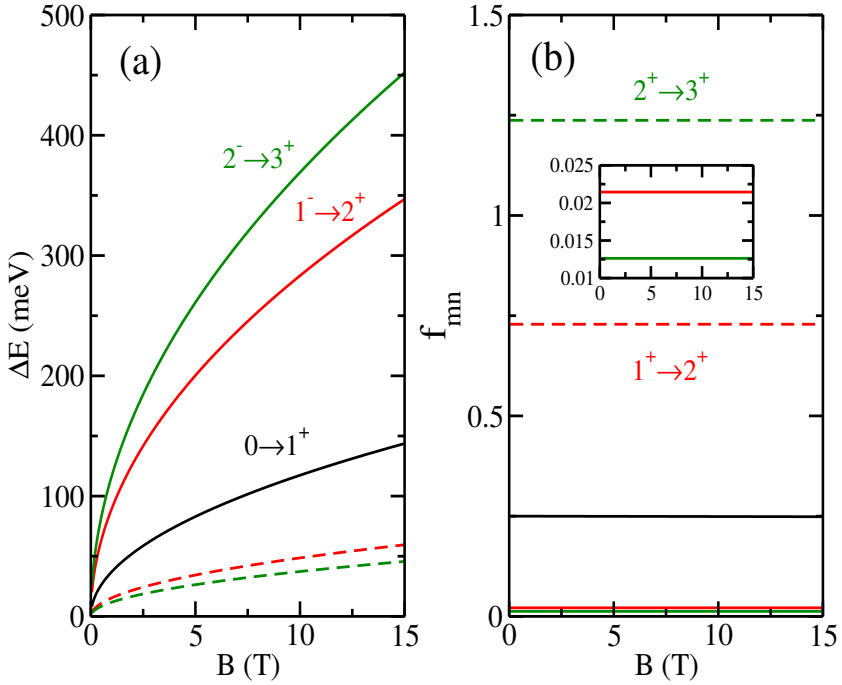

Figure 53: (a) The transition energies between monolayer-like levels as a function of the magnetic field B for unbiased, $U_1 = U_2 = U_3 = 0$, ABA layers. (b) The corresponding oscillator strengths are shown in the left panel.

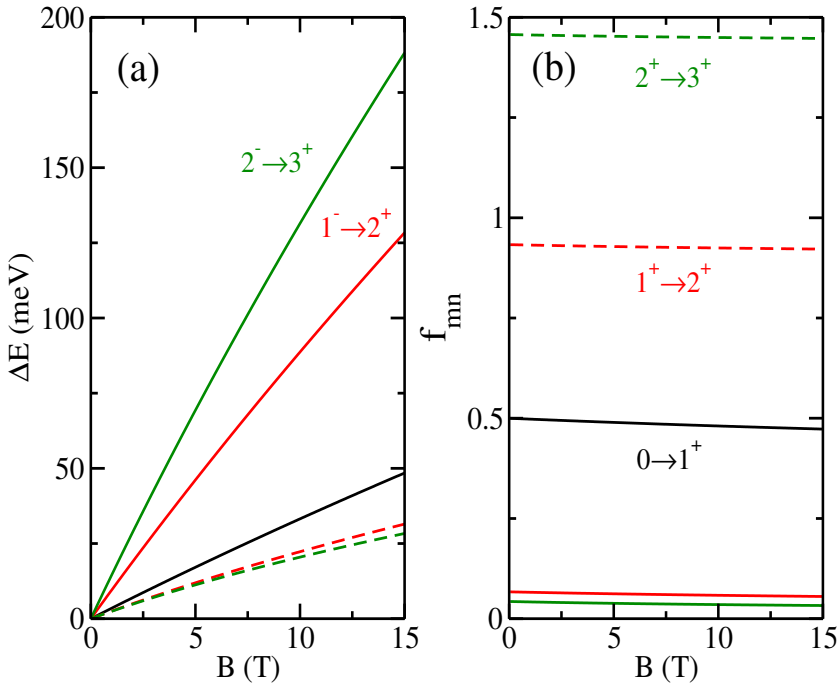

Figure 54: (a) The transition energies between bilayer-like levels as a function of the magnetic field B for unbiased, $U_1 = U_2 = U_3 = 0$, ABA layers. (b) The oscillator strength for the transitions showed in the left panel.

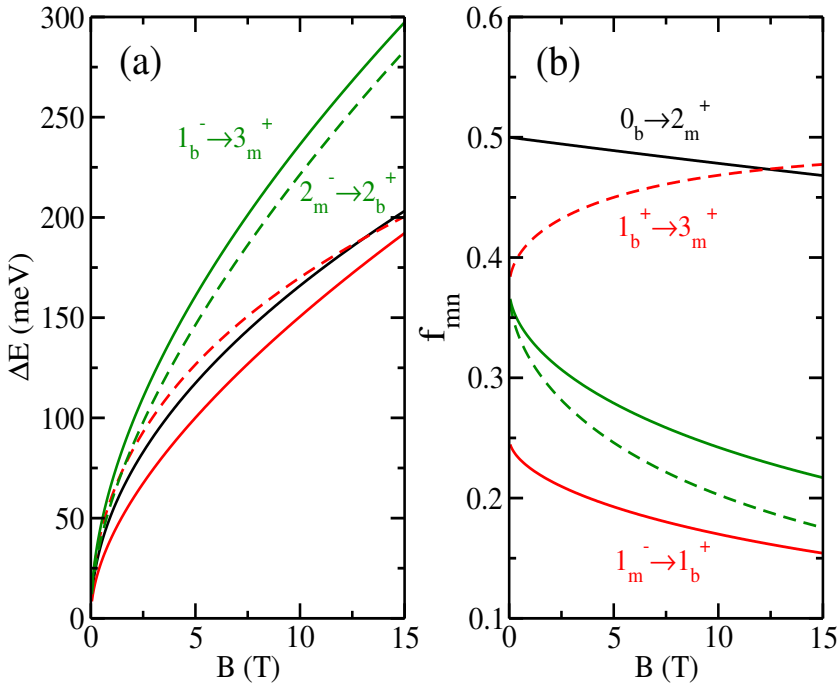

Figure 55: (a) The transition energies between monolayer-like and bilayer-like levels as a function of the magnetic field B for unbiased, $U_1 = U_2 = U_3 = 0$, ABA layers. (b) The oscillator strength for the transitions showed in the left panel.

transitions present all the same kind of behavior, i.e. a weak monotonic decrease as B increases.

In Fig. 55 the transitions between monolayer-like and bilayer-like levels are presented. The transition energy $(n_b = 0, n_m = 2^+)$, black solid curve, follows a perfect $\sqrt{B}$ dependence, since the level $n_b = 0$ is simply $E = 0$. The energies correspond to the transition $(n_m = 1^-, n_b = 1^+)$, red solid line, $(n_b = 1^-, n_m = 3^+)$, green solid line, and $(n_m = 2^-, n_b = 2^+)$, green dashed line, can be well fitted by a power law with an exponent that varies from 0.5 (low fields) to 0.6 (high fields) as B increases. The transition $(n_b = 1^+, n_m = 3^+)$ can be also fairly approximated by a power law, but in this case the exponent varies from 0.4 to 0.5 as the magnetic field increases. The OS are shown in panel (b) where we can see that all OS decrease with increasing B with the exception of the intraband transition $(n_b = 1^+, n_m = 3^+)$, red dashed line, which exhibits the opposite behavior.

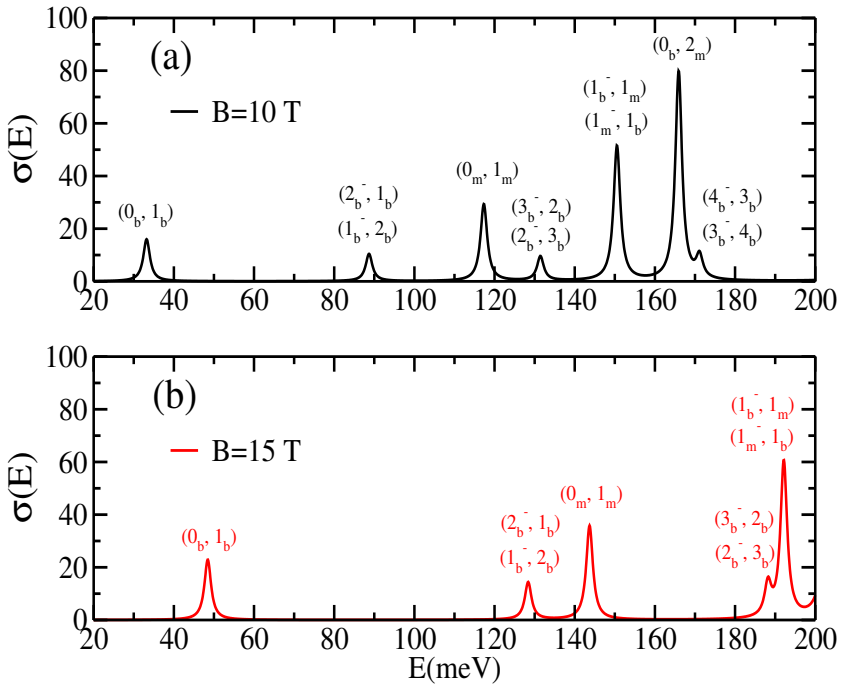

Figure 56: $\sigma(E)$ vs energy in an unbiased ABA TLG for $B = 10$ T (black lines) and $B = 15$ T (red lines).

The CR absorption peaks of an unbiased ABA TLG are displayed in Fig. 56 for $B = 10$ T (panel (a)) and $B = 15$ T (panel (b)). The Fermi energy is taken to be $E = 0$. Above each peak it is shown which transitions are involved. We can notice that with the exception of the peaks associated to transitions involving the level $E = 0$ each peak receives equal contributions of two interband transitions. It means that if, for instance, the Fermi level is increased in order to cross the level $n_b = 1^+$, the first and third peaks will disappear, the second and fifth peaks will drop to half of their values and the other ones will be unaffected.

The following results consider the effect of a bias ($U_1 = 100$ meV, $U_2 = 50$ meV and $U_3 = 25$ meV) that breaks the mirror reflection symmetry of the ABA TLG. Figure 57(a) shows some of the transitions between the monolayer-like levels. We see two groups of transition energies: the intraband transitons (dashed and dotted lines starting from $E = 0$) and interband transitions (solid lines starting from $E = 75$ meV). The inset displays the small asymmetry between the electron-like ($n_m = 0^+, n_m = 1^+$) and hole-like ($n_m = 1^-, n_m = 0^-$) transitions due to the bias. In general the transition energies increase less fast with B when a bias is applied. In panel (b) we notice that the OS of all the intraband transitions have the same decreasing behavior as B increases, exibiting a more strong dependence on B up to 5 T. Remarkably, the OS of the interband transitions exhibit the opposite behavior, i.e. a small monotonically increasing behavior with B. The upper inset displays an enlarged view of the OS for the transitions ($n_m = 1^-, n_m = 2^+$) and ($n_m = 2^-, n_m = 3^+$).

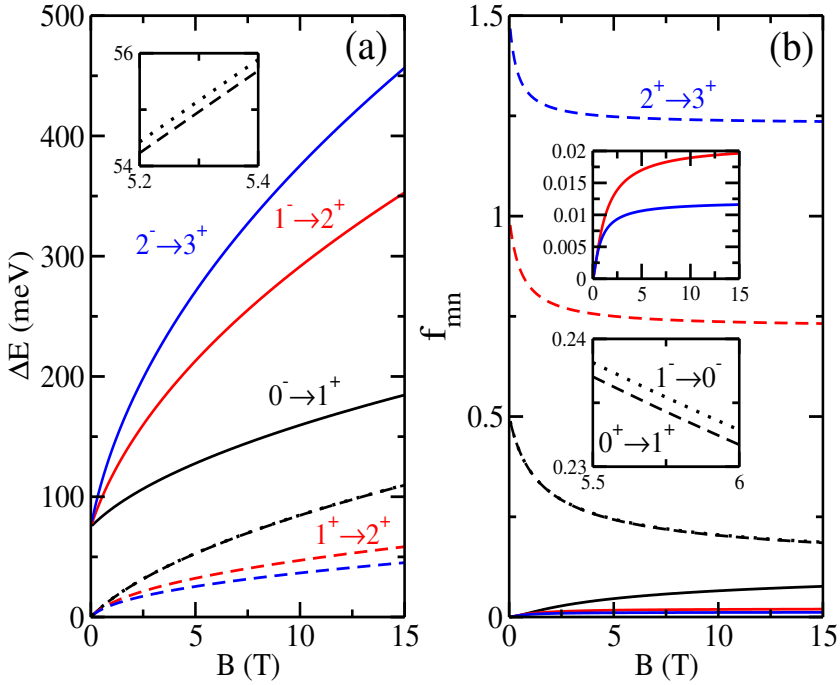

Figure 57: (a) The transition energies between monolayer-like levels as a function of the magnetic field B for biased ABA layers. The inset shows the small difference in energy of the electron and hole-like transitions. (b) The oscillator strength for the transitions showed in the left panel. The lower inset shows the small difference in OS of the transitions ($n_m = 0^+, n_m = 1^+$) and ($n_m = 1^-, n_m = 0^-$), while the upper inset shows an enlargement of the ($n_m = 1^-, n_m = 2^+$) and ($n_m = 2^-, n_m = 3^+$).

Figure 58 focus on the transitions between bilayer-like levels. The main effect of the bias on the transition energies is the disappearance of the linear behavior for small values of B (see the inset of Fig. 52) and the breaking of the symmetry between electrons and

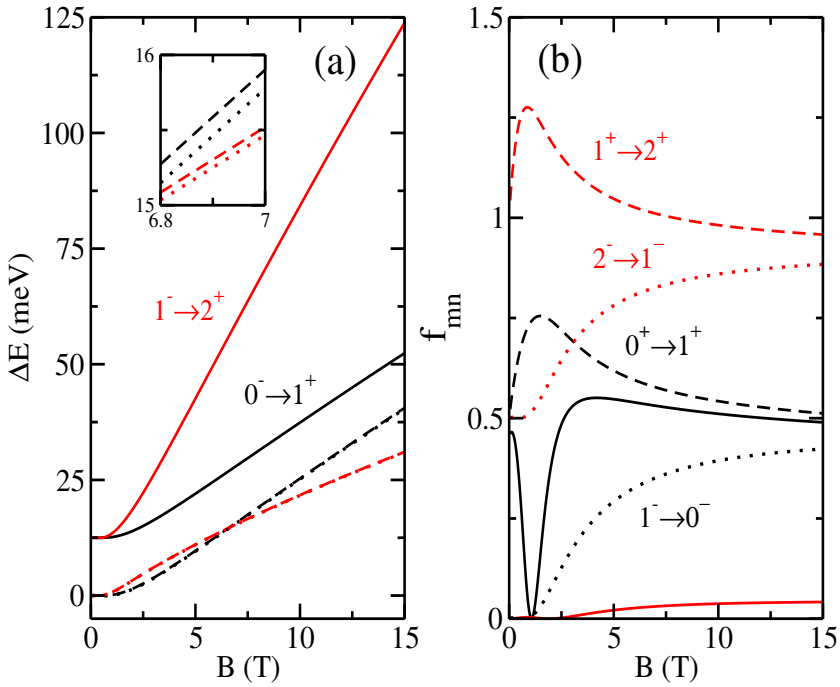

Figure 58: (a) The transition energies between bilayer-like levels as a function of the magnetic field B for biased ABA layers. The inset shows the small difference in energy of the electron and hole-like transitions. (b) The oscillator strength for the transitions are shown in the left panel.

holes, as shown in the inset of panel (a). In panel (b) we see that for all the transitions, with the exception of $(n_b = 1^-, n_b = 2^+)$, the OS exhibit a strong dependence on B, specially for low fields. The OS for the hole-like transitons have a strong increase up to 5 T and then they continue to increase but now less fast, while for the electron-like transitions the OS presents a significant increase for small values of B with a subsequent decrease.

Figure 59 exhibits some transitions from monolayer to bilayer-like levels. The energy of the transition $(n_m = 0^-, n_b = 0^-)$ is 25 meV and constant while its, OS exhibits a strong magnetic field dependence (panel (b)) due to the magnetic length l_B appearing in the constants of Appendix A. The other two intraband transition energies (red and blue solid curves) can be well fitted by a power law whose exponent approaches 0.3 and the oscillator strengths of these transitions are very small as shown in the inset of panel (b). The interband transitions $(n_m = 1^-, n_b = 1^+)$, red dashed line, and $(n_m = 2^-, n_b = 2^+)$, blue dashed line, have energies that can be described by a $B^{0.6}$ dependence for $B > 5$ T and their OS have a small increase for low values of magnetic field followed by a monotonic decrease as can be seen in panel (b). In Fig. 60 we present the same kind of results for some transitions from bilayer to monolayer-like levels. Note that in this case, with the exception of the intraband transition $(n_b = 0^+, n_m = 0^+)$, all the transitions have low

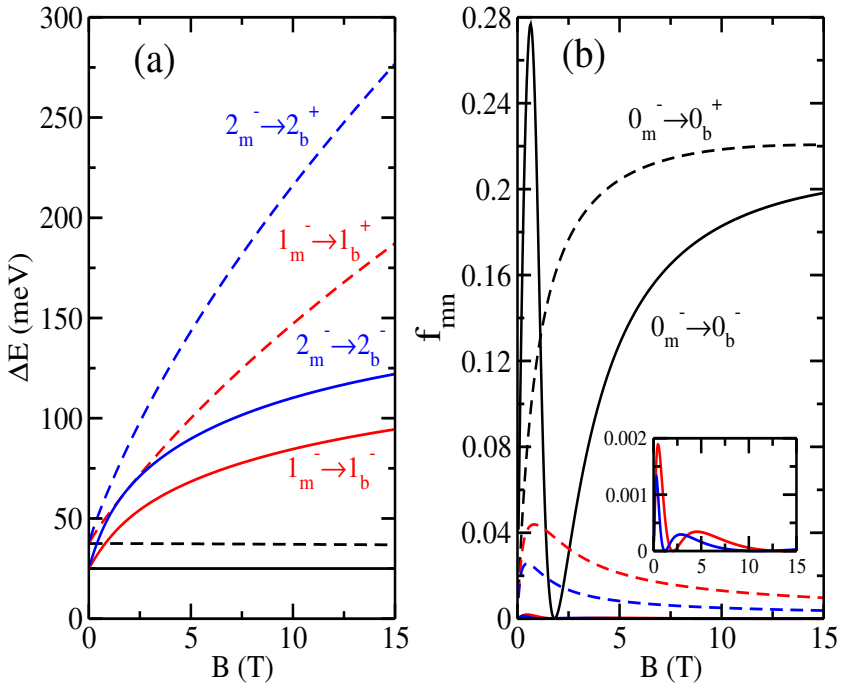

Figure 59: (a) Transition energies from monolayer to bilayer-like levels as a function of the magnetic field B for biased ABA layers. (b) The oscillator strength for the transitions showed in the left panel. The inset shows the OS of the transitions $(n_m = 1^-, n_b = 1^-)$ in red solid line and $(n_m = 2^-, n_b = 2^-)$ in blue solid line.

oscillator strengths for fields higher than 3 T.

Figure 61 shows the CR spectrum for the biased ABA layers for $B = 10$ T (panel (a)) and $B = 15$ T (panel (b)). We assumed that all levels are occupied until 0_b^+. This result summarizes the main effects of the bias on the transitions between the LL, since it takes into account both, transition energies and oscillator strength. We observe more CR lines at low energies due to the lifting of the four-fold degeneracy (without taking into account spin and valley degeneracy) of the level 0. The asymmetry between elctrons and holes induced by the bias are usually small, which makes, for instance, the transitions $(n_b = 2^-, n_b = 1^+)$ and $(n_b = 1^-, n_b = 2^+)$ appear as a single CR line, since the difference in energy of these transitions are smaller than the broadening Γ of the peaks. The only evidence of this kind of asymmetry in the CR spectrum is given by the transitions $(n_m = 1^-, n_b = 1^+)$ and $(n_b = 1^-, n_m = 1^+)$ which occur at 147.14 meV and 159.69 meV for $B = 10$ T, respectively. The inset in panel (a) shows an enlargement of the CR line corresponding to $(n_b = 0^-, n_m = 2^+)$ around 181.5 meV. Note also that the transition $(n_b = 0^+, n_m = 2^+)$ is not visible since its OS is very small (see inset in Fig. 15 (b)). In panel (b) it can be seen that the first three peaks in panel (a) become two double peaks, since the energies of the transitions $(n_b = 0^+, n_m = 0^+)$ and $(n_b = 0^-, n_m = 0^+)$ do not change, and the energies of $(n_b = 0^+, n_b = 1^+)$ and $(n_b = 0^-, n_b = 1^+)$ increase. A similar behavior occurs

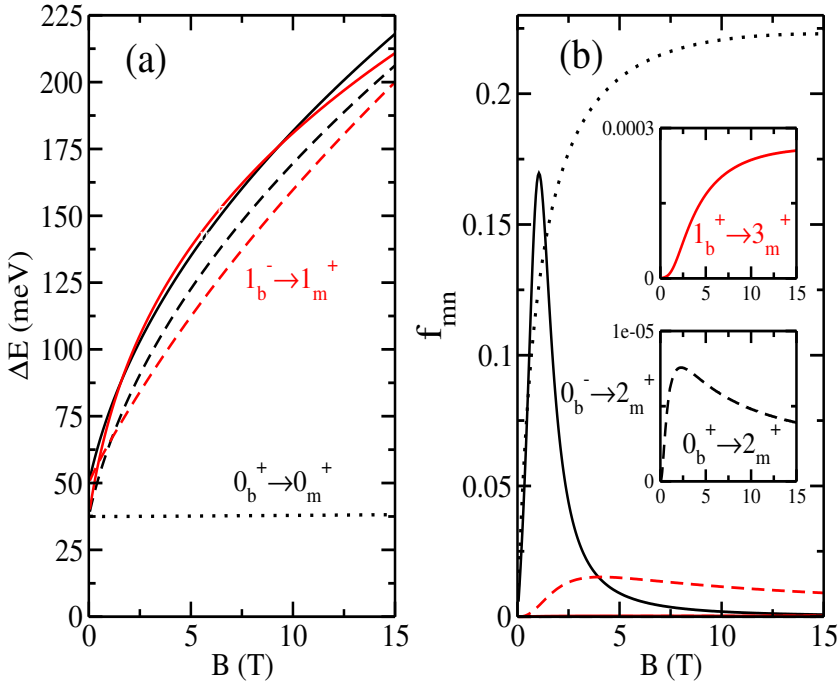

Figure 60: (a) Energies of some of the transitions from bilayer to monolayer-like levels as a function of the magnetic field B for biased ABA layers. (b) The oscillator strength for the transitions showed in the left panel. The lower inset displays the OS of the transition $(n_b = 0^+, n_m = 2^+)$ in black dashed line, while the upper inset displays the transitions $(n_b = 1^-, n_m = 3^+)$ and $(n_b = 1^+, n_m = 3^+)$.

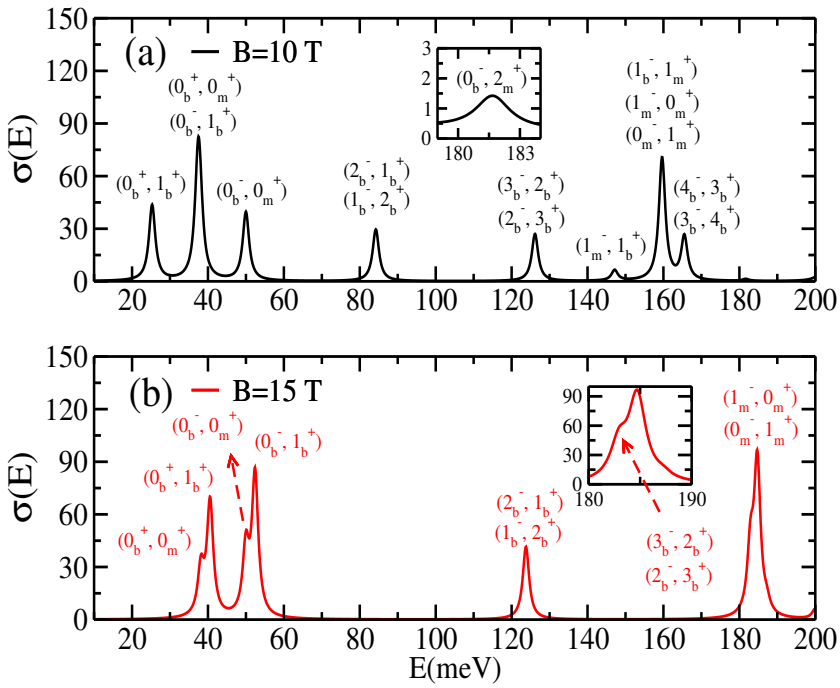

Figure 61: $\sigma(E)$ vs energy in a biased ABA ($U_1 = 100$ meV, $U_2 = 50$ meV, $U_3 = 25$ meV) TLG for $B = 10$ T (black lines) and $B = 15$ T (red lines). The inset in (a) shows an enlargement of the transition occurring around 181.5 meV, while the inset panel (b) shows the formation of a double peak around 183 meV and 184.8 meV.

around 185 meV, the transition energies of $(n_b = 2^-, n_b = 3^+)$ and $(n_b = 3^-, n_b = 2^+)$ increase faster than the energies of $(n_m = 1^-, n_m = 0^+)$ and $(n_m = 0^-, n_m = 1^+)$ leading to the formation of the double peak shown in the inset.

7 Conclusions and Perspectives

In this thesis we theoretically study the basic electronic properties of carbon nanoribbons and trilayers graphene.

In the first chapter we started by introducing the carbon atom and its hybridizations, followed by a brief review on the carbon materials discovered along the last three decades, such as fullerenes, carbon nanotubes and graphene. Then, in the last part of the chapter, we focused on graphene fabrication techniques and some electronic properties that make this material an interesting research subject.

Along the second chapter we developed the mathematical framework that helps to explain the basic electronic properties of graphene. More precisely, we presented the tight-binding model applied to graphene and performed the continuum limit approximation in order to obtain an effective Hamiltonian valid for a low density of carriers, which allows the analogy with quantum electrodynamics. The formation of the Landau levels as a result of an applied external magnetic field was also analyzed.

In chapter 3, we turned our attention to graphene nanoribbons, where we investigated, by means of tight-binding model, how simple shear strain modifies the electronic spectrum of graphene and carbon nanoribbons with zigzag and armchair edges. The effect of the strain in zigzag ribbons with an even number of atom lines is to open a gap in the spectrum, which can be controlled by changing the extension of the deformation δ. The armchair nanoribbons that were initially semiconductors, become metallic when the strain is applied.

In chapter 4, we showed how to mathematically treat the stacking of two and three layers of graphene, describing the tight-binding parameters responsible for coupling the layers. The free electron spectra, as well as the LLs are presented for bilayer graphene. Concerning to trilayer graphene, we focused on the effect of the two stacking orders on the free electron spectrum, and the role played by the interlayer asymmetries as well.

In chapter 5, we obtained exact analytical expressions for the Landau-level spectra

of trilayer graphene, within a model that took into account the layer asymmetry induced by different electrostatic potentials in each layer. The expressions were obtained for both the Bernal (ABA) and rhombohedral (ABC) stackings, which were found to display quite distinct behaviors. As shown in previous work [92] the Landau-level spectrum for the ABA case in the absence of electrostatic bias between the layers shows both a monolayer-like as well as bilayer-like character, indicated by the different magnetic field dependence of the spectrum. The addition of a potential difference between the layers shifts the spectrum and creates a tunable gap between the electron and hole states, the size of this energy gap being different for the monolayer and the bilayer energy levels. Level crossings between the monolayer and bilayer Landau levels are found for certain values of the magnetic field. For the ABC case, the Landau levels have a magnetic field dependence which, in the absence of bias, has a $B^{3/2}$ dependence for low energies [71]. For stronger magnetic fields the Landau levels exhibit a linear B dependence. The introduction of electrostatic bias in the system lifts the degeneracy of the $n = 0$ levels and creates a tunable gap. The results show also the existence of level crossings at small magnetic fields. This model can be refined by taking into account second-nearest neighbor terms, as well as remote coupling between the lowest and uppermost layers.

Finally, in chapter 6 we made use of the continuum approximation to describe the TLG with both, ABA (Bernal) and ABC (rhombohedral), stacking sequences by a 6×6 Hamiltonian in which we use the Peierls sustitution together with the Landau gauge to include an external magnetic field. Using this approach we were able to find analytical expressions for the six-components spinor that we use to calculate, within the dipole approximation, the oscillator strengths of the transitions between the Landau levels. We also calculated the cyclotron resonance spectrum for neutral and biased layers. In summary the effect of an applied bias on the transitions between the LL are three: reduction of the transition energies, lift of the degeneracy of the level $n = 0$ (two-fold degeneracy in ABC TLG and four-fold degeneracy in ABA TLG), and the break of the electron-hole symmetry. The first and second effects are easily observed in the CR spectrum for both types of stacking: reduction of transition energies causes a shift of the peaks and the lifting of the degeneracy appears as extra peaks. Although the asymmetry between electrons and holes has a considerable influence on the OS of the transitions, the difference in the transition energies are rather small, usually smaller than the broadening of CR peaks, which makes difficult to see this asymmetry in the CR spectrum, with the exception of the transitions $(n_m = 1^-, n_b = 1^+)$ and $(n_b = 1^-, n_m = 1^+)$ in ABA TLG which occur at very distinguished energies.

As a short-term perspective we intend to investigate the effect of an external magnetic field, acting together with the simple shear strain, on the energy bands of carbon nanoribbons. Concernig TLG, we are interested to look for what is called topological confined states. In 2008 *Ivar Martin et al.* found two branches of states inside the gap of a biased bilayer graphene. Each one of these states appear to be localized on the domain walls separating insulating regions experiencing the opposite gating polarity [103]. Since trilayers having ABC stacking behave similarly to bilayers when subjected to a gate voltage, we believe these kind of confined states can be also found in TLG, but in this case, instead of two branches we expect to find three energy modes.

APPENDIX A

The constants appearing in Ψ_n^{ABC} are given by:

$$b_n \equiv \frac{1}{\gamma_1'}\left(\delta_3^n - \frac{2n}{{l_B}^2\delta_3^n}\right), \tag{A.1a}$$

$$c_n \equiv \frac{l_B}{2(n+1)}\left(\delta_2^n b_n - \gamma_1'\right), \tag{A.1b}$$

$$d_n \equiv \frac{1}{\gamma_1'}\left(\delta_2^n c_n - \frac{b_n}{l_B}\right), \tag{A.1c}$$

$$A_n \equiv \left(\frac{1}{\sqrt{\pi} l_B g_n}\right)^{1/2}, \tag{A.1d}$$

$$\begin{aligned} g_n \equiv & 2^n n!\left(1+{b_n}^2\right) + 2^{n+1}(n+1)!\left({c_n}^2+{d_n}^2\right) + \\ & 2^{n+2}(n+2)!\frac{{d_n}^2}{\delta_1^{n\,2}{l_B}^2} + 2^{n-1}(n-1)!\frac{4n^2}{\delta_3^{n\,2}{l_B}^2}, \end{aligned} \tag{A.1e}$$

where $\gamma_1' = \gamma_1/(\hbar v_F)$.

The integrals involved in the calculation of the oscillator strength for ABC TLG are given by

$$\int {\Psi_{A_1}^m}^* \bar{x} \Psi_{A_1}^n d\bar{x} = \sqrt{\pi} 2^{m+1}(m+1)! \frac{d_m d_n A_m A_n}{2}\left\{2(m+2)\delta_{m+2,n+1} + \delta_{m,n+1}\right\}, \tag{A.2a}$$

$$\int {\Psi_{B_1}^m}^* \bar{x} \Psi_{B_1}^n d\bar{x} = \sqrt{\pi} 2^{m+2}(m+2)! \frac{d_m d_n A_m A_n}{2\delta_1^m \delta_1^n {l_B}^2}\left\{2(m+3)\delta_{m+3,n+2} + \delta_{m+1,n+2}\right\}, \tag{A.2b}$$

$$\int {\Psi_{B_2}^m}^* \bar{x} \Psi_{B_2}^n d\bar{x} = \sqrt{\pi} 2^{m+1}(m+1)! \frac{c_m c_n A_m A_n}{2}\left\{2(m+2)\delta_{m+2,n+1} + \delta_{m,n+1}\right\}, \tag{A.2c}$$

$$\int {\Psi_{A_2}^m}^* \bar{x} \Psi_{A_2}^n d\bar{x} = \sqrt{\pi} 2^{m} m! \frac{b_m b_n A_m A_n}{2}\left\{2(m+1)\delta_{m+1,n} + \delta_{m-1,n}\right\}, \tag{A.2d}$$

$$\int {\Psi_{A_3}^m}^* \bar{x} \Psi_{A_3}^n d\bar{x} = \sqrt{\pi} 2^{m-1}(m-1)! \frac{2mn A_m A_n}{\delta_3^m \delta_3^n {l_B}^2}\left\{2m\delta_{m,n-1} + \delta_{m-2,n-1}\right\}, \tag{A.2e}$$

$$\int {\Psi_{B_3}^m}^* \bar{x} \Psi_{B_3}^n d\bar{x} = \sqrt{\pi} 2^{m} m! \frac{A_m A_n}{2}\left\{2(m+1)\delta_{m+1,n} + \delta_{m-1,n}\right\}, \tag{A.2f}$$

where m and n are Landau level indices for the different eigenstates. The selection rule is as usual $|m-n| = 1$. The result of Eq. (A.2e) is for $m, n > 0$, otherwise this integral is zero.

The constants appearing in Ψ_n^{ABA} are given by:

$$b_{1(3)}^n \equiv \frac{1}{\gamma_1'}\left(\frac{2n}{l_B} - l_B {\delta_{1(3)}^n}^2\right), \tag{A.3a}$$

$$B_n \equiv \left(\frac{1}{\sqrt{\pi} l_B g_n}\right)^{1/2}, \tag{A.3b}$$

$$\begin{aligned} g_n \equiv & 2^{n-2}(n-2)! \frac{4(n-1)^2 b_1^{n2}}{\delta_2^{n2} {l_B}^2} + 2^{n-1}(n-1)! \\ & + 2^{n-1}(n-1)!\left({l_B}^2 \delta_1^{n2} + b_1^{n2} + {l_B}^2 \delta_3^{n2}\left(\frac{b_1^n}{b_3^n}\right)^2\right) \qquad \text{(A.3c)} \\ & + 2^n n!\left(1 + \left(\frac{b_1^n}{b_3^n}\right)^2\right). \qquad \text{(A.3d)} \end{aligned}$$

The integrals needed to calculate the oscillator strength of the transitions are the following

$$\int {\Psi_{A_1}^m}^* \bar{x} \Psi_{A_1}^n d\bar{x} = \sqrt{\pi} 2^{m-1}(m-1)! \frac{\delta_1^m \delta_1^n B_m B_n}{2} \left\{2m\delta_{m,n-1} + \delta_{m-2,n-1}\right\}, \tag{A.4a}$$

$$\int {\Psi_{B_1}^m}^* \bar{x} \Psi_{B_1}^n d\bar{x} = \sqrt{\pi} 2^m m! \frac{B_m B_n}{2} \left\{2(m+1)\delta_{m+1,n} + \delta_{m-1,n}\right\}, \tag{A.4b}$$

$$\int {\Psi_{B_2}^m}^* \bar{x} \Psi_{B_2}^n d\bar{x} = \sqrt{\pi} 2^{m-1}(m-1)! \frac{b_1^m b_1^n B_m B_n}{2} \left\{2m\delta_{m,n-1} + \delta_{m-2,n-1}\right\}, \tag{A.4c}$$

$$\int {\Psi_{A_2}^m}^* \bar{x} \Psi_{A_2}^n d\bar{x} = \sqrt{\pi} 2^{m-2}(m-2)! \frac{2 b_1^m b_1^n B_m B_n (m-1)(n-1)}{{l_B}^2 \delta_2^m \delta_2^n} \left\{2(m-1)\delta_{m-1,n-2} + \delta_{m-3,n-2}\right\}, \tag{A.4d}$$

$$\int {\Psi_{A_3}^m}^* \bar{x} \Psi_{A_3}^n d\bar{x} = \sqrt{\pi} 2^{m-1}(m-1)! \frac{{l_B}^2 \delta_3^m \delta_3^n b_1^m b_1^n B_m B_n}{2 b_3^m b_3^n} \left\{2m\delta_{m,n-1} + \delta_{m-2,n-1}\right\}, \tag{A.4e}$$

$$\int {\Psi_{B_3}^m}^* \bar{x} \Psi_{B_3}^n d\bar{x} = \sqrt{\pi} 2^m m! \frac{b_1^m b_1^n B_m B_n}{2 b_3^m b_3^n} \left\{2(m+1)\delta_{m+1,n} + \delta_{m-1,n}\right\}. \tag{A.4f}$$

Equations (A.4a), (A.4c) and (A.4e) are valid for $m, n > 0$, while 9(d) is valid only for $m, n > 1$, otherwise these integrals are zero.

APPENDIX B – Publications related to this thesis

- S. H. R. Sena, J. M. Pereira Jr., G. A. Farias, and F. M. Peeters, *Landau levels in asymmetric graphene trilayers*, Phys. Rev. B **84**, 205448 (2011).
- S. H. R. Sena, J. M. Pereira Jr., G. A. Farias, and F. M. Peeters, *Cyclotron resonance of trilayer graphene*, Phys. Rev. B **86**, 085412 (2012).
- S. H. R. Sena, J. M. Pereira Jr., G. A. Farias, F. M. Peeters, and R. N. Costa Filho, *The electronic properties of graphene and graphene ribbons under simple shear strain*, Journal of Physics: Condensed. Matter **24**, 375301 (2012).

APPENDIX A – Publications related to this thesis

- S. H. R. Sena, J. M. Pereira Jr., G. A. Farias, and F. M. Peeters, *Landau levels in asymmetric graphene trilayers*, Phys. Rev. B **84**, 205448 (2011).
- S. H. R. Sena, J. M. Pereira Jr., G. A. Farias, and F. M. Peeters, *Cyclotron resonance of trilayer graphene*, Phys. Rev. B **86**, 085412 (2012).
- S. H. R. Sena, J. M. Pereira Jr., G. A. Farias, F. M. Peeters, and R. N. Costa Filho, *The electronic properties of graphene and graphene ribbons under simple shear strain*, Journal of Physics: Condensed. Matter **24**, 375301 (2012).

References

[1] M. Karplus and R. N. Porter, Atoms and Molecules: An Introduction For Students of Physical Chemistry (Benjamin, New York 1970).

[2] A. A. Radzig, B. M. Smirnov, Reference Data on Atoms, Molecules and Ions (Springer, Berlin 1985).

[3] C. Cohen-Tannoudji, B. Diu, and F. Laloë, Quantum Mechanics, Vol. 1 (Hermann and John Wiley & Sons, Paris 1997).

[4] C. A. Coulson, Valence (Oxford University Press, London 1953).

[5] R. Saito, G. Dresselhaus, and M.S. Dresselhaus, Physical Properties of Carbon Nanotubes (Imperial College Press, London 1998).

[6] E. C. Girão, Electronic and transport properties of carbon nanostructures. Doctoral thesis − Departamento de Física, Universidade Federal do Ceará, Fortaleza 2011.

[7] Hugh O. Pierson, Handbook of Carbon, Graphite, Diamond and Fullerenes: Properties, Processing and Applications (Noyes Publications, New Jersey 1993).

[8] H. W. Kroto, J. R. Heath, S. C. O'Brien, R. F. Curl and R. E. Smalley, C_{60}: Buckminsterfullerene, Nature **318**, 162-164 (1985).

[9] "The Nobel Prize in Chemistry 1996". Nobelprize.org. 19 Nov 2012 http://www.nobelprize.org/nobel_prizes/chemistry/laureates/1996/.

[10] S. Iijima, Helical microtubules of grahitic carbon, Nature **354**, 56-58 (1991).

[11] S. Iijima and Toshinari Lchihashi, Single-shell carbon nanotubes of 1-nm diameter, Nature **363**, 603-605 (1993).

[12] D. S. Bethune, C. H. Kiang, M. S. Devries, G. Gorman, R. Savoy, J. Vazquez, R. Beyers, Cobalt-catalyzed growth of carbon nanotubes with single-atomic layerwalls, Nature **363**, 605 (1993).

[13] Jeroen W. G. Wilder, Liesbeth C. Venema, Andrew G. Rinzler, Richard E. Smalley, Cees Dekker, Electronic structure of atomically resolved carbon nanotubes, Nature 391, 59-62 (1998).

[14] K. S. Novoselov, A. K. Geim, S. V. Morozov, D. Jiang, Y. Zhang, S. V. Dubonos, I. V. Grigorieva, A. A. Firsov, Electric Field Effect in Atomically Thin Carbon Films, Science **306**, 666-669 (2004).

[15] C. Berger, Z. Song, T. Li, X. Li, A. Y. Ogbazghi, R. Feng, Z. Dai, A. N. Marchenkov, E. H. Conrad, P. N. First, and W. A. de Heer, J. Phys. Chem. B **108**, 19912-19916 (2004).

[16] K. S. Novoselov, D. Jiang, F. Schedin, T. J. Booth, V. V. Khotkevich, S. V. Morozov, and A. K. Geim, Two-dimensional atomic crystals, PNAS **102** (30), 10451 (2005).

[17] N. D. Mermin, Crystalline order in two dimensions. Phys. Rev. **176**, 250-254 (1968).

[18] L. D. Landau and Lifshitz, E. M. Statistical Physics, Part I (Pergamon, Oxford, 1980).

[19] "The Nobel Prize in Physics 2010". Nobelprize.org. 19 Nov 2012 http://www.nobelprize.org/nobel_prizes/physics/laureates/2010/.

[20] M. O. Goerbig, Electronic properties of graphene in a strong magnetic field, Rev. Mod. Phys. **83**, 1193 (2011).

[21] http://www.sciencemag.org/cgi/content/full/306/5696/666/DC1, Supporting Online Material, Materials and Methods.

[22] Yike Hu, Ming Ruan, Zelei Guo, Rui Dong, James Palmer, John Hankinson, Claire Berger, and Walt A de Heer, Structured epitaxial graphene: growth and properties, J. Phys. D: Appl. Phys. **45**, 154010 (2012).

[23] Konstantin V. Emtsev, Aaron Bostwick, Karsten Horn, Johannes Jobst, Gary L. Kellogg, Lothar Ley, Jessica L. McChesney, Taisuke Ohta, Sergey A. Reshanov, Jonas Rhrl, Eli Rotenberg, Andreas K. Schmid, Daniel Waldmann, Heiko B. Weber, and Thomas Seyller, Towards wafer-size graphene layers by atmospheric pressure graphitization of silicon carbide, Nature Mater. **8**, 203-207 (2009).

[24] Walt A. de Heer, Claire Bergera, Ming Ruana, Mike Sprinklea, Xuebin Lia, Yike Hua, Baiqian Zhanga, John Hankinsona, and Edward Conrada, Large area and structured epitaxial graphene produced by confinement controlled sublimation of silicon carbide, PNAS **108** (41), 16900 (2011).

[25] Alfonso Reina, Xiaoting Jia, John Ho, Daniel Nezich, Hyungbin Son, Vladimir Bulovic, Mildred S. Dresselhaus and Jing Kong, Large Area, Few-Layer Graphene Films on Arbitrary Substrates by Chemical Vapor Deposition, Nano Lett. **9**, 30 (2009).

[26] Keun Soo Kim, Yue Zhao, Houk Jang, Sang Yoon Lee, Jong Min Kim, Kwang S. Kim, Jong-Hyun Ahn, Philip Kim, Jae-Young Choi and Byung Hee Hong, Large-scale pattern growth of graphene films for stretchable transparent electrodes, Nature **457**, 706 (2009).

[27] Sukang Bae, Hyeongkeun Kim, Youngbin Lee, Xiangfan Xu, Jae-Sung Park, Yi Zheng, Jayakumar Balakrishnan, Tian Lei, Hye Ri Kim, Young Il Song, Young-Jin Kim, Kwang S. Kim, Barbaros Özyilmaz, Jong-Hyun Ahn, Byung Hee Hong, and Sumio Iijima, Roll-to-roll production of 30-inch graphene films for transparent electrodes, Nat. Nano **5**, 574-578 (2010).

[28] Xuesong Li, Weiwei Cai, Jinho An, Seyoung Kim, Junghyo Nah, Dongxing Yang, Richard Piner, Aruna Velamakanni1, Inhwa Jung, Emanuel Tutuc, Sanjay K. Banerjee, Luigi Colombo, Rodney S. Ruoff, Large-Area Synthesis of High-Quality and Uniform Graphene Films on Copper Foils, Science **324**, 1312-1314 (2009).

[29] P. R. Wallace, The Band Theory of Graphite, Phys. Rev. **71**, 622-634 (1947).

[30] J. W. McClure, Diamagnetism of graphite, Phys. Rev. **104**, 666-671 (1956).

[31] J. C. Slonczewski and P. R. Weiss, Band structure of graphite. Phys. Rev. **109**, 272-279 (1958).

[32] A. K. Geim and K. S. Novoselov, The rise of graphene, Nature Materials **6**, 183-191 (2007)

[33] K. S. Novoselov, A. K. Geim, S. V. Morozov, D. Jiang1, M. I. Katsnelson, I. V. Grigorieva, S. V. Dubonos and A. A. Firsov, Two-dimensional gas of massless Dirac fermions in graphene, Nature **438**, 197-200 (2005).

[34] Y. Zhang, Yan-Wen Tan, Horst L. Stormer, and Philip Kim, Experimental observation of the quantum Hall effect and Berry's phase in graphene, Nature **438**, 201-204 (2005).

[35] S.V. Morozov, K.S. Novoselov, M.I. Katsnelson, F. Schedin, D.C. Elias, J.A. Jaszczak, and A.K. Geim, Giant Intrinsic Carrier Mobilities in Graphene and Its Bilayer, Phys. Rev. Lett. **100**, 016602 (2008).

[36] T. Dürkop, S. A. Getty, Enrique Cobas, and M. S. Fuhrer, Extraordinary Mobility in Semiconducting Carbon Nanotubes, Nano Lett. **4**, 35-39 (2008).

[37] J. J. Sakurai, Advanced Quantum Mechanics, (Addison-Wesley, USA 1967).

[38] K. v. Klitzing, G. Dorda, M. Pepper, New Method for High-Accuracy Determination of the Fine-Structure Constant Based on Quantized Hall Resistance, Phys. Rev. Lett. **45**, 494-497 (1980).

[39] K. S. Novoselov , Z. Jiang, Y. Zhang, S. V. Morozov, H. L. Stormer, U. Zeitler, J. C. Maan, G. S. Boebinger, P. Kim, and A. K. Geim, Room-Temperature Quantum Hall Effect in Graphene, Science **315**, 1379 (2007).

[40] M. I. Katsnelson, K. S. Novoselov, and A. K. Geim, Chiral tunneling and the Klein paradox in graphene, Nature Physics **2**, 620-625 (2006).

[41] A. Matulis and F.M. Peeters: Analogy between one-dimensional chain models and Graphene, Am. J. Phys. **77**, 595-601 (2009).

[42] F. Schedin, A. K. Geim, S. V. Morozov, E. W. Hill, P. Blake, M. I. Katsnelson and K. S. Novoselov, Detection of individual gas molecules adsorbed on graphene, Nature Materials **6**, 652-655 (2007).

[43] Heejun Yang, Jinseong Heo, Seongjun Park, Hyun Jae Song, David H. Seo, Kyung-Eun Byun, Philip Kim, InKyeong Yoo, Hyun-Jong Chung, and Kinam Kim, Graphene Barristor, a Triode Device with a Gate-Controlled Schottky Barrier, Science **336**, 1140-1143 (2012).

[44] Mark P. Levendorf, Cheol-Joo Kim, Lola Brown, Pinshane Y. Huang, Robin W. Havener, David A. Muller, and Jiwoong Park Graphene and boron nitride lateral heterostructures for atomically thin circuitry, Nature **488**, 627-632 (2012).

[45] A. H. Castro Neto, F. Guinea, N. M. R. Peres, K. S. Novoselov, and A. K. Geim, The electronic properties of graphene, Rev. Mod. Phys. **81**, 109 (2009).

[46] S. Kim, I. Jo, D. C. Dillen, D. A. Ferrer, B. Fallahazad, Z. Yao, S. K. Banerjee, and E. Tutuc, Direct Measurement of the Fermi Energy in Graphene Using a Double-Layer Heterostructure, Phys. Rev. Lett. **108**, 116404 (2012).

[47] M. Sprinkle, D. Siegel, Y. Hu, J. Hicks, A. Tejeda, A. Taleb-Ibrahimi, P. Le Fe'vre, F. Bertran, S. Vizzini, H. Enriquez, S. Chiang, P. Soukiassian, C. Berger, W. A. de Heer, A. Lanzara, and E. H. Conrad, First Direct Observation of a Nearly Ideal Graphene Band Structure, Phys. Rev. Lett. **103**, 226803 (2009).

[48] C. Cohen-Tannoudji, B. Diu, and F. Laloë, Quantum Mechanics, Vol. 2 (Hermann and John Wiley & Sons, Paris 1997).

[49] M. L. Sadowski, G. Martinez, and M. Potemski, Landau Level Spectroscopy of Ultrathin Graphite Layers, Phys. Rev. Lett. **97**, 266405 (2006).

[50] Z. Jiang, E. A. Henriksen, L. C. Tung, Y. -J. Wang, M. E. Schwartz, M. Y. Han, P. Kim, and H. L. Stormer, Infrared Spectroscopy of Landau Levels of Graphene, Phys. Rev. Lett. **98**, 197403 (2007).

[51] V. P. Gusynin, S. G. Sharapov, and J. P. Carbotte, Anomalous Absorption Line in the Magneto-Optical Response of Graphene, Phys. Rev. Lett. **98**, 157402 (2007).

[52] R. S. Deacon, K.-C. Chuang, R. J. Nicholas, K. S. Novoselov, and A. K. Geim, Cyclotron resonance study of the electron and hole velocity in graphene monolayers, Phys. Rev. B **76**, 081406(R) (2007).

[53] E. McCann, Asymmetry gap in the electronic band structure of bilayer graphene , Phys. Rev. B **74**, 161403(R) (2006).

[54] T. Ohta, A. Bostwick, T. Seyller, K. Horn and E. Rotenberg, Controlling the Electronic Structure of Bilayer Graphene, Science **313**, 951 (2006).

[55] H. Min, B. Sahu, S. K. Banerjee and A. H. MacDonald, Ab initio theory of gate induced gaps in graphene bilayers, Phys. Rev. B **75**, 155115 (2007).

[56] Eduardo V. Castro, K. S. Novoselov, S.V. Morozov, N. M. R. Peres, J. M. B. Lopes dos Santos, Johan Nilsson, F. Guinea, A. K. Geim, and A. H. Castro Neto, Biased Bilayer Graphene: Semiconductor with a Gap Tunable by the Electric Field Effect, Phys. Rev. Lett. **99**, 216802 (2007).

[57] M. Fujita, K. Wakabayashi, K. Nakada, and K. Kusakabe, Peculiar Localized State at Zigzag Graphite Edge, J. Phys. Soc. Jpn. **65**, 1920 (1996).

[58] Z. F. Wang, Q. Li, H. Zheng, H. Ren, H. Su, Q. W. Shi, and J. Chen, Tuning the electronic structure of graphene nanoribbons through chemical edge modification: A theoretical study, Phys. Rev. B **75**, 113406 (2007).

[59] M. Ezawa, Peculiar band gap structure of graphene nanoribbons, Phys. Stat. Sol. (c) **4**, 489 (2007).

[60] M. Ezawa, Peculiar width dependence of the electronic properties of carbon nanoribbons, Phys. Rev. B **73**, 045432 (2006).

[61] C. P. Chang, B. R. Wu, R. B. Chen, and M. F. Lin, Deformation effect on electronic and optical properties of nanographite ribbons, J. Appl. Phys. **101**, 063506 (2007).

[62] L. Brey and H. A. Fertig, Electronic states of graphene nanoribbons studied with the Dirac equation, Phys. Rev. B **73**, 235411 (2006).

[63] L. Brey and H. A. Fertig, Elementary electronic excitations in graphene nanoribbons, Phys. Rev. B **75**, 125434 (2007).

[64] Y. -W. Son, M. L. Cohen, and S. G. Louie, Energy Gaps in Graphene Nanoribbons, Phys. Rev. Lett. **97**, 216803 (2006).

[65] M. Y. Han, B. Ozyilmaz, Y. Zhang, P. Kim, Energy Band-Gap Engineering of Graphene Nanoribbons, Phys. Rev. Lett. **98**, 206805 (2007).

[66] M. Fujita, K. Wakabayashi, K. Nakada, and K. Kusakabe, Peculiar Localized State at Zigzag Graphite Edge, J. Phys. Soc. Jpn. **65**, 1920 (1996).

[67] T. B. Martins, R. H. Miwa, A. J. R. da Silva, and A. Fazzio, Electronic and Transport Properties of Boron-Doped Graphene Nanoribbons, Phys. Rev. Lett. **98**, 196803 (2007).

[68] R. N. Costa Filho, G. A. Farias, and F. M. Peeters, Graphene ribbons with a line of impurities: Opening of a gap, Phys. Rev. B **76**, 193409 (2007).

[69] Vitor M. Pereira, A. H. Castro Neto, and N. M. R. Peres, Tight-binding approach to uniaxial strain in graphene, Phys. Rev. B **80**, 045401 (2009).

[70] B. Partoens and F. M. Peeters, From graphene to graphite: Electronic structure around the K point, Phys. Rev. B **74**, 075404 (2006).

[71] F. Guinea, A. H. Castro Neto and N. M. Peres, Electronic states and Landau levels in graphene stacks, Phys. Rev. B **73**, 245426 (2006)

[72] B. Partoens and F. M. Peeters, Normal and Dirac fermions in graphene multilayers: Tight-binding description of electronic structure, Phys. Rev. B **75**, 193402 (2007).

[73] M. Aoki and H. Amawashi, Dependence of band structures on stacking and field in layered graphene, Solid State Commun. **142**, 123 (2007).

[74] M.S. Dresselhaus and G. Dresselhaus, Intercalation compouds of graphite, Adv. Phys. **51**, 1 (2002).

[75] A. B. Kuzmenko, I. Crassee, and D. van der Marel, Determination of the gate-tunable band gap and tight-binding parameters in bilayer graphene using infrared spectroscopy, Phys. Rev. B **80**, 165406 (2009).

[76] E. McCann and M. Koshino, The electronic properties of bilayer graphene, arXiv:1205.6953 [cond-mat.mes-hall] (2012).

[77] E. McCann and V. I. Fal'ko, Landau-Level Degeneracy and Quantum Hall Effect in Graphite Bilayer, Phys. Rev. Lett. **96**, 086805 (2006).

[78] J. Milton Pereira Jr., F. M. Peeters, and P. Vasilopoulos, Landau levels and oscillator strength in a biased bilayer of graphene, Phys. Rev. B **76**, 115419 (2007).

[79] E. A. Henriksen, Z. Jiang, L.-C. Tung, M. E. Schwartz, M. Takita, Y.-J. Wang, P. Kim, and H. L. Stormer, Cyclotron Resonance in Bilayer Graphene, Phys. Rev. Lett. **100**, 087403 (2008).

[80] K. S. Novoselov, E. McCann, S. V. Morozov, V. I. Fal'ko, M. I. Katsnelson, U. Zeitler, D. Jiang, F. Schedin1, and A. K. Geim, Unconventional quantum Hall effect and Berry's phase of 2π in bilayer graphene, Nature Phys. **2**, 177 (2006).

[81] M. Koshino and E. McCann, Gate-induced interlayer asymmetry in ABA-stacked trilayer graphene, Phys. Rev. B **79**, 125443 (2009).

[82] M. Koshino and E. McCann, Trigonal warping and Berry's phase Nπ in ABC-stacked multilayer graphene, Phys. Rev. B **80**, 165409 (2009).

[83] F. Zhang, B. Sahu, H. Min and A. H. MacDonald, Band structure of ABC-stacked graphene trilayers, Phys. Rev. B **82**, 035409 (2010).

[84] S. Yuan, Rafael Roldn1, and M. I. Katsnelson, Landau level spectrum of ABA- and ABC-stacked trilayer graphene, Phys. Rev. B **84**, 125455 (2011).

[85] C. H. Lui, Z. Li, Z. Chen, P. V. Klimov, L. E. Brus, and T. F. Heinz, Imaging Stacking Order in Few-Layer Graphene, Nano Lett. **11**, 164 (2011).

[86] C. H. Lui, Z. Li, K. F. Mak, E. Cappelluti, and T. F. Heinz, Observation of an electrically tunable band gap in trilayer graphene, Nature Physics **7**, 944-947 (2011).

[87] A. A. Avetisyan, B. Partoens, and F. M. Peeters, Stacking order dependent electric field tuning of the band gap in graphene multilayers, Phys. Rev. B **81**, 115432 (2010).

[88] M. Aoki and H. Amawashi, Dependence of band structures on stacking and field in layered graphene, Solid State Commun. **142**, 123 (2007).

[89] T. Taychatanapat, K. Watanabe, T. Taniguchi, and Pablo Jarillo-Herrero, Quantum Hall effect and Landau-level crossing of Dirac fermions in trilayer graphene, Nature Physics **7**, 621-625 (2011).

[90] L. Zhang, Y. Zhang, J. Camacho, M. Khodas, and I. Zaliznyak The experimental observation of quantum Hall effect of l=3 chiral quasiparticles in trilayer graphene, Nature Physics **7**, 953957 (2011).

[91] A. Kumar, W. Escoffier, J. M. Poumirol, C. Faugeras, D. P. Arovas, M. M. Fogler, F. Guinea, S. Roche, M. Goiran, and B. Raquet, Integer Quantum Hall Effect in Trilayer Graphene, Phys. Rev. Lett. **107**, 126806 (2011).

[92] M. Koshino and E. McCann, Landau level spectra and the quantum Hall effect of multilayer graphene, Phys. Rev. B **83**, 165443 (2011).

[93] M. Koshino and E. McCann, Parity and valley degeneracy in multilayer graphene, Phys. Rev. B **81**, 115315 (2010).

[94] W. Bao, Z. Zhao, H. Zhang, G. Liu, P. Kratz, L. Jing, J. Velasco, Jr., D. Smirnov, and C. N. Lau Magnetoconductance Oscillations and Evidence for Fractional Quantum Hall States in Suspended Bilayer and Trilayer Graphene, Phys. Rev. Lett. **105**, 246601 (2010).

[95] W. Bao, L. Jing, J. Velasco Jr, Y. Lee, G. Liu, D. Tran, B. Standley, M. Aykol, S. B. Cronin, D. Smirnov, M. Koshino, E. McCann, M. Bockrath, and C. N. Lau Stacking-dependent band gap and quantum transport in trilayer graphene, Nature Physics **7**, 948952 (2011).

[96] Y. Liu, S. Goolaup, C. Murapaka, W. S. Lew, and S. K. Wong, Effect of Magnetic Field on the Electronic Transport in Trilayer Graphene, ACS Nano. **4**, 7087 (2010).

[97] S. H. Jhang, M. F. Craciun, S. Schmidmeier, S. Tokumitsu, S. Russo, M. Yamamoto, Y. Skourski, J. Wosnitza, S. Tarucha, J. Eroms, C. Strunk Stacking-order dependent transport properties of trilayer graphene, Phys. Rev. B **84**, 161408(R) (2011).

[98] A. A. Avetisyan, B. Partoens1, and F. M. Peeters, Electric-field control of the band gap and Fermi energy in graphene multilayers by top and back gates, Phys. Rev. B **80**, 195401 (2009).

[99] S. H. R. Sena, J. M. Pereira, Jr., G. A. Farias, and F. M. Peeters, Cyclotron resonance of trilayer graphene, Phys. Rev. B **86**, , 085412 (2012).

[100] B. Partoens and F. M. Peeters, Normal and Dirac fermions in graphene multilayers: Tight-binding description of the electronic structure, Phys. Rev. B **75**, 193402 (2007).

[101] H. Min and A. H. MacDonald, Chiral decomposition in the electronic structure of graphene multilayers, Phys. Rev. B **77**, 155416 (2008).

[102] M. Koshino and E. McCann, Trigonal warping and Berrys phase Nπ in ABC-stacked multilayer graphene, Phys. Rev. B **80**, 165409 (2009).

[103] I. Martin, Ya. M. Blanter, and A. F. Morpurgo Topological Confinement in Bilayer Graphene, Phys. Rev. Lett. **100**, 036804 (2008).